

**3D AND 2.5D MICROFABRICATION TECHNOLOGIES FOR
HIGH-DENSITY ELECTRONIC HETEROGENEOUS
INTEGRATION AND BIOSENSING APPLICATIONS**

A Dissertation
Presented to
The Academic Faculty

by

Muneeb Zia

In Partial Fulfillment
of the Requirements for the Degree
Doctor of Philosophy in the
School of Electrical and Computer Engineering

Georgia Institute of Technology
December 2018

COPYRIGHT © 2018 BY MUNEEB ZIA

**3D AND 2.5D MICROFABRICATION TECHNOLOGIES FOR
HIGH-DENSITY ELECTRONIC HETEROGENEOUS
INTEGRATION AND BIOSENSING APPLICATIONS**

Approved by:

Dr. Muhanad Bakir, Advisor
School of Electrical and Computer
Engineering
Georgia Institute of Technology

Dr. Omer Inan
School of Electrical and Computer
Engineering
Georgia Institute of Technology

Dr. Oliver Brand
School of Electrical and Computer
Engineering
Georgia Institute of Technology

Dr. Samuel Sober
Department of Biology
Emory University

Dr. Hua Wang
School of Electrical and Computer
Engineering
Georgia Institute of Technology

Date Approved: [October 29, 2018]

DEDICATION

To

*My parents for their endless love and support, for being there day and night and sacrifice
their comforts for me, and being role models that I could always look up to*

*My wife and daughter for supporting me, comforting me and bearing with me through
this journey, and for always giving me a reason to smile*

*My brother for being a source of inspiration, for supporting me at every step and being
the friend to rely on through this journey*

ACKNOWLEDGEMENTS

I would really like to thank Dr. Bakir for his invaluable mentorship throughout my PhD journey. His guidance and support has been instrumental in allowing me to develop not only my research skills but also my soft skills. Perhaps more than anything else, I really appreciate the fact that he believed in me even when I would have doubts; each meeting with him ended with his positive reinforcement of how he believed that I can accomplish a task, no matter how difficult I thought it was! Furthermore, the friendly and conducive for research culture that he has created in the group has helped me immensely in trying to achieve my fullest potential.

I would also like to thank Dr. Oliver Brand, Dr. Hua Wang, Dr. Omer Inan and Dr. Samuel Sober for serving on my thesis committee; I would specially like to thank Dr. Wang and his students, Dr. Jong-Soek Park and Dr. Tayiun Chi for collaboration on the electronic microplate project. Their input during the design phase as well as measurements for the assembled system were critical for the success of that research effort. I would also like to thank Dr. Sober and Dr. Bryce Chung for the collaboration on the flexible microelectrode project. I have thoroughly enjoyed their infectious passion for research and feel extremely lucky to have such dedicated and hardworking collaborators. I would specially like to acknowledge Dr. Chung for doing all the *in vivo* experiments he performed to collect the EMG data. Dr. Chung's contributions were pivotal in the design and characterization of the fabricated multi-electrode arrays.

I would also like to thank all of my I3DS group members. I was fortunate to have some exceptional mentors when I joined the group including Dr. James Yang, Dr. Chaoqi

Zhang and Dr. Paragkumar Thadesar who taught me a lot, especially making me familiar and comfortable with the cleanroom usage and made me feel welcome into the group. I also wish to especially thank Dr. Hanju Oh for simulations and measurements for the micro-inductors and also help with taking multiple SEM images for the different projects I have completed in my PhD. I have had research discussions with all of the current group members over the course of my PhD and I really appreciate everyone's input and help. I would like to thank Paul Jo, Joe Gonzalez and Sreejith K. Rajan for the invaluable discussions and help in the heterogeneous integration, electronic microplate and the flexible MEA projects. I would also like to thank Reza Abbaspour and Mingu Kim for their help to better understand the flexible polymer chemistry.

As all of my experimental work was completed in the IEN cleanroom facilities at Georgia Tech, I want to thank all the leadership and staff who helped provide support for our processes and were always there for any help that I required. In particular, I would like to thank Gary Spinner, Charlie Turgeon, Charlie Suh, Hang Chen and Chris Yang for their help and support.

Lastly, and the most importantly, I would like to thank my family. I will never be able to thank my parents, Zia and Rizwana, enough for their endless and selfless love and support throughout my life. Their hard work and sacrifices were vital in all of my accomplishments. I would also like to thank my wife Rabia and daughter Maryam for being a source of comfort and providing boundless love and support and bearing with me through my PhD journey. I would also like to thank my brother, Aneeq for always being there and being a source of inspiration, my sister in law, Ayesha and nephew Omer, who's addition into our family have certainly made some of the best memories in my PhD journey.

TABLE OF CONTENTS

ACKNOWLEDGEMENTS	iv
LIST OF TABLES	viii
LIST OF FIGURES	ix
SUMMARY	xiii
CHAPTER 1. Introduction	1
1.1 The need for high-density interconnects	1
1.2 Current methods and relevant research	6
1.2.1 Trends in heterogeneous integration	7
1.2.2 Trends in biosensing systems for in vitro and in vivo measurements	10
1.3 Organization of this thesis	12
CHAPTER 2. Multi-interposer system utilizing flexible interconnects	15
2.1 System Overview	17
2.2 Fabrication and Assembly	18
2.2.1 Key Technology Enablers	18
2.2.2 System assembly	20
2.2.3 Electrical Characterization	22
2.3 System-level Analysis	26
2.4 Conclusion	30
CHAPTER 3. Co-fabrication of 3D solenoidal micro-inductors with flexible i/os	32
3.1 Fabrication	34
3.2 Electrical and Mechanical Measurements	39
3.3 Conclusion	45
CHAPTER 4. 3D Integrated Electronic Microplate Platform for Low-cost Repeatable Biosensing Applications	47
4.1 System Overview	49
4.2 Fabrication of E-microplate	50
4.3 Characterization	54
4.3.1 Mechanical Characterization of MFIs	54
4.3.2 Electrical Characterization of TSV-MFI Link	55
4.3.3 Cell Growth	56
4.3.4 Integrated System characterization	60
4.4 Conclusion	66
CHAPTER 5. Fabrication and Characterization of High Density Electrodes on Flexible Substrate for In Vivo EMG Recording	68
5.1 Introduction	68
5.2 Flexible MEA Fabrication	72
5.3 MEAs Characterization and EMG Measurements	76

5.3.1	Electrical Characterization of Fabricated MEAs	76
5.3.2	EMG Measurements	77
5.4	Conclusion	80
CHAPTER 6. Fabrication and Characterization of 3D Multi-Electrode Array on Flexible Substrate for In Vivo EMG Recording from Expiratory Muscle of Songbird		82
6.1	Introduction	82
6.2	Fabrication of 3D Multi-Electrode Arrays	83
6.3	EMG Measurement and SNR Comparison	86
6.4	Conclusion	91
CHAPTER 7. Summary And Future Work		92
7.1	Future Work	93
7.1.1	Heterogeneous integration	93
7.1.2	In vitro and in vivo biosensing	94
REFERENCES		97

LIST OF TABLES

Table 1 Summary of relevant published work on 3D inductors	10
Table 2 Insertion Loss Comparison for Compliant Interconnects and Bump	23
Table 3 Extracted RLGC Parameter for the Interposer-FR4 MFIs.....	25
Table 4 Performance Comparison of the Fabricated Inductors with Published Work	43
Table 5 Dimensions of the fabricated MFIs and TSVs.....	52
Table 6 Mouse embryonic stem cell growth on oxide and nitride surfaces with sensing electrodes	59
Table 7 Summary of the different types of flexible electrodes in literature	71
Table 8 Temperature profile used for curing polyimide.....	73
Table 9 Range of trace resistance and electrode impedance for each electrode contact site	77
Table 10 SNR comparison of EMG signal recorded using the 2D and 3D MEAs. N/A is listed where signal was not discernable from noise.....	90

LIST OF FIGURES

Figure 1 Scaling of processors I/O [1].....	1
Figure 2 Conventional interconnect methodologies (a) electrical interconnects on motherboard, (b) flex electrical connectors, and (c) optical interconnects on motherboard	3
Figure 3 CMOS biosensor – cell growth directly onto the sensing electrodes	5
Figure 4 Silicon based (a) electrical interposer, (b) EMIB and (c) optical interposer – fine pitch wires and waveguides achievable on silicon enables high-density communication..	6
Figure 5 Schematic of the HIST platform [101].....	8
Figure 6 Summary of core technologies enabling the presented research in this thesis...	13
Figure 7 Two interposer tiles mounted on FR-4 interconnected using silicon bridge.....	16
Figure 8 Double-sided MFI fabrication process	18
Figure 9 (a) PSAS on bridge (b) inverse pyramid pit	19
Figure 10 Demonstrated technology enablers for the proposed multi-interposer heterogeneous system	20
Figure 11 Assembly of multiple interposers with glass.....	21
Figure 12 Simulation setup for the MFIs.....	22
Figure 13 Experimental setup with RF probing of interposer-FR4 MFIs	23
Figure 14 (a) Measured and simulated S11 and S21 parameters for MFI, (b) comparison of S21 parameter before and after deformation cycles	24
Figure 15 (a) Assembled system with 2 interposer tiles bridged using silicon bridge (b) top view of multi-interposer system array – center to center distance between adjacent interposers is taken to be 2 cm.....	26
Figure 16 Optimal width for different lengths of wires on interposers that maximizes BWD/EPB.....	27
Figure 17 Modelling flowchart for BWD and EPB calculation	28
Figure 18 (a) Number of optical couplers and silicon bridges with array size, (b) EPB comparison of four different lengths’ electrical interconnects with optical interconnect and (c) crossover length – interconnect length after which electrical interconnect link dissipates more energy after this length.....	28
Figure 19 Envisioned schematic utilizing fabricated micro-inductors and MFIs; figure extends HIST [101, 102].....	34
Figure 20 Fabrication process for micro-inductors and MFIs	35
Figure 21 Profilometer scan of the reflowed domes after double-exposure process – height difference of 70 μm between the small and the large domes was achieved	36
Figure 22 Optical image showing electroplating mold for large NiW MFIs with resist covered copper micro-inductors and MFIs	36
Figure 23 SEM images of fabricated sample showing (a) NiW MFIs, (b) Fine-pitch Cu MFIs, (c) Cu micro-inductors and (d) X-ray images showing bottom and top metallization with good connection	37
Figure 24 SEM images of the samples depicting height differential – the height differential between the co-fabricated MFIs and the micro-inductors allow the inductors	

to be embedded between tiers in a stack while the MFIs provide the required interconnection and compensate any surface non-planarity	38
Figure 25 Measurement setup: A Cascade microprobe station and Keysight network analyzer and optical image of micro-inductors with GSG probes. (b) Simulation configuration for inductors using ANSYS HFSS software; tind, wind, and gind refer to the thickness, width, and gap of solenoid inductors, respectively, and rdome refers to the radius of a sacrificial photoresist dome.	39
Figure 26 Measured and simulated S-parameters for the 5-turn inductor; results show close match between the simulated and measured values	41
Figure 27 Measured (a) inductance, (b) resistance and (c) Q-factor of the 5 and 8 turn micro-inductors	42
Figure 28 Trade-off between dome radius and the micro-inductor’s peak Q-factor and inductance	44
Figure 29 Compliance measurements for the fabricated MFIs.....	45
Figure 30 Envisioned micro-fabricated electronic microplate platform – the electronic microplate can be replaced, and the biosensor reused	49
Figure 31 Fabrication flow of the e-microplate	50
Figure 32 Sensing pixel group of e-microplate and its surface profile.....	52
Figure 33 X-ray and SEM images of the fabricated e-microplate pixel group.....	53
Figure 34 Mechanical compliance measurements for fabricated MFIs.....	55
Figure 35 Four-point resistance measurement results for the TSV-MFI link.....	56
Figure 36 Cell growth results after 48 hours of seeding on (a) nitride, (b) oxide, (c) nitride with sensing electrodes only, (d) oxide with sensing electrodes only, (e) silicon membrane with oxide surface, sensing electrodes, and TSVs and (f) control with cells on TCPS.....	58
Figure 37 Test setup for gain and noise measurements – sensing electrodes were wire-bonded to test board for measurements	60
Figure 38 Test setup for impedance mapping.....	61
Figure 39 X-ray image showing accurate alignment between e-microplate and CMOS biosensor	62
Figure 40 Schematic of internal voltage sensing amplifier and its connection to the e-microplate’s pixel.....	63
Figure 41 (a) Amplifier gain measurements – the amplifier gain remains unchanged with the incorporation of the e-microplate, (b) Input referred noise measurements – low input referred noise ensures high SNR when measuring weak signals.....	65
Figure 42 Impedance measurement for air and DPBS measured via e-microplate’s pixel group – measurements verify functional accuracy of the platform	66
Figure 43 Schematic of experimental set up and EMG activity recorded during breathing. A) The exhaling phase of breathing in songbirds is controlled by expiratory muscles that contract around an air sac. Motor neurons excite individual muscle fibers that cause the expiratory muscle to contract. Multi-electrode arrays are used to record electromyography (EMG) activity. B) Increases in air pressure occur when the expiratory muscles contract. Spike sorting algorithms are used to detect individual spikes (Unit 1, Unit 2) from recorded muscle activity (EMG 1, EMG 2). Tick marks above physiological traces indicate spike times. Time scale: 100 ms. Vertical scale: 30 μ V.	69
Figure 44 Fabrication process flow for Flexible MEAs.	72

Figure 45 Optical image showing the fabricated electrodes for Songbird’s expiratory muscle; (a) 200 μm diameter, 300 μm pitch, (b) 125 μm diameter, 200 μm pitch and (c) 50 μm diameter, 100 μm pitch.....	74
Figure 46 Fabricated mouse fore-limb array; 16 electrodes are spatially arranged in a cluster of 4 electrodes for picking up EMG from different locations in the fore-limb.....	75
Figure 47 Characterization of electrical properties for different electrode sizes. (a) Schematic of four-point DC resistance measurement across traces for each electrode array. (b) Image of impedance measurement at 1,000 Hz where each electrode array is submerged in a grounded bath of saline.	76
Figure 48 Data collection flow chart. Rhythmic muscle activity generates air pressure during breathing (dark gray). Analog signals (solid arrows) are detected by the Flexible MEA and an Air Pressure Sensor (black outlined boxes). EMG activity from the Flexible MEA is amplified and digitized by the Intan RHD2132 Amplifier Chip and air pressure data are digitized by the Intan RHD2000 Eval Board (light gray outlined boxes). The Eval Board records digital signals (dashed arrows) for both EMG and air pressure data for analysis (gray boxes). Spike sorting is used to distinguish individual motor units and mutual information is used to analyze neural activity and behavior.	78
Figure 49 EMG recordings of expiratory muscle activity using two types of MEA devices. (a-c) EMG activity during 2 breathing cycles shows comparable signal qualities for all electrode sizes. Blue tick marks indicate spike times identified using a previously-described spike-sorting algorithm [11]. Time scale: 30 ms. Vertical scale: (a,b) 50 μV , (c) 20 μV . (d) EMG activity recorded using a pair of fine-wire electrodes, which, in this recording, the waveforms of individual spikes were not sufficiently distinct to be isolated by spike sorting. Time scale: 30 ms. Vertical scale: 1000 units.	79
Figure 50 EMG recording from mouse shoulder muscle using the fabricated MEAs	80
Figure 51 Fabrication process flow for the flexible 3D MEAs	83
Figure 52 Profilometer scan data after reflow of photoresist to form the hemispherical domes (step (e) in the process flow). A 50 μm dome height was obtained for the 3D MEAs and can be modulated by changing the photoresist film thickness.	84
Figure 53 Optical images of fabricated 3D MEAs	85
Figure 54 3D optical images of the fabricated 3D MEAs	86
Figure 55 Example air pressure and electromyograph recordings. (a,b) EMG recording after 5 minutes of array placement on the expiratory muscle of the songbird with (a) flexible 2D MEA, and (b) flexible 3D MEA. (c,d) EMG recording after 25 minutes of array placement on the expiratory muscle of songbird with (c) flexible 2D MEA, and (d) flexible 3D MEA.....	89
Figure 56 Comparison of signal-to-noise ratio (SNR) using multi-electrode arrays with either 2D (red) or 3D (blue) electrode sites. Recordings for each trial were collected over at least 30-minute periods and alternated between 2D and 3D MEAs to control for non-stationary factors of the in vivo preparation. An average (solid or dashed line) SNR was calculated every 3 minutes with 4 measurements during each minute to determine a standard error of the mean (shaded regions).....	90
Figure 57 Example showing conduction along two neurons – a major motivation for HD E-microplate is being able to trace the exact path of the electrical activity	94
Figure 58 RDL layout for realizing HD E-microplate without scaling the TSVs or flexible interconnects	94

Figure 59 Future vision of multi-electrode array with multi-layer high-density RDL and integrated signal conditioning IC..... 95

SUMMARY

The demand for continuous increase in computing performance has put an overburdening demand on I/O interface and novel heterogeneous integration to allow performance benefits at system level. The demand for high-density integration is not limited to computing systems but, with ever increase use of electronics in biological science space, extends to *in vitro* and *in vivo* biosensing systems as well. In this research, 3D and 2.5D microfabrication technologies for advancing heterogeneous integration and biosensing systems are presented.

Technology enablers for realizing large-scale silicon systems as well as unique fabrication allowing 3D solenoidal micro-inductors alongside flexible interconnects are discussed in the first half of the thesis. The fabrication technology utilizes photoresist reflow process to obtain dome-shaped structures to serve as the basis for the flexible interconnects, self-alignment structures and 3D solenoidal micro-inductors. The fabrication technology discussed in Chapter 3 also gives control over the height, thickness, material and pitch of the fabricated flexible interconnects. This allows for close integration of disparate ICs along with micro-inductors.

The same fabrication process is then adapted and applied to *in vitro* and *in vivo* biosensing domain; through-silicon-vias and flexible interconnects are used to fabricate an electronic microplate platform for low-cost high-throughput biosensing. Furthermore, the reflow process is further utilized to fabricate 3D multi-electrode arrays on flexible substrate for high SNR EMG recordings from songbird.

CHAPTER 1. INTRODUCTION

1.1 The need for high-density interconnects

Improving performance of computing systems is becoming increasingly difficult and complex as transistor scaling becomes technically and economically challenging as well as interconnects become a critical bottleneck limiting the enhancement of system performance; the ability to sustain high-bandwidth low-loss communication between chips is limiting system performance despite the increased computing power of individual chips. Figure 1 shows the total off-chip bandwidth trends, along with the number of package pins [1].

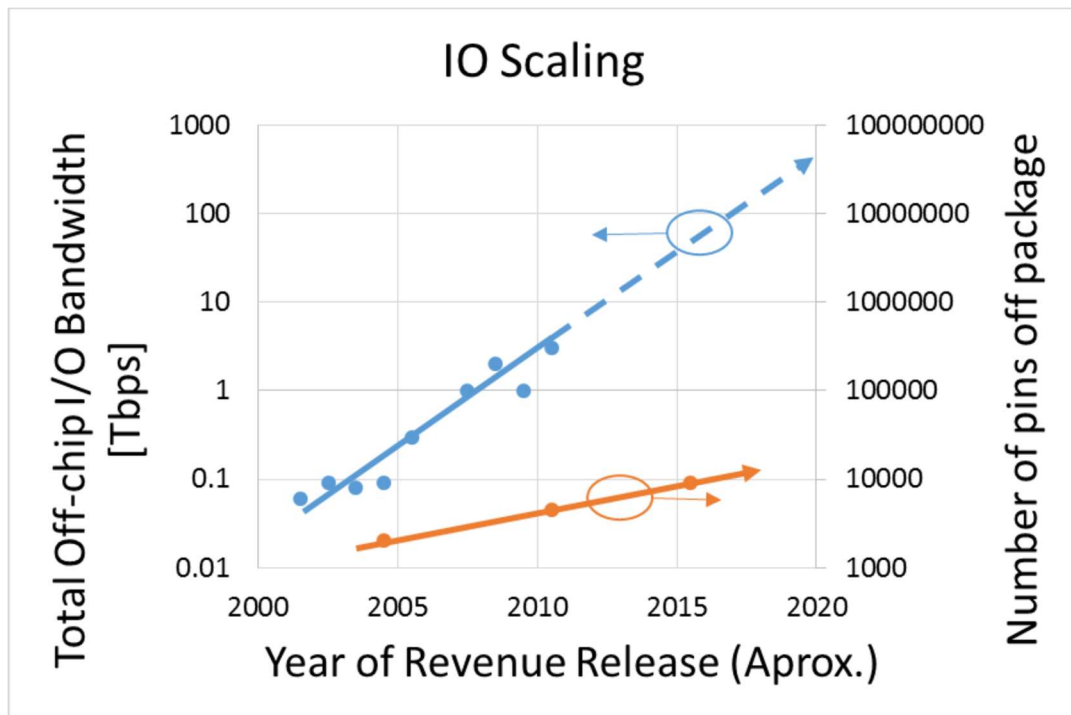
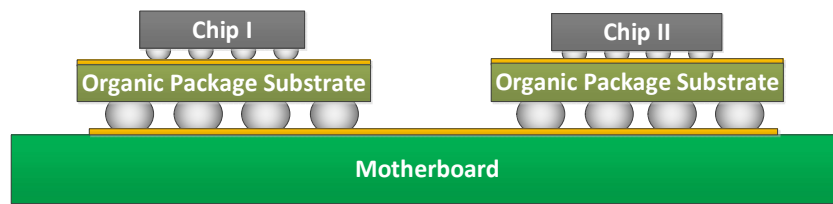
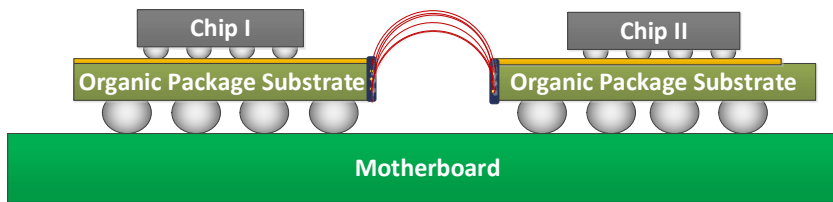


Figure 1 Scaling of processors I/O [1]

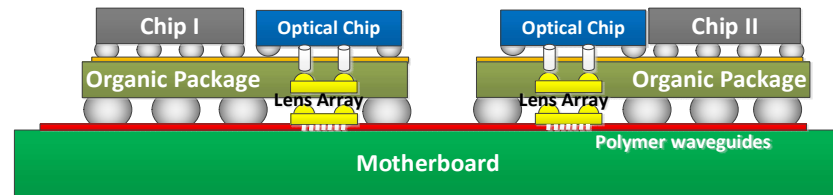
As seen from the figure, the total off-chip I/O bandwidth is consistently increasing with an ever-increasing mismatch between the required off-chip bandwidth and the increase in the number of off-chip I/O pins. Although increase in channel data rate can allow for an increase in total aggregate bandwidth, the increased need for equalization and noise cancellation circuitry requires additional power and area deeming it a less attractive option [2]. Thus, current interconnection methodologies are quickly becoming incapable of sustaining the high-bandwidth demand. For example, motherboard-based interconnects (Figure 2 (a)) have been widely used for relatively long range ($\sim 30 - 100$ cm) [3] interconnects between modules. However, with the required I/O bandwidth between chips and modules increasing drastically, motherboard based electrical interconnects have not been able to keep up with the bandwidth demand. This is primarily because of the inherent limit of the minimum channel pitch achievable on the motherboard; high density differential stripline pair has typically pitch in the order of ~ 600 μm [3]. Assuming 10 Gb/s channel data rate would imply that the bandwidth density achievable utilizing motherboard based electrical interconnects is in the order of ~ 16 Gb/s/mm. Operating channels at a higher frequency can result in a higher aggregate bandwidth between modules, however, higher channel frequencies are limited by channel dispersion limits, the need for higher number of equalization taps and a consequent increase in the power dissipation [2]. Figure 2 (b) shows flex connectors as an alternate to connecting package modules via motherboard. High-speed connectors are used to directly connect the package substrate thereby bypassing the conventional socket and motherboard. This can allow 3x increase in raw bandwidth and the ability to transmit higher data rates over longer distances as compared to FR4 boards [4].



(a)



(b)



(c)

Figure 2 Conventional interconnect methodologies (a) electrical interconnects on motherboard, (b) flex electrical connectors, and (c) optical interconnects on motherboard

Optical interconnects have also been explored for low-loss long-range chip-to-chip interconnects. The ability to send multiple wavelengths in the same channel using wavelength division multiplexing (WDM) allows higher bandwidth communication between modules. However, incorporating the electrical to optical conversion overhead and the laser efficiency increases the total energy per bit expended and hence limits their

utilization for short distances for which electrical interconnects expense less overall energy. Furthermore, the pitch of the waveguides on the board is typically fabrication limited and hence cannot be scaled to very fine dimensions. Figure 2 (c) shows the schematic of terabus architecture with polymer waveguides at the board-level fabricated at a 62.5 μm pitch [5, 6]. A silicon based ‘optical chip’ converts the electrical signals to optical signals which is then relayed to the motherboard via a lens array and optical couplers. The terabus has been shown to provide a bidirectional aggregate data rate of 360 Gb/s bandwidth over 24 transmitter and 24 receiver channels with polymer waveguide on the optical PCB with each channel operating at 15 Gb/s and a link EPB of 9.7 pJ/bit [6]. This translates to a bandwidth density of ~ 240 Gb/s/mm.

Consequently, there are significant ongoing research efforts aiming to overcome this hurdle. Heterogeneous integration has emerged as a key enabler of increased computing performance by allowing high-bandwidth low-loss interconnects between individual modules of disparate substrates; this allows for optimization of ICs in different process nodes connected using efficient high-density interconnects. Recent advances in 2.5D [7, 8] packaging as well as silicon interposer-level optical interconnects [9] have allowed high-bandwidth communication between chips (or stack of chips) on interposers. Simultaneously, there is also a push towards integrating passives e.g. inductors, capacitors etc. on, or in close proximity to, the chips [10] as they are an integral part of various radio frequency (RF) circuits including filters, amplifiers, oscillators and transceivers with applications in communication, sensing and power delivery domains [11-14]. Thus, there is a need for a large-scale silicon system that can enable simultaneous electrical and optical

interconnections, allow close integration with passives and give flexibility to replace individual components in a modular fashion.

The need for high density interconnects, however, is not limited to high-performance computing. The increasing use of electronics in the biological science domain has generated an ever-growing need for high density interconnects between a ‘living’ sample and electronics. *In vitro* biosensors, for example, are increasingly being used for sensing electrical, magnetic, and optical properties of cellular and molecular samples. Using living cells for drug or pathogen detection links the analyte effects with corresponding changes in cellular properties that can be subsequently detected using integrated CMOS biosensors [15-23]. However, this technique necessitates the growth of cells onto the CMOS biosensors’ surface (Figure 3). As the CMOS biosensor needs to undergo rigorous cleaning to avoid contamination, this makes the biosensor reuse difficult and adds additional processing time and cost. Thus, there is a need for a solution that allows for the reuse of the biosensor while enabling high-density interconnects between the cells and the biosensor.

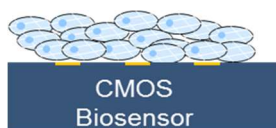
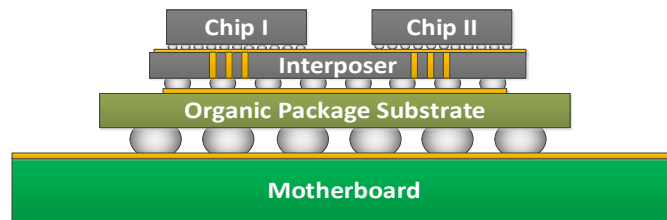


Figure 3 CMOS biosensor – cell growth directly onto the sensing electrodes

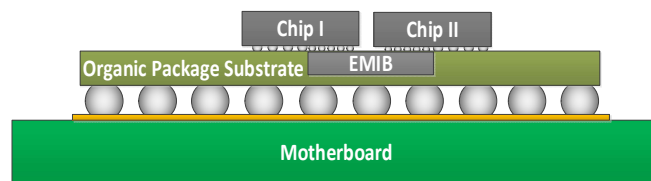
Similarly, *in vivo* studies for better understanding how brain controls, for example, motor control [24] by stimulation and recording from living animals, as well as understand and treat health conditions affecting nervous system [25-30], requires high-density interconnects between the animal and the electronics. These *in vivo* recordings add further

limitations pertaining to the materials that can be utilized to maintain bio-compatibility. Moreover, chronic recordings require robust devices that can record over long duration of time while consistently providing a high SNR and prevent damage to the living tissue.

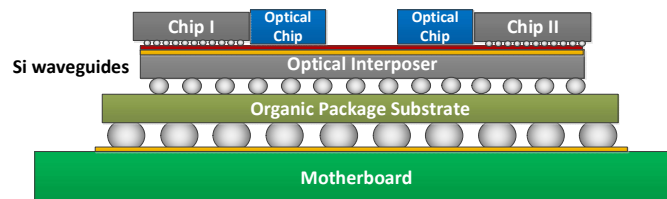
1.2 Current methods and relevant research



(a)



(b)



(c)

Figure 4 Silicon based (a) electrical interposer, (b) EMIB and (c) optical interposer – fine pitch wires and waveguides achievable on silicon enables high-density communication

1.2.1 Trends in heterogeneous integration

In recent years, silicon interposers (Figure 4(a)) have been extensively explored for various benefits including higher bandwidth density, heterogeneous integration and reduction in form factor [3]. Dense wiring on silicon interposers allows higher aggregate bandwidth between chips. Assuming a stripline differential pair pitch of $22\ \mu\text{m}$ [31] for interconnect on silicon interposer and channel data rate of 10 Gb/s, the achievable bandwidth density is $\sim 450\ \text{Gb/s/mm}$. The energy efficiency of such a link of length 4 cm is 5.3 pJ/bit [31]. Based on the 2.5 D integration platform, there have also been different topologies presented leveraging the key benefits of the interposer technology while addressing cost, energy or packaging challenges. For example, Intel's embedded multi-die interconnect bridge (EMIB) packaging [8], shown in Figure 4(b), reduces the overall silicon area on package (compared to using a silicon interposer) and reduces the overall cost when compared to conventional interposer technology.

Integration of nanophotonic to form optical interposer (Figure 4 (c)) has also been widely researched as it allows a significantly higher bandwidth density using fine pitch silicon waveguides [5, 9] and WDM. Assuming a waveguide pitch of $10\ \mu\text{m}$ [32] with 8 WDM channels and each channel operating at 10 Gb/s, the bandwidth density achievable using nanophotonics integration on interposer is $\sim 8\ \text{Tb/s/mm}$. This is clearly a attractive option. However, again, the EPB expensed in electrical to optical conversion and vice versa, along with the laser efficiency dictates the interconnect length after which utilization of nanophotonic interconnect becomes feasible in terms of power dissipation. Oracle's macrochip [1, 33] architectures aim to leverage silicon nanophotonic integration to form a large passive grid of silicon waveguides embedded in a silicon lattice; the LSI chips

(processors, RAM modules etc.) are connected to the lattice via a ‘bridge’ chip that converts the electrical signal to optical and couples it into the waveguide network [33, 34]. The proposed architecture can potentially operate at very low EPB (including laser power) and can enable high bandwidth communication between chips using WDM [35]. In [36], Thacker *et al.* demonstrate an all-solid-state WDM link with energy efficiency of 4.23 pJ/bit.

The mechanical reliability of the I/Os is also becoming increasingly critical with a greater trend towards heterogeneous 2.5D and 3D integration of disparate substrate materials which results in CTE mismatch and an increased number of off-chip I/O demand [37-41]. Flexible interconnects have been widely explored as a suitable replacement for the conventional solder bumps and copper pillars as I/Os [42-52]. These flexible interconnects enable temporary pressure-based interconnects and allow compensation of any surface non-planarity or CTE mismatch between disparate substrates. Utilizing compressible interconnects along with fine-pitch micro-bumps, Zhang et al. have proposed HIST [101,

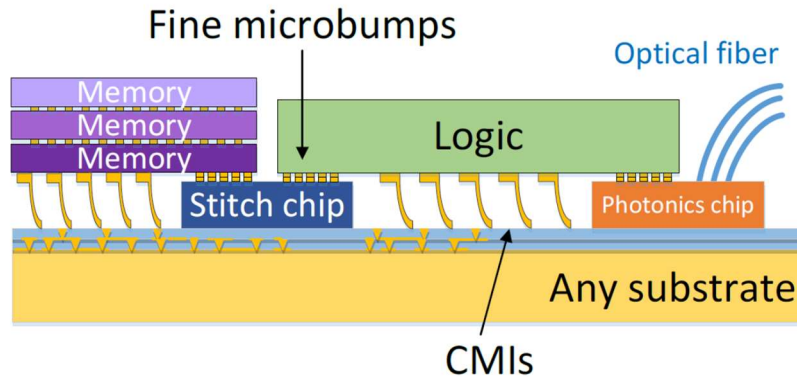


Figure 5 Schematic of the HIST platform [101]

[102] platform allowing close integration of disparate substrates. The flexible interconnects

provide chiplet-package interconnection while compensating for surface non-planarities. The proposed HIST system is shown in Figure 5.

Alongside the research efforts to advance heterogeneous integration, there is an increasing push towards integrating passives e.g. inductors, capacitors etc. on, or in close proximity to, the chips [15] as they are an integral part of various radio frequency (RF) circuits including filters, amplifiers, oscillators and transceivers with applications in communication, sensing and power delivery domains [11-14]. On-chip inductors of planar structures have been traditionally preferred owing to their ease of fabrication and CMOS compatibility. However, these inductors typically suffer from large substrate losses as well as limited footprint due to a large number of metal interconnects in back-end-of-line, resulting in limited inductor performance [53]. Three-dimensional (3D) inductors have been explored to circumvent some of the issues of planar inductors. Specifically, solenoidal micro-inductors have been preferred as high inductance and low-loss are achievable owing to better magnetic field confinement [54]. However, the additional processing steps and complex fabrication procedures have prevented mass adoption. Moreover, additional fabrication steps are required to fabricate the needed I/Os for interconnections [55]. Table 1 summarizes some of the significant efforts in 3D micro-inductors along with their key metrics.

Table 1 Summary of relevant published work on 3D inductors

Reference	Peak Q @ (f_{qmax})	Bandwidth for Q > 15 (GHz)	L (nH)	SRF (GHz)	Substrate	Inductor shape	Co- fabrication with I/Os
[55]	100 (3.2 GHz)	< 8	3.5	n/r	Glass	3D solenoid	No
[56]	17.5 (70 MHz)	< 0.1	60	n/r	Silicon	3D toroidal	No
[57]	46 (400 MHz)	n/r	38	n/r	Glass	3D solenoid	No
[58]	50 (6 GHz)	< 7	2.3	> 20	Silicon	3D solenoid	No
[59]	32 (0.95 GHz)	< 0.5	1000	1.24	Polymer	3D solenoid	No

1.2.2 Trends in biosensing systems for *in vitro* and *in vivo* measurements

As discussed in section 1.1, cell-based sensing techniques require the growth of cells onto the biosensor's surface; both the successful adhesion and growth of these cells onto the biosensor are pivotal for meaningful sensing and are strongly affected by the type of material and the surface roughness [60-66]. Growth of human cells on a multi-modality CMOS biosensor has been shown in [67].

Growing cells directly onto the biosensor is tedious due to the surface treatments required to enhance bio-compatibility and culture cells. Additionally, culturing cells directly onto the CMOS biosensor may be expensive because it is difficult to re-use as it must undergo a rigorous cleansing process or disposed of to avoid contamination. Moreover, even after cleaning and sterilizing the CMOS biosensor surface, the biosensor might not be suitable for re-use if the cell type or the biochemical stimulus to be tested are different.

Contamination poses a perpetual risk to the proper functionality of the CMOS biosensor. Furthermore, any electrical connections to the board (e.g. wire bonds in [67]) and culture medium sealing (e.g. PDMS sealing in [67]) need to be replaced for a new sample during which there is a high likelihood of damaging the CMOS biosensor and/or interconnects.

Although disposable plastic micro-electrode arrays (MEAs) have been used to address some of these challenges, they suffer from significant performance degradation as the density of electrodes achievable is far less than that in silicon-based biosensors. 3D integration approach had been discussed by Y. Temiz et al. in [68], however, the complex fabrication, specifically implementing reliable interconnection between biosensor and cells, has prevented successful implementation of the concept.

In the *in vivo* biosensing domain, advances in data analysis methods in neuroscience have provided new insights on how a nervous system controls complex behaviors such as vocal learning and song production in songbirds [69, 70]. Recent evidence [24, 71] has pointed to the importance of precise timing of individual motor units for controlling behavior and showed that EMG activity can be used to understand how nervous systems produce behaviors.

Understanding how nervous systems produce behaviors requires recording devices that can provide high-density interconnects capable of providing reliable recordings along with algorithms that can identify individual motor events, called muscle potentials. Among the challenges involved with obtaining high fidelity recordings suitable for neural analyses are: biological compliance of recording devices [72] and the signal-to-noise ratio. In addition, characterizing single motor unit activity requires a stable, reliable EMG recording for a

duration long enough to produce sufficient data for advanced computational analyses [73,74].

Polyimide, PDMS and parylene-C have been widely used for the fabrication of high-density multi-electrode arrays [75-80]. To increase the signal fidelity, three-dimensional neural and muscular recording devices have also been explored [76-80]. However, these involve complex processing methodologies increasing the fabrication complexity, cost and time.

1.3 Organization of this thesis

With the background discussed in Section 1.2, this thesis aims to further advance the state-of-the-art in heterogeneous integration and addresses the need for high-density interconnects needed for electronic heterogeneously integrated systems, *in vitro* cell based assays and *in vivo* EMG recordings. This is accomplished by developing 3D and 2.5D microfabrication technologies which merge some of the widely used processes, structures and substrates from rather disparate disciplines to provide unique solutions in the two domains discussed in Section 1.2. In particular, thick photoresist reflow process, which is primarily utilized for flexible interconnect fabrication, will be utilized as an enabling technology for realizing large-scale silicon system capable of both electrical and optical interconnects as well as provide temporary 3D interconnections for *in vitro* biosensing applications. This technology will be further modified to incorporate simultaneous fabrication of micro-inductors as well as fabricate 3D electrodes on a bio-compatible flexible substrate for bio-signal recording. The core processes utilized for the research contributions of this thesis are summarized in Figure 6.

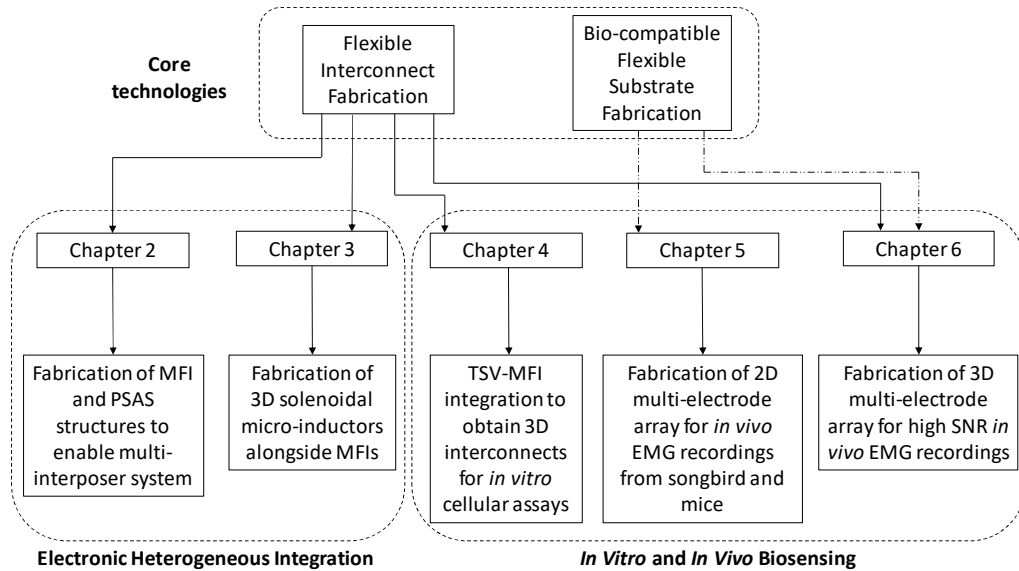


Figure 6 Summary of core technologies enabling the presented research in this thesis

The thesis is organized as follows:

1. Realization of a large-scale silicon system utilizing flexible interconnects and self-alignment structure is discussed in Chapter 2; a prototype system with two interposers assembled directly onto the FR4 substrate with a silicon bridge utilized to provide high-density interconnects between the interposers is shown. System level modelling showing trade-off between bandwidth-density and energy-per-bit expended for electrical and optical interconnects is also discussed.
2. Chapter 3 introduces a unique fabrication process enabling simultaneous fabrication of 3D solenoidal micro-inductors and high-density flexible interconnects for heterogeneously integrated systems; the fabrication process further enables fabrication of flexible interconnects of various heights, pitches, material and thickness giving high degree of flexibility in system design.

3. Fabrication and characterization of an electronic microplate, providing high-density 3D interconnects between living cells and biosensor, is presented in Chapter 4. The e-microplate provides an electrical connection between the cells and the biosensor while maintaining a physical separation; this allows for the reuse of the biosensor resulting in an increase in throughput of assays and reduced cost.
4. Chapter 5 introduces high-density micro-electrode arrays on flexible substrates for *in vivo* recording from songbird and mouse. The fabricated MEAs utilize a hybrid polyimide-PDMS process allowing ease of fabrication. EMG measurements from a songbird using 100 μm , 200 μm and 300 μm pitch MEAs are presented. The recordings from the fabricated MEAs show significant improvement over the fine-wire electrodes and comparable SNR with other relevant MEAs while providing a simpler fabrication process.
5. Chapter 6 extends the work presented in the previous chapter and presents a 3D MEA on flexible substrate. The fabrication process utilized a photoresist reflow process, adapted from Chapter 3, for the fabrication of the 3D electrodes and a thick PDMS top layer for insulation. The results show up to 7x improvement in SNR when compared to 2D arrays.

CHAPTER 2. MULTI-INTERPOSER SYSTEM UTILIZING FLEXIBLE INTERCONNECTS

The 2.5D and 3D integration technologies discussed in Section 1.1 enable high-bandwidth low-energy communication between chips. However, all of them have shortcomings and some trade-off is necessary in lieu of the benefits that the technologies bring; while the EMIB technology enables high-bandwidth communication between chips connected via the bridge, it increases the package complexity and substrate processing. Furthermore, EMIB technology is specific to chips that are spatially in close proximity in the package and high-density communication is only between adjacent chips on the package. Moreover, since the platform doesn't currently support optical communication, it cannot take advantage of WDM to achieve higher aggregate bandwidths.

On the other hand, optical interposer based approaches like the Oracle's macrochip vision portray an aggressive target allowing high bandwidth low-energy communication between chips that are even spatially further away. However, the assembly and packaging of large silicon lattice with embedded VLSI chips may pose a number of challenges that need to be overcome before the system can be realized. Furthermore, as optical communication is feasible for relatively longer distances, the chips that are in close proximity would expense unwanted energy if only optical communication is used.

Likewise, 3D integration poses a unique set of challenges introduced by stacking chips; thermal management of stacked dice, especially with high power dice such as processors present in the stack, becomes a critical issue. Also, wafer-to-wafer bonding and sequential

testing of stacked dice poses additional challenges that need to be overcome before large scale adoption of the technology [81-83].

The shortcomings of these technologies are exacerbated by the fact that the number of VLSI chips needing to be integrated in a system are continuously increasing. Thus, incorporating all of these chips on an interposer would require a very large silicon interposer, which will pose mechanical handling and cost challenges. Similarly, having a 3D stack with ever increasing number of stacked chips would further amplify the current challenges. Thus, there remains a need for a large-scale silicon system that allows high density electrical and optical communication between chips and extends beyond the physical limits of an interposer. The next subsection describes one approach to realize this large-scale silicon system along with its enabling technologies.

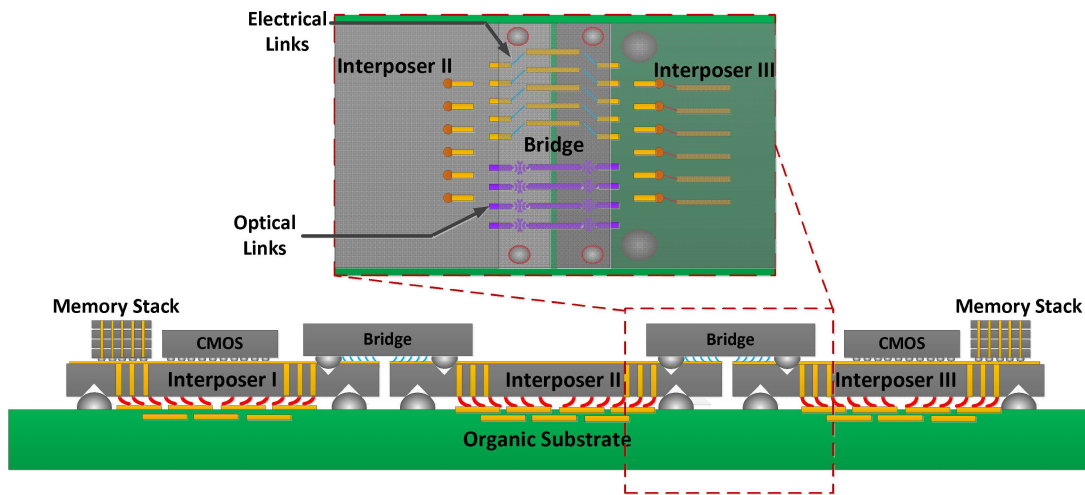


Figure 7 Two interposer tiles mounted on FR-4 interconnected using silicon bridge

2.1 System Overview

The discussion thus far motivates the utilization of interposers with electrical and optical interconnects as it can provide highest bandwidth density and efficient energy utilization compared to other methodologies discussed. It also motivates a packaging solution that allows extension of bandwidth and energy benefits of an interposer beyond the physical and practical limits. In this context, Yang et al. [84], have proposed using silicon bridges to bridge adjacent interposer ‘tiles’. Figure 7 shows an overview of the silicon-bridged multi-interposer system platform. The interposer tiles are directly mounted onto the FR-4 thereby eliminating package substrate; four positive self-alignment structures (PSAS) are fabricated on the FR-4 corresponding to the inverse pyramid pits on the interposer tiles to provide low-cost high accuracy alignment. Dense mechanically flexible interconnects (MFIs) are utilized to provide reliable interconnections to the motherboard as well as adjacent interposer via silicon bridge while overcoming coefficient of thermal expansion (CTE) mismatch and surface variations [86]. Optical waveguides can also be incorporated in the platform utilizing grating couplers to couple the light from one interposer to the other interposer via the silicon bridge. The silicon bridge allows one to extend the high-bandwidth fine pitch connections possible on an interposer beyond the physical limits of the interposer. Thus, the silicon-bridged multi-interposer system emulates a contiguous piece of large silicon allowing high density communication between interposers. The work described in the following sections extends the work presented in [84] and presents double-sided MFI fabrication, RF characterization of the MFIs and a system level bandwidth and energy per bit analysis for bridged multi-interposer system.

2.2 Fabrication and Assembly

2.2.1 Key Technology Enablers

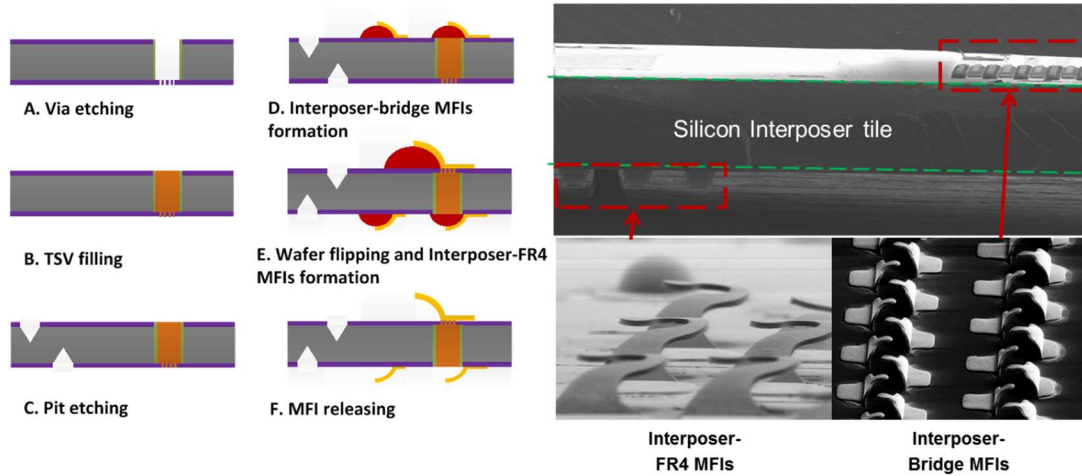


Figure 8 Double-sided MFI fabrication process

MFIs are an integral enabling technology for the realization of the system under consideration; Figure 8 shows the fabrication flow for double-sided MFIs on interposer, which extends the fabrication process of MFIs from [85]. A double-side polished wafer is utilized for the fabrication allowing fabrication of MFIs on both sides. Photolithography is used to pattern thick photoresist, AZ-40XT, to obtain the desired structures. The resist was then reflowed to obtain the hemispherical domes. After the formation of the reflowed photoresist domes, a Ti/Cu/Ti seed layer with a 50nm/300nm/30nm thickness was deposited. The electroplating mold was fabricated by spray coating 10 μm thick AZ-4620 photoresist. Once the MFIs were electroplated on one side, masking tape was used to protect that side followed by fabrication of MFIs on the other side. Once the electroplating was completed, MFIs on both sides were released by removing the photoresist and the seed layer. The MFIs are fabricated using NiW; the higher yield strength of NiW as compared

to copper [86] allows extended range of elastic motion for the fabricated MFIs. The MFIs connecting the motherboard to the tiles are fabricated at 200 μm pitch with a height of 70

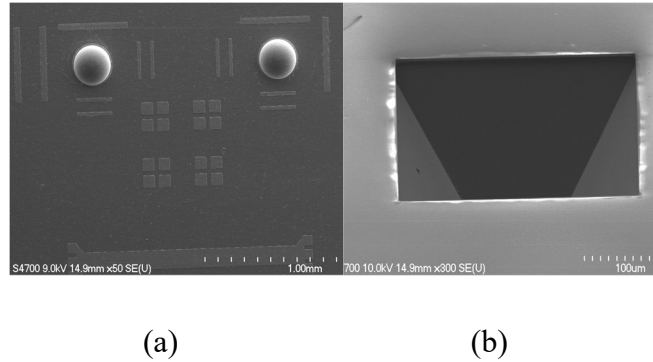


Figure 9 (a) PSAS on bridge (b) inverse pyramid pit

μm and are 7 μm thick. The MFIs connecting the interposer tiles to the bridge are fabricated at 100 μm pitch with a height of 12 μm and are 5 μm thick. An array of MFIs with 50 μm pitch has also been demonstrated to enable high-density I/Os between an interposer and bridge. The electroless gold plating passivates the MFIs and prevents any oxidation ensuring a good contact.

Another key enabling technology for the silicon-bridged multi-interposer system is the self-alignment utilizing PSAS and inverse pyramid pits, as shown in Figure 9. The inverse pyramid pits are fabricated using KOH etch of silicon using nitride mask. Photolithography using the NR5 negative resist was first used to create 300 μm x 300 μm openings. Reactive-ion-etching was then used to etch the nitride mask for subsequent wet etch. The wafer was then placed in a 45% KOH bath for 6 hours to fabricate the pits. The dimensions of the pits on both sides of the interposer are kept at 300 μm x 300 μm . The PSAS are also fabricated using reflow of AZ-40XT photoresist [84]. The resist is first spin coated at 1250 rpm. The

soft bake, exposure, post-exposure bake and developing parameters were kept the same as that used for the MFIs. The gap between the substrates is controlled by tuning the height of the PSAS [84]. For the described system, PSAS are fabricated on both the FR-4 and the glass or silicon bridge while the interposer has the pits etched on both sides. The PSAS-pit duo enables precise control over the gap between substrates, which is a critical factor determining the optical coupling loss. The fabricated TSVs provide the necessary interconnections between the two sides of the interposer. The SEM images of these key enabling technologies are shown in Figure 10.

2.2.2 System assembly

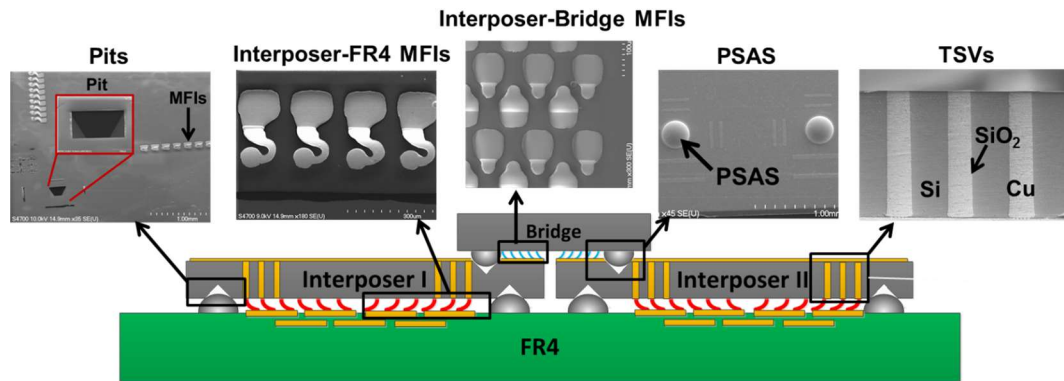


Figure 10 Demonstrated technology enablers for the proposed multi-interposer heterogeneous system

During the assembly process, the interposers were coarsely aligned to the FR-4 using a flip-chip bonder and the PSAS-pit duo enabled the fine alignment after placement. Epoxy was then used to hold the interposers in place. Once the tiles were secured on FR-4, similar process was repeated for the bridge placement. Figure 11 shows the assembled system with two pairs of interposer tiles; each interposer is 2 cm x 2 cm and is mounted directly over a 2.5-inch x 2.5-inch motherboard leaving a 200 μm gap between the interposers. The top assembly shows the tiles bridged using silicon while the bottom assembly shows bridging using glass. Both the bridges are 0.5 cm x 2 cm.

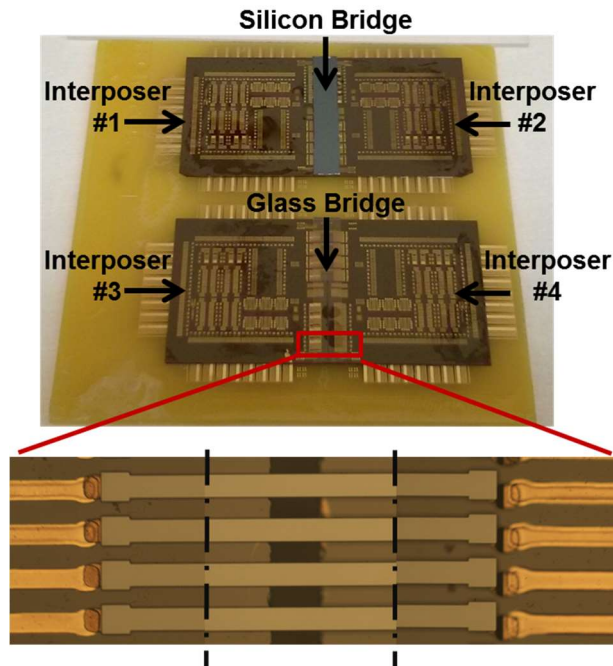


Figure 11 Assembly of multiple interposers with glass

2.2.3 Electrical Characterization

RF simulation and measurements for the interposer-FR4 MFIs were performed from 100 MHz to 50 GHz. The 3D model of the MFIs, shown in Figure 12, was also simulated in

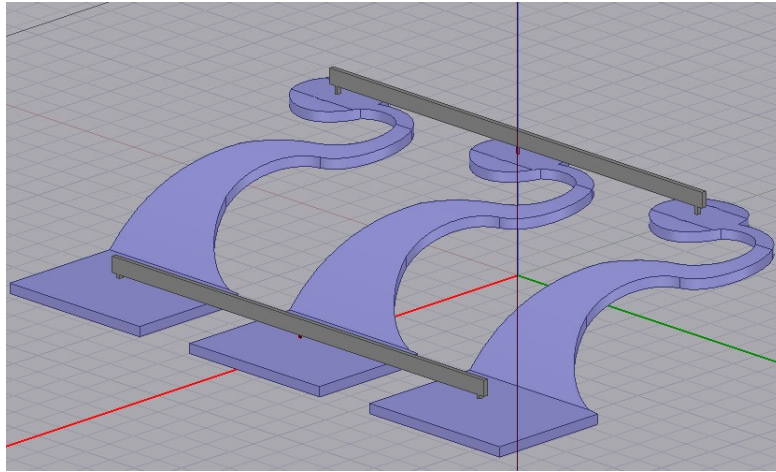


Figure 12 Simulation setup for the MFIs

HFSS for the same frequency range. The relative permeability of the Ni was set to 1 for the simulations. A dedicated RF probe station with Agilent N5245A PNA-X network analyzer and Cascade $|Z|$ probes, as shown in Figure 13 was used for the S-parameter measurements. Figure 14 (a) shows the measured and simulated S_{11} and S_{21} for the interposer-FR4 MFIs. The measured loss for these MFIs at 20 GHz is ~ 0.3 dB; the insertion loss of a 60 μm high solder ball is ~ 0.1 dB at 20 GHz [87]. Table 2 also summarizes the insertion loss of select compliant interconnects in literature along with solder bump. The fabricated MFIs exhibit lower loss than some of the other compliant interconnects while having the largest total height of the interconnect structure. Although the loss of the solder ball is lower than that of the MFI, the elimination of the package layer and overcoming CTE mismatch provides significant advantages at system level.

Furthermore, it allows replaceability of components by allowing temporary pressure-based interconnections.

To study the flexibility and effect of mechanical deformation on the electrical performance of these MFIs, three measurements were taken. An initial measurement was taken without

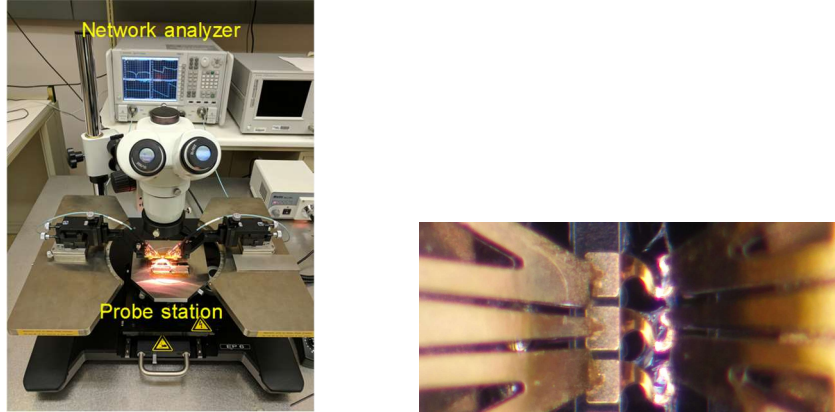


Figure 13 Experimental setup with RF probing of interposer-FR4 MFIs

Table 2 Insertion Loss Comparison for Compliant Interconnects and Bump

Reference	Structure (Total height in μm)	S_{21} @ 20 GHz
[42]	Double-turn helix (25)	~ 0.35 dB
[43]	Double helix (N/R)	~ 0.6 dB
[88]	Solder Bump (60)	~ 0.1 dB
[102]	Compressible MicroInterconnect (55)	~ 0.8 dB
[This work]	Flexible Interconnect (70)	~ 0.3 dB

any deformation. The second measurement was taken after fully deforming the MFIs. Third measurement was performed after 10 deform-recover cycles; in each cycle, the MFIs were deformed to the full vertical range of motion and then recovered. Figure 14 (b) shows the S_{21} of the MFIs under the three scenarios described above. When fully deformed, the MFIs show minimal change in RF characteristics. Similarly, the effect on RF performance after 10 deform-recover cycle is negligible and the measurement after 10 deform-recover cycles matches closely to the initial measurement.

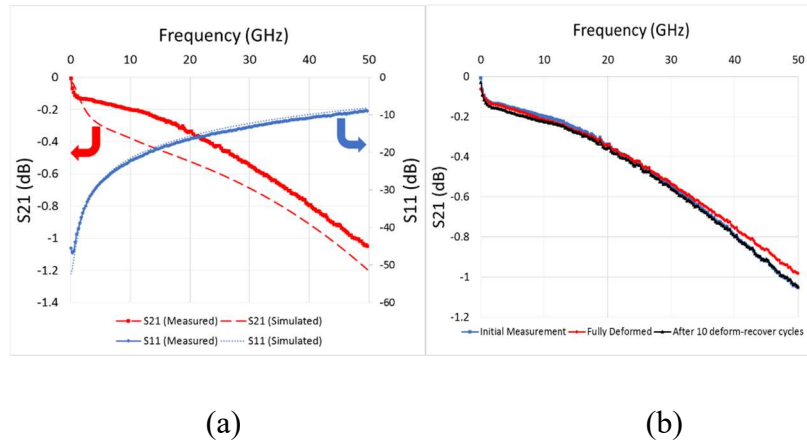


Figure 14 (a) Measured and simulated S_{11} and S_{21} parameters for MFI, (b) comparison of S_{21} parameter before and after deformation cycles

The measured data for the interposer-FR4 MFIs was also used to extract the RLGC parameters. The measured S-parameters for initial, fully deformed, and cycled MFIs were converted into corresponding Y- and Z-parameters using MATLAB. RLGC were then extracted using the following equations [88]:

$$R = Re (Z_{11} + Z_{22} - Z_{12} - Z_{21}) \quad (1)$$

$$L = Im (Z_{11} + Z_{22} - Z_{12} - Z_{21}) \quad (2)$$

$$G = \text{Im} (Y_{11} + Y_{22} - Y_{12} - Y_{21}) \quad (3)$$

$$C = (\text{Im} (Y_{11} + Y_{22} - Y_{12} - Y_{21}))/\omega \quad (4)$$

The results for the extracted RLGC parameters for 5, 10, 25 and 50 GHz frequency points are summarized in Table 3. The difference in the resistance of the MFIs is most likely due to the work hardening the interconnects go during the deform-recover cycles. The work hardening introduces defects and increases the electrical resistance of the MFIs [89].

Table 3 Extracted RLGC Parameter for the Interposer-FR4 MFIs

Measurement	Para- meters	5 GHz	10 GHz	25 GHz	50 GHz
Initial Measurement	R (Ω)	1.08	1.19	1.76	1.69
	L (nH)	0.17	0.17	0.16	0.15
	G(mS)	0.53	0.99	2.50	4.01
	C (fF)	17.00	15.90	15.60	12.80
Fully Deformed	R (Ω)	1.14	1.36	1.90	1.82
	L (nH)	0.17	0.16	0.16	0.15
	G(mS)	0.60	1.16	2.75	4.55
	C (fF)	19.00	17.80	17.50	14.50
Stressed (20 deform-recover cycles)	R (Ω)	1.37	1.50	1.99	1.87
	L (nH)	0.17	0.16	0.16	0.14
	G(mS)	0.54	1.00	2.47	4.03
	C (fF)	17.00	15.90	15.70	12.80

2.3 System-level Analysis

Figure 15 (a) shows the assembled system consisting of two interposer tiles mounted directly on FR-4 and bridged using silicon bridge. The demonstrated system can be extended to have a 2-dimensional interconnected array of interposers. Top view of the different array sizes analyzed in this chapter are shown in Figure 15 (b). All tiles are taken to be 2 x 2 cm in size and the distance between the tiles is assumed to be negligible so that the center to center distance between tiles is 2 cm. For such large-scale systems, it is essential to utilize interconnection scheme that gives the highest bandwidth at the lowest energy consumption. For the analysis that follows, the width of the electrical wire on the interposer is taken to be the one that maximizes the BWD/EPB, as shown in Figure 16. It can be seen from the figure that, for example, 2.5 μm wire width would maximize the BWD/EPB for a 2 cm long wire on interposer. Channel pitch for electrical interconnects is calculated assuming stripline structure with differential signaling and wire spacing equal to two-thirds of the width. The EPB for the electrical interconnects is calculated assuming

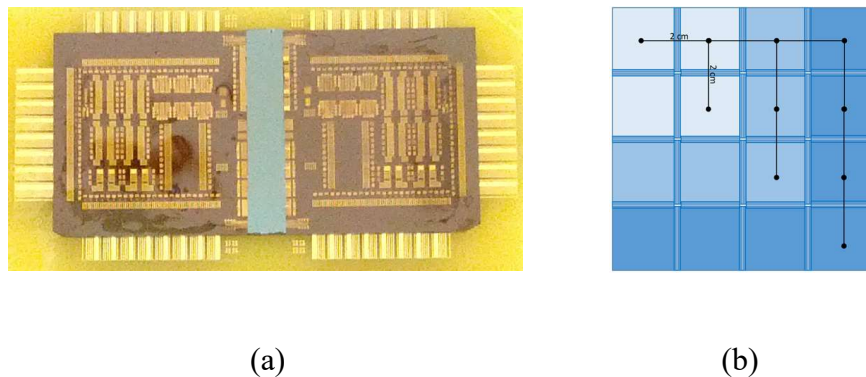


Figure 15 (a) Assembled system with 2 interposer tiles bridged using silicon bridge (b) top view of multi-interposer system array – center to center distance between adjacent interposers is taken to be 2 cm

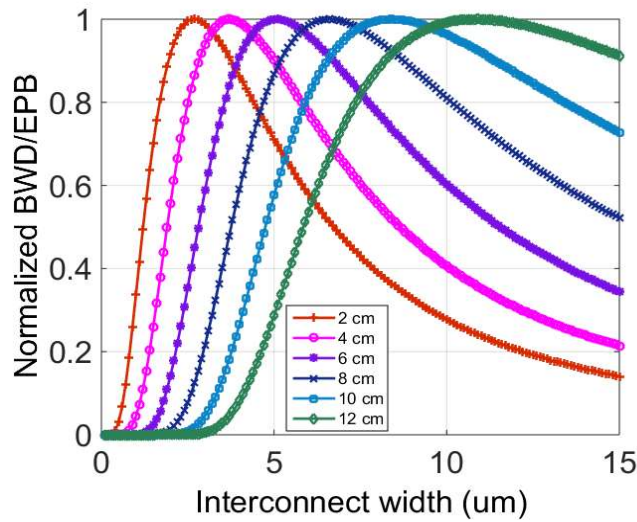


Figure 16 Optimal width for different lengths of wires on interposers that maximizes BWD/EPB

a stripline structure with differential voltage mode signaling scheme [90]; the geometric dimensions of the transmission line are used to extract the R, L, C and G parameters; propagation constant is then determined based on these parameters. Using the receiver noise condition for a maximum BER of 10^{-12} , the minimum driving current is calculated which is then used to find the total loss in the transmission line [90]. Figure 18 shows the flowchart for calculating the EPB and BWD for the electrical transmission line.

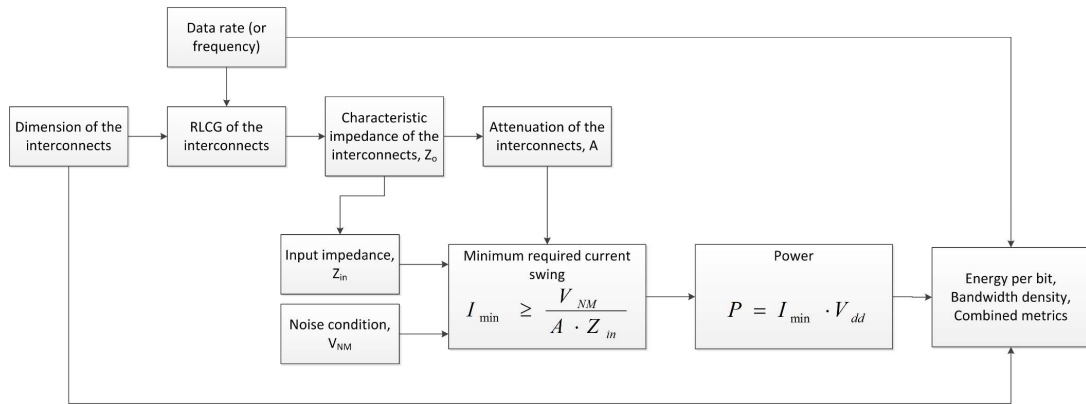
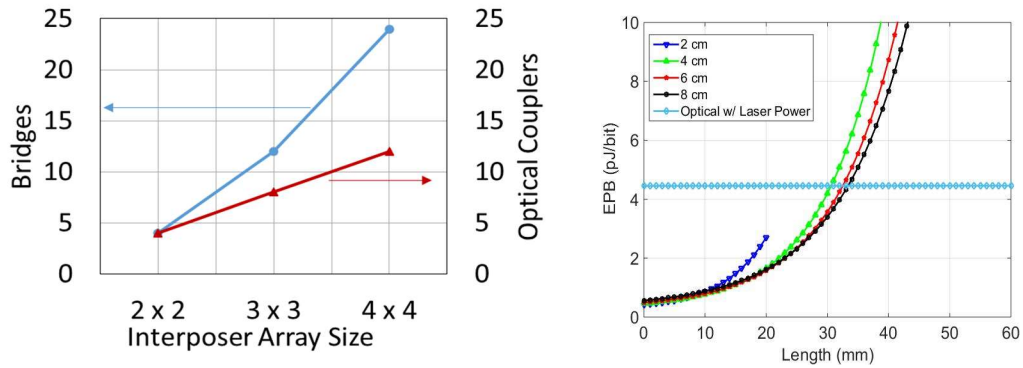
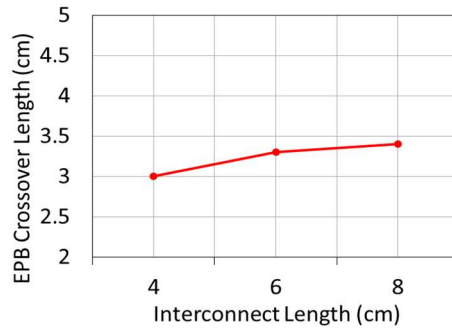


Figure 18 Modelling flowchart for BWD and EPB calculation



(a)

(b)



(c)

Figure 17 (a) Number of optical couplers and silicon bridges with array size, (b) EPB comparison of four different lengths' electrical interconnects with optical interconnect and (c) crossover length – interconnect length after which electrical interconnect link dissipates more energy after this length

The EPB analysis for the silicon photonic based optical interconnect has been adapted from [16]. The average transmitter and receiver electrical power is taken to be 6.93 and 4.26 mW respectively [16]. The excess loss caused by the optical couplers in the bridged interposer system is compensated by increasing the on-chip optical power to maintain a constant BER of 10^{-12} . The wall plug efficiency of the laser is taken to be 9.5% [91] and the coupling loss is assumed to be 1 dB. The EPB for electrical transmission lines is a strong function of the interconnect length. Silicon photonic based interconnects' EPB is dominated by the fixed overhead from transmitter and receiver. The silicon-bridged multi-interposer system is different from other large scale optically connected systems in the fact that each tile hop requires 2 optical couplings. The number of optical coupler pairs in the longest link, along with the number of bridges in the system as a function of interposer array size is shown in Figure 17 (a). Figure 17 (b) shows the EPB of electrical interconnects on silicon-bridged multi-interposer system for 4 different lengths, along with the EPB of optical interconnect. The width of each of these interconnects is taken to be the optimized width that maximizes the BWD/EPB metric (Figure 17 (c) also shows the crossover length after which the electrical interconnects on interposer would expense more EPB than the silicon photonic interconnects as a function of total interconnect length. As seen from the figure, EPB line for 2 cm long electrical interconnect does not surpass that of the optical interconnect; For a case where the longest distance to be traversed is 4 cm (2 x 2 interposer array), the cross over length is ~ 3 cm. Hence, based on above set of assumptions, any electrical interconnect below this length would expense less EPB when compared to the silicon photonics-based interconnect. It can also be seen that the cross over length remains almost unchanged for longer length. Thus, for silicon bridged systems where high

bandwidth communication is required for over 3 cm distance, silicon photonics-based interconnects may provide a lower energy alternate to electrical interconnects.

2.4 Conclusion

With the perpetual increase in bandwidth requirements of chip-to-chip communication, it is imperative that an all-encompassing solution be devised – one that allows high-bandwidth low-energy communication for both short and long reach interconnects. Conventional interconnects through the motherboard suffer from coarse channel pitch and the need for higher equalization taps for longer range. While flex-based interconnects bypass the package and motherboard, the channel pitch still limits the bandwidth density achievable. Optical interconnects at motherboard level are a promising alternate, however, the relatively coarse waveguide pitch and added package complexity makes them less attractive. Silicon interposer based electrical interconnects allow high-bandwidth communication owing to the fine pitch achievable. However, long fine pitch wires on silicon quickly become very lossy and expense very high EPB. This has motivated efforts in the optical interposer regime which allows ultra-high bandwidth communication owing to the fine waveguide pitch and WDM. However, as the link EPB is dominated by the transmitter and receiver loss and the laser wall plug efficiency, the silicon nanophotonic links expense far more EPB at shorter lengths than the electrical interconnects. Although having a physically large interposer allows integration of multiple chips on the same substrate enabling high density communication, the cost and mechanical handling of such large interposers are not feasible. The silicon-bridged multi-interposer system described in this chapter, which extend the work presented in [84], provides a viable alternative that allows the extension of high bandwidth density of an interposer beyond the practical limits.

It further enables both electrical and optical communication for short and long reach interconnects. The self-alignment technology allows submicron alignment accuracy that ensure low optical coupling loss which is imperative for nanophotonic link integration. The modelling work presented in this chapter further provides a framework to direct research efforts towards either electrical or optical interconnects based on the size of the system.

With the demand for off-chip bandwidth projected to continue to grow, large scale silicon systems, like the silicon-bridged multi-interposer system, are likely to come into more and more use. It is also foreseeable that coexistence of electrical and nanophotonic interconnects would be critical in achieving low energy interconnects for short and long reach chip-to-chip interconnects.

CHAPTER 3. CO-FABRICATION OF 3D SOLENOIDAL MICRO-INDUCTORS WITH FLEXIBLE I/OS

Chip I/Os play an integral role in not only providing reliable electrical interconnections but also the mechanical reliability of the overall system. The mechanical reliability of the I/Os is becoming increasingly critical with a greater trend towards heterogeneous 2.5D and 3D integration of disparate substrate materials which results in CTE mismatch and an increased number of off-chip I/O demand [20-26]. Flexible interconnects have been widely explored as a suitable replacement for conventional solder bumps and copper pillars as I/Os [25-29]. Furthermore, there is also a push towards integrating passives (e.g. inductors, capacitors etc.) on, or in close proximity to, the chips [92] as they are an integral part of various radio frequency (RF) circuits including filters, amplifiers, oscillators, and transceivers with applications in the communication, sensing, and power delivery domains [93-96]. On-chip inductors of planar structures have been traditionally preferred owing to their ease of fabrication and CMOS compatibility. However, these inductors typically suffer from large substrate losses as well as limited footprint due to a large number of metal interconnects fabricated in back-end-of-line, resulting in limited inductor performance [97]. Three-dimensional (3D) inductors have been explored to circumvent some of the issues of these planar inductors. Specifically, solenoidal micro-inductors have been preferred as high inductance and low-loss is achievable owing to better magnetic field confinement [98]. However, the additional processing steps and complex fabrication procedures make them less feasible for integration. Moreover, additional fabrication steps are required to fabricate the needed I/Os for interconnections [99].

In this chapter, post-CMOS wafer-level co-fabrication of 3D solenoidal micro-inductors with mechanically flexible interconnects (MFIs) of different materials, pitches, thicknesses, and heights for electrical signaling is reported; the described process allows simultaneous fabrication of I/Os (MFIs) and micro-inductors thereby preventing additional fabrication steps. A double lithography and double reflow process [100] is utilized to get the differential height photoresist domes for micro-inductors and MFIs; smaller height domes are utilized to fabricate fine-pitch MFIs along with micro-inductors while the larger domes are used for the coarse pitch MFIs. The developed process further allows the MFIs to be fabricated using different materials, pitches, and thicknesses giving control over the mechanical and electrical properties of the MFIs. This can be important for heterogeneous integration where I/Os of different pitches, heights and materials maybe required for increased integration flexibility.

Figure 19 shows a schematic of one such topology leveraging multi-height I/Os [101, 102] and 3D micro-inductors. As shown in this chapter, the high-density stitch chip can be fabricated out of a low-loss substrate allowing high performance 3D passives (inductors) along with low-loss, high-density electrical interconnects. The fabrication process enables seamless heterogeneous integration of ICs of different substrate materials utilizing I/Os of different heights, materials, and pitches; fine-pitch Cu MFIs can enable high-density communication between chips using high-density interconnect technologies, including embedded multi-die interconnect bridge (EMIB) [8, 103] and heterogeneous interconnect stitching technology (HIST) [101, 102]. The coarse pitch NiW MFIs can provide the necessary interconnection between the bottom substrate and the chips while providing a

greater vertical elastic range of motion, owing to the higher yield strength of NiW as compared to Cu [86], to compensate for height differences and surface non-planarities.

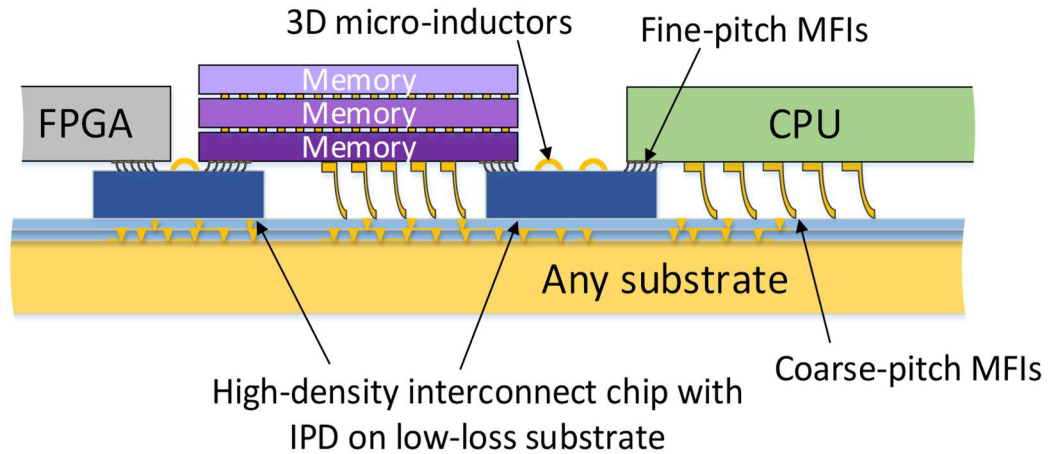


Figure 19 Envisioned schematic utilizing fabricated micro-inductors and MFIs; figure extends HIST [101, 102]

3.1 Fabrication

The co-fabrication process of the MFIs and the micro-inductors is outlined in Figure 20. A Ti/Cu/Au metallization, with a thickness of 50/2000/100 nm, using a lift-off process is obtained to get the base metallization for the micro-inductors. Large domes are obtained using reflow of thick positive photoresist as described earlier in Section 2.2.1. A second exposure is then performed followed by a second reflow process to get the smaller domes [100]. Figure 21 shows a profilometer scan for the two different dome heights obtained after the second exposure and reflow. A height differential of 70 μm is achieved between the large and the small domes. The height differential between the domes can be modulated

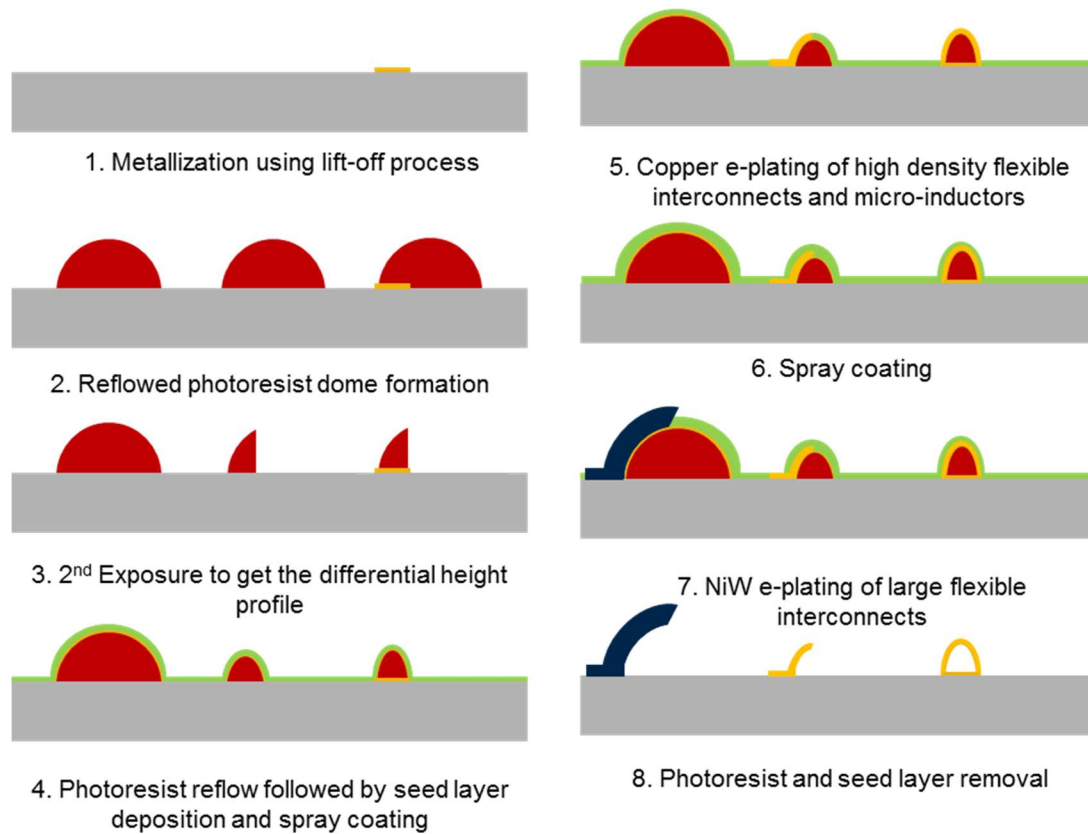


Figure 20 Fabrication process for micro-inductors and MFIs

by changing the width of the photoresist being exposed in the second exposure. After the differential height domes are obtained, the metal seed layer and spray coated photoresist is deposited for subsequent electroplating processes. Copper electroplating of small MFIs and micro-inductors is then performed using the spray coated electroplating mold. After the copper electroplating, a second layer of spray coated photoresist is applied to isolate the copper plated structures and create a new electroplating mold for the large MFIs. An optical image of the spray coated copper micro-inductors and fine-pitch MFIs and the electroplating mold for the NiW MFIs is shown in Figure 22. NiW is used to electroplate

the large MFIs allowing for larger vertical elastic deformation than copper [86]. Seed layer and photoresist are then removed to obtain free-standing structures.

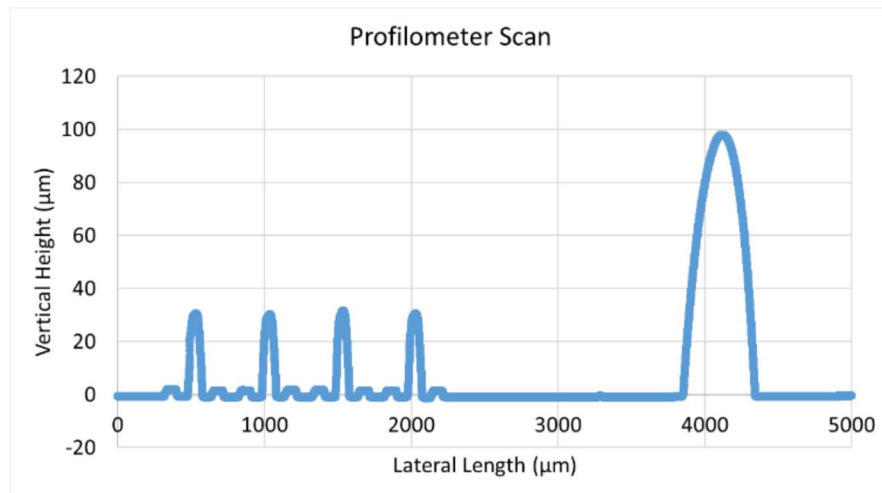


Figure 21 Profilometer scan of the reflowed domes after double-exposure process – height difference of 70 µm between the small and the large domes was achieved

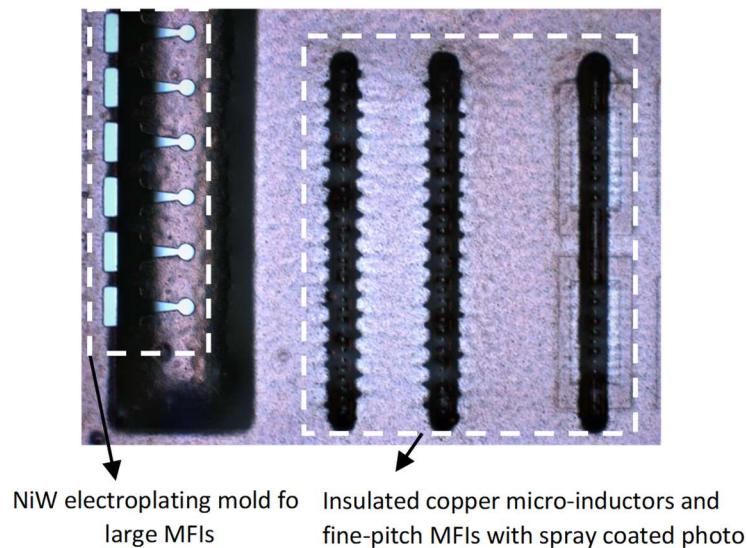


Figure 22 Optical image showing electroplating mold for large NiW MFIs with resist covered copper micro-inductors and MFIs

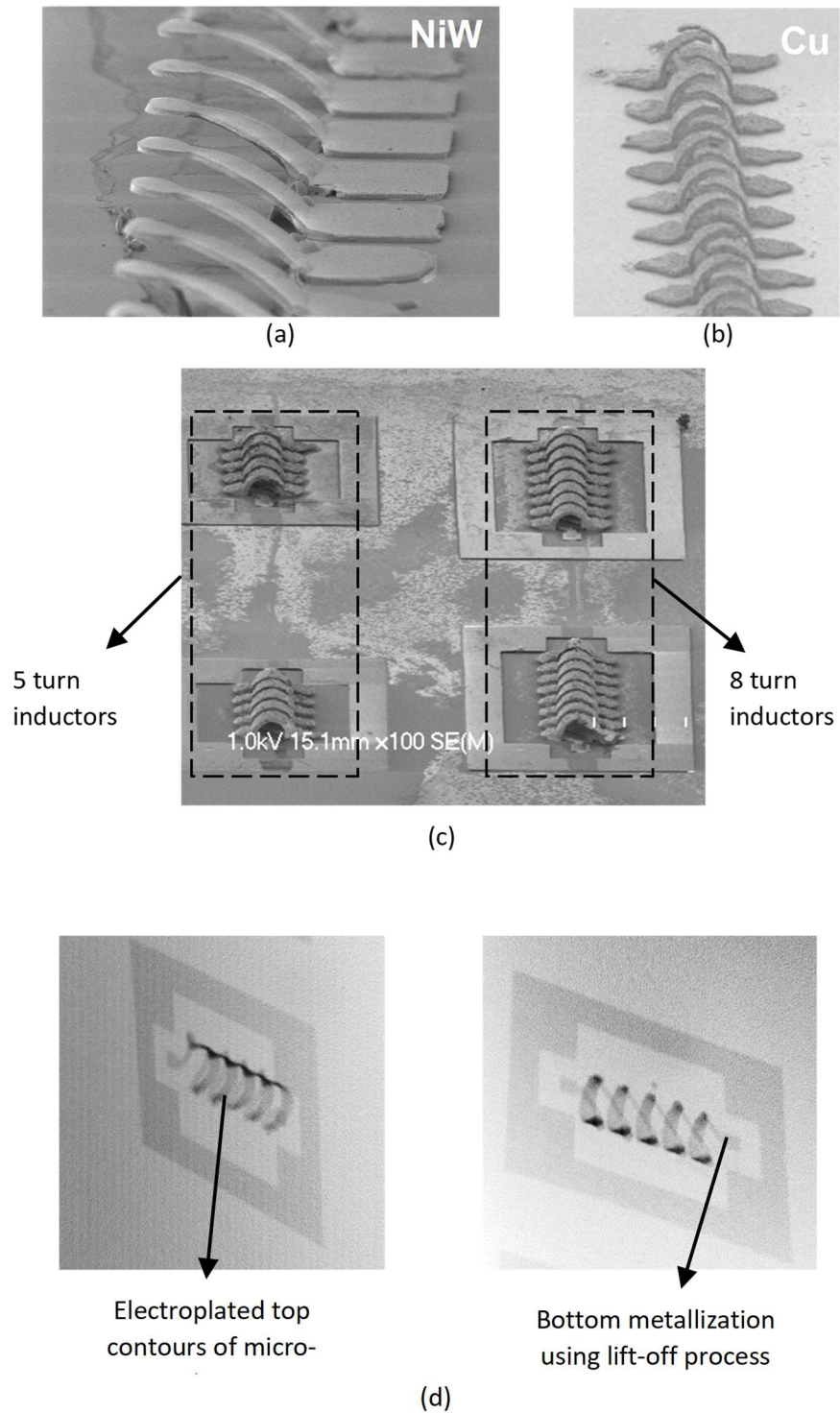


Figure 23 SEM images of fabricated sample showing (a) NiW MFIs, (b) Fine-pitch Cu MFIs, (c) Cu micro-inductors and (d) X-ray images showing bottom and top metallization with good connection

Figure 23 (a) – (c) show SEM images of the fabricated sample with Cu micro-inductors and fine-pitch MFIs and NiW coarse-pitch MFIs. X-ray images of the fabricated 5-turn micro-inductor, shown in Figure 23 (d) show good connection between the top and bottom metallization. SEM images in Figure 24 show the height difference between the MFIs and

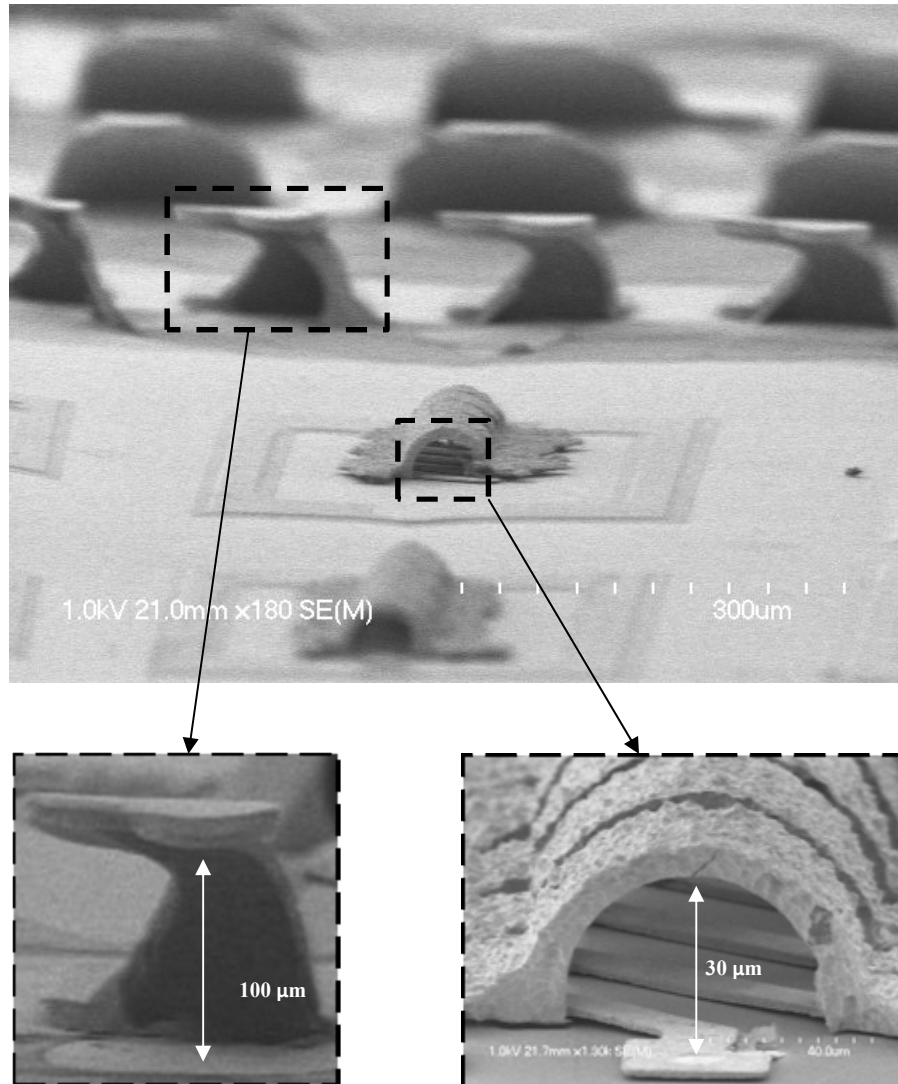
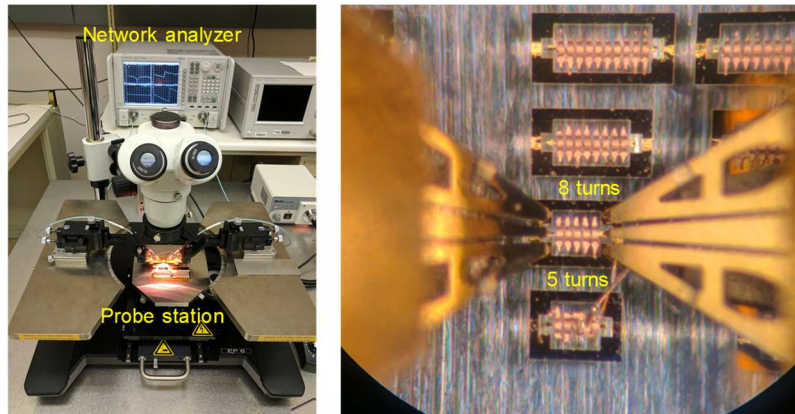


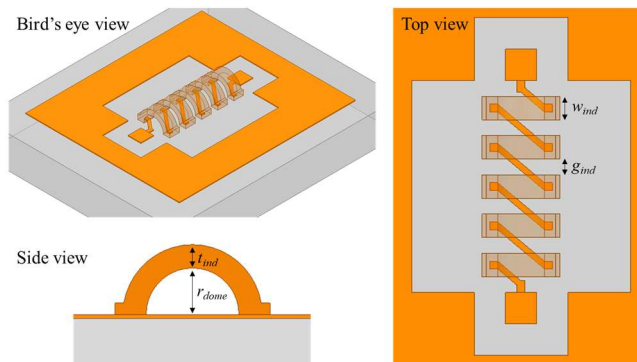
Figure 24 SEM images of the samples depicting height differential – the height differential between the co-fabricated MFIs and the micro-inductors allow the inductors to be embedded between tiers in a stack while the MFIs provide the required interconnection and compensate any surface non-planarity

the micro-inductors fabricated on the same substrate. The height differential allows heterogeneous integration with micro-inductors embedded between substrate tiers while MFIs provide the required electrical interconnections.

3.2 Electrical and Mechanical Measurements



(a)



(b)

Figure 25 Measurement setup: A Cascade microprobe station and Keysight network analyzer and optical image of micro-inductors with GSG probes. (b) Simulation configuration for inductors using ANSYS HFSS software; t_{ind} , w_{ind} , and g_{ind} refer to the thickness, width, and gap of solenoid inductors, respectively, and r_{dome} refers to the radius of a sacrificial photoresist dome.

This section presents electrical and mechanical measurements of the fabricated micro-inductors. The radio-frequency (RF) measurements of micro-inductors were performed to extract their inductance and Q-factors. The fabricated micro-inductors are measured using a Cascade microprobe station and Keysight PNA X N5245 network analyzer. Prior to the measurements, short-open-load-through (SOLT) calibration was performed up to 40 GHz using a calibration substrate. After calibration, ground-signal-ground (GSG) probes of a 200 μm pitch were used for 2-port measurements, as shown in Figure 25 (a). Each micro-inductor is surrounded by a ground plane to facilitate probing. Figure 25 (b) illustrates simulation configurations for solenoid micro-inductors using full-wave electromagnetic software (ANSYS HFSS, Version 18.1).

Figure 26 illustrates the measured and simulated S-parameters for the fabricated 5-turn micro-inductor; the figure shows a good match between the simulated and the measured structure. After S-parameter to Z-parameter conversion, the resistance, inductance, and Q-factor of each inductor can be extracted using (5) – (8) [104], where Re and Im stand for real and imaginary parts, respectively, and ω is the angular frequency.

$$Z_{diff} = Z_{11} + Z_{22} - Z_{12} - Z_{21} \quad (5)$$

$$R = \text{Re}(Z_{diff}) \quad (6)$$

$$L = \text{Im}(Z_{diff})/\omega \quad (7)$$

$$Q = \text{Im}(Z_{diff})/\text{Re}(Z_{diff}) \quad (8)$$

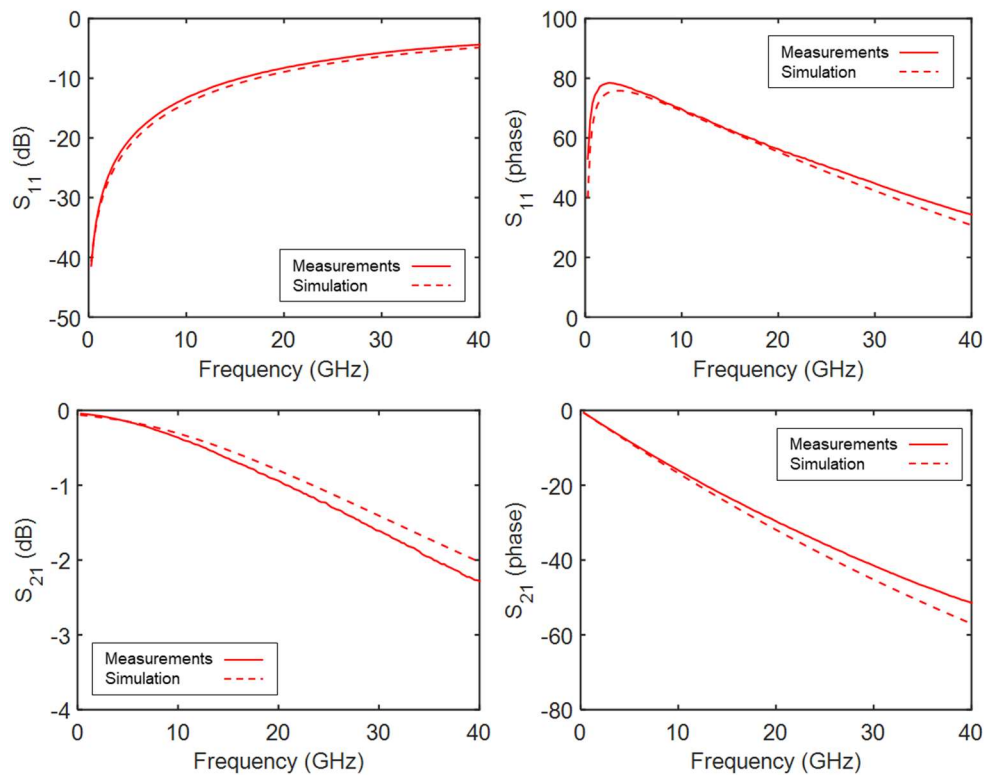
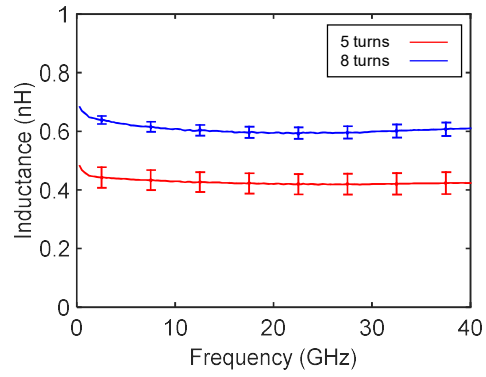


Figure 26 Measured and simulated S-parameters for the 5-turn inductor; results show close match between the simulated and measured values

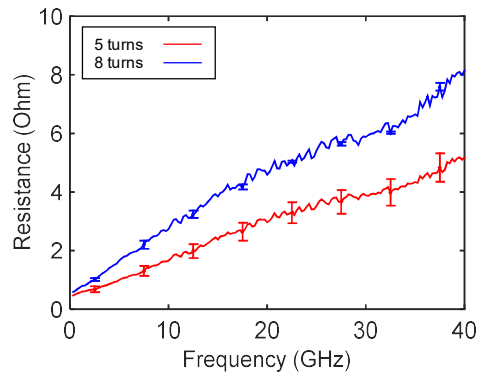
Figure 27 shows the extracted inductance, resistance, and Q-factor for the 5- and 8-turn micro-inductors from the RF measurements. For each structure, five measurement results were averaged with the error bars of one standard deviation. As the number of turn increases, inductance values increase while Q-factors decrease. The maximum Q-factor of ~ 25 is achieved at 33 GHz for the 30 μm radius and 10 μm thick 5-turn micro-inductor.

Table 4 Performance Comparison of the Fabricated Inductors with Published Workshows the performance comparison of the fabricated inductor with some of the published work for 3D solenoid shaped inductors. The fabricated micro-inductors, which demonstrate

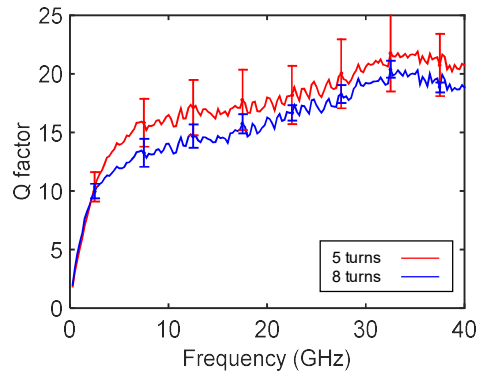
proof-of-concept, exhibit a Q greater than 15 for a frequency band of over 35 GHz with a



(a)



(b)



(c)

Figure 27 Measured (a) inductance, (b) resistance and (c) Q-factor of the 5 and 8 turn micro-inductors

SRF of > 40 GHz and an inductance of 0.45 nH; the fabricated micro-inductors were not optimized. The fabrication process uniquely allows co-fabrication of I/Os with the micro-inductors; this significantly reduces the number of fabrication steps and increases the ease and flexibility of heterogeneous integration.

Table 4 Performance Comparison of the Fabricated Inductors with Published Work

Reference	Peak Q @ (f_{qmax})	Frequency Band with Q > 15 (GHz)	L (nH)	SRF (GHz)	Substrate	Inductor shape	Co-fabrication with I/Os
[99]	100 (3.2 GHz)	< 8	3.5	n/r	Glass	3D solenoid	No
[106]	17.5 (70 MHz)	< 0.1	60	n/r	Silicon	3D toroidal	No
[107]	46 (400 MHz)	n/r	38	n/r	Glass	3D solenoid	No
[108]	50 (6 GHz)	< 7	2.3	> 20	Silicon	3D solenoid	No
[109]	32 (0.95 GHz)	< 0.5	1000	1.24	Polymer	3D solenoid	No
This Work	25 (33 GHz)	> 35	0.45	> 40	Glass	3D solenoid	Yes

The effect of coil radius (r_{dome}) on the Q-factor was also studied using the simulation configuration described above. The maximum Q-factor shows an increase with the increase in the coil radius; this is primarily due to lower flux leakage and reduced parasitic capacitance between the base metallization and the electroplated contours of the micro-inductors [105]. The inductance also increases with an increase in coil radius due to a larger core area. The simulated results for this trade-off are depicted in Figure 28.

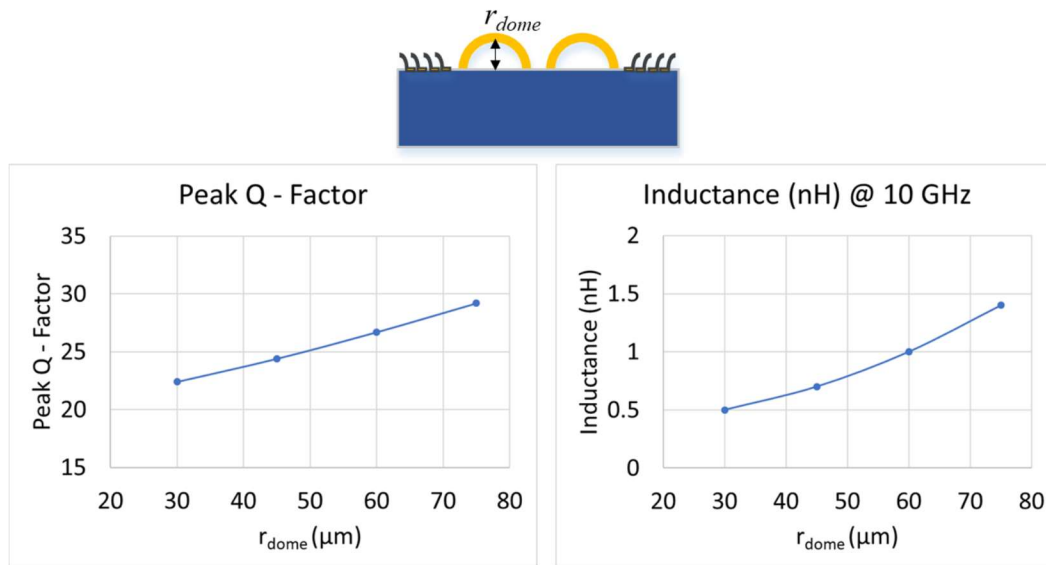


Figure 28 Trade-off between dome radius and the micro-inductor's peak Q-factor and inductance

The developed co-fabrication process also gives control over the type of material and thickness of the electroplated layer. This allows modulation of mechanical properties of the MFIs (compliance, elastic range, etc.) to better meet the varying requirements of electronic systems. For example, the total ‘clamping’ force required to maintain a good electrical connection would be a function of the number of I/Os and the compliance of the I/Os. Thus, modulating the compliance can allow for achieving the desired clamping force for a given number of I/Os. Figure 29 shows the mechanical indentation results for the fabricated MFIs. Indentation was performed using a Hysitron Triboindenter with a cono-spherical probe tip. The measured compliance of the fine-pitch Cu MFIs with a thickness of 9 μm was 1.1 mm/N while that of the 7 μm and 10 μm thick large coarse-pitch NiW MFIs was 10 and 2.6 mm/N, respectively. The hysteresis depicted by the loading-unloading

curve here is due to the plastic deformation caused by exceeding the yield strength. The indentation of the MFIs also induces work hardening of the structure and introduces defects into the metal, causing an increase in the yield strength for subsequent indentations [110]. Further details on the optimization and fabrication of the flexible interconnects utilizing the photoresist reflow process can be found in [51], [86], and [100].

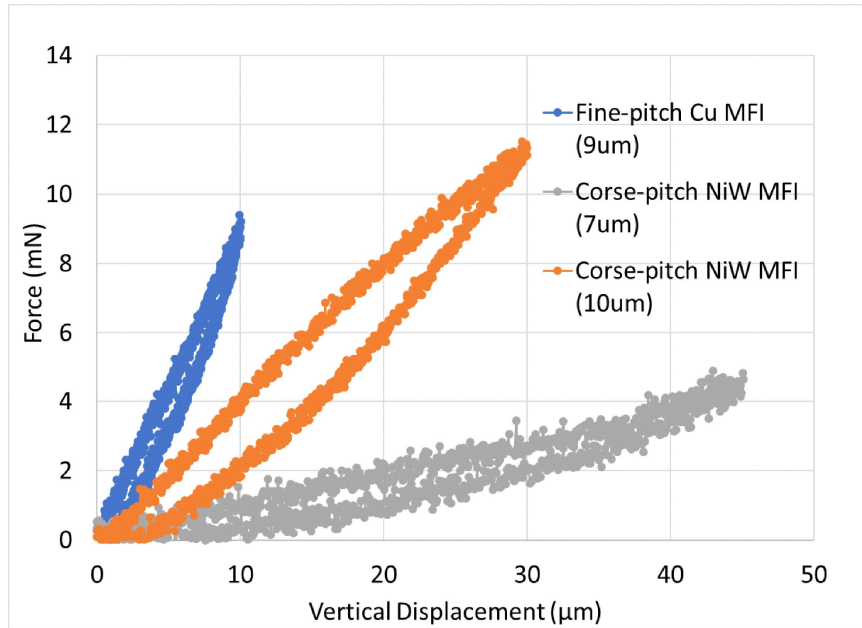


Figure 29 Compliance measurements for the fabricated MFIs

3.3 Conclusion

In this chapter, co-fabrication of 3D solenoidal micro-inductors and MFIs as I/Os is presented. The developed process enables I/Os to be fabricated with different pitches and vertical heights, enabling seamless heterogeneous integration for RF systems. A maximum height difference of 70 μm was achieved between the large MFIs and the micro-inductors. This large height differential between the micro-inductors and the MFIs can enable

embedding of micro-inductors between substrates for 2.5D or 3D integration. Fabrication of micro-inductors on the high-density stitch chip allows leveraging low-loss substrates for high performance passives and low-loss electrical interconnects. The process also gives control over the mechanical characteristics of the fabricated MFIs by allowing multi-material and multi-thickness electroplating processes. Electrical measurements of two different fabricated inductor structures are also presented.

CHAPTER 4. 3D INTEGRATED ELECTRONIC MICROPLATE PLATFORM FOR LOW-COST REPEATABLE BIOSENSING APPLICATIONS

CMOS biosensors are increasingly being utilized for sensing various modalities of cellular and molecular samples including, but not limited to, electrical, magnetic, and optical modalities at low cost. Sensing these modalities involves correlating the cellular-based physiological events to change in current or voltage that can then be sensed using integrated electrodes [111-118]. A change in electrical response can be induced by the administration of a stimulating chemical or biological agent on electro-active samples (cardiac cells, neurons, etc.) and any resulting changes in the sensed signal can then be studied to determine the drug efficacy or pathogen mechanistic effects [116, 118].

These cell-based sensing techniques require the growth of cells onto the biosensor's surface; both the successful adhesion and growth of these cells onto the biosensor are pivotal for meaningful sensing and are strongly affected by the type of material and the surface roughness [119-125]. Growth of human cells on a multi-modality CMOS biosensor has been shown in [126]. However, growing cells directly onto the biosensor is tedious due to the surface treatments required to enhance bio-compatibility and culture cells. Additionally, culturing cells directly onto the CMOS biosensor may be expensive because it is difficult to re-use as it must undergo a rigorous cleansing process or disposed of to avoid contamination [116]. Moreover, even after cleaning and sterilizing the CMOS biosensor surface, the biosensor might not be suitable for re-use if the cell type or the biochemical stimulus to be tested are different. Contamination poses a perpetual risk to the

proper functionality of the CMOS biosensor. Furthermore, any electrical connections to the board (e.g. wire bonds in [126]) and culture medium sealing (e.g. PDMS sealing in [126]) need to be replaced for a new sample during which there is a high likelihood of damaging the CMOS biosensor and/or interconnects. Another major bottleneck in this process is the fact that the biosensor is ‘tied down’ while the cells are growing to full confluence; the biosensor is only actively measuring after successful completion of cell growth and differentiation which can take several weeks resulting in low throughput. To address these challenges, this chapter presents a 3D integrated disposable e-microplate platform allowing the reuse of the CMOS biosensor and thereby reducing cost and increasing throughput relative to systems that are non-disposable. The platform utilizes mechanically-flexible interconnects (MFIs), described in previous chapters, and through-silicon-vias (TSVs) to electrically interface the sensing electrodes on the CMOS biosensor to the sensing electrodes on the e-microplate while maintaining a physical separation of the biosensors from the cellular samples. Mouse embryonic stem cell seeding experiment shows successful cell attachment and growth on the sensing electrodes of the e-microplate. The electrical characterization results show that the integration of the e-microplate does not adversely affect the performance of the underlying CMOS biosensor, as seen via the consistency of the internal amplifier gain and the input referred noise. Additionally, the e-microplate system is shown to perform successful impedance mapping on DPBS solution. The average measured resistance of the TSV-MFI link is 163 m Ω while the measured 3dB bandwidth and the integrated input referred noise with the e-microplate included is 0.5-400 Hz and 4.96 μ V_{rms}, respectively. The low input noise ensures high SNR for sensing minute biological signals from the cellular samples, which is critical for reliable analysis.

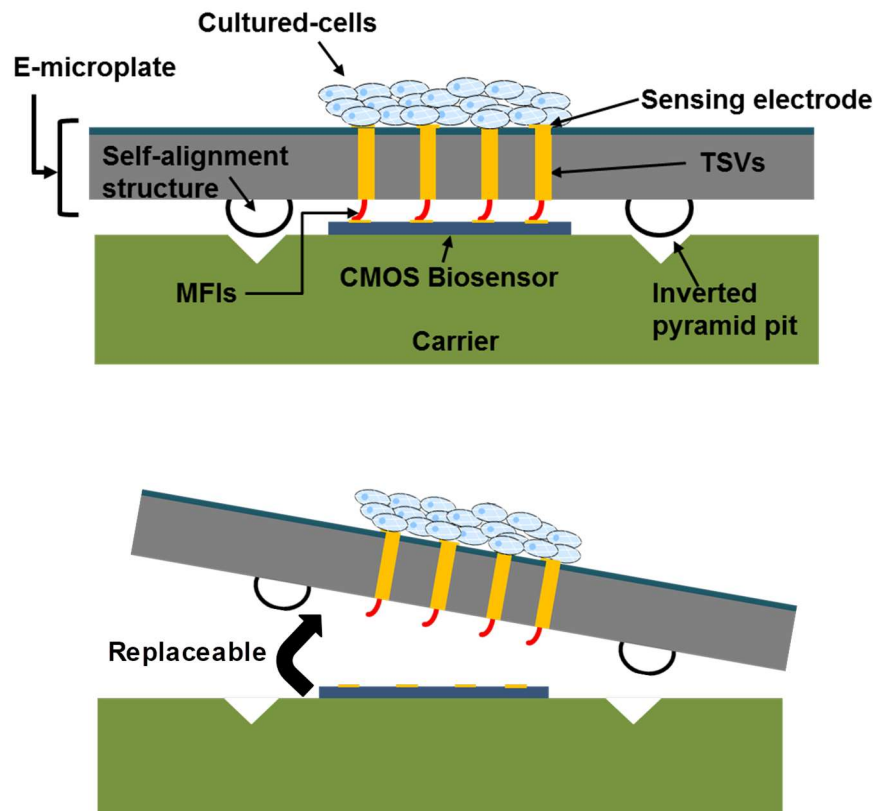


Figure 30 Envisioned micro-fabricated electronic microplate platform – the electronic microplate can be replaced, and the biosensor reused

4.1 System Overview

Figure 30 shows the envisioned e-microplate platform. The e-microplate serves as a 3D integrated disposable tier separating the CMOS biosensor from the cultured cells. Mechanical self-alignment structures and pyramid pits with sub-micron alignment accuracy [127], which have been described earlier in Chapter 2, can be incorporated into this platform to enable low-cost and high-accuracy alignment between the e-microplate and the CMOS biosensor. The gap between the two tiers can be modulated by adjusting the size of the pyramid pits and the self-alignment structures. Electrical interconnections

between the cultured cells and the sensing electrodes on the CMOS biosensor are enabled using through-silicon-vias and mechanically flexible interconnect integration. The flexible interconnects compensate for any surface non-planarity or minor gap variations between tiers while maintaining good electrical connection. After performing required measurements on a cell culture, the e-microplate can be replaced, and the CMOS biosensor and board reused for a new set of measurements. The CMOS biosensor presented in [126] was utilized for the e-microplate assembly.

4.2 Fabrication of E-microplate

Figure 31 shows the fabrication process of the e-microplate. The TSVs are first fabricated using the mesh process. A standard BOSCH process is used for silicon etching followed

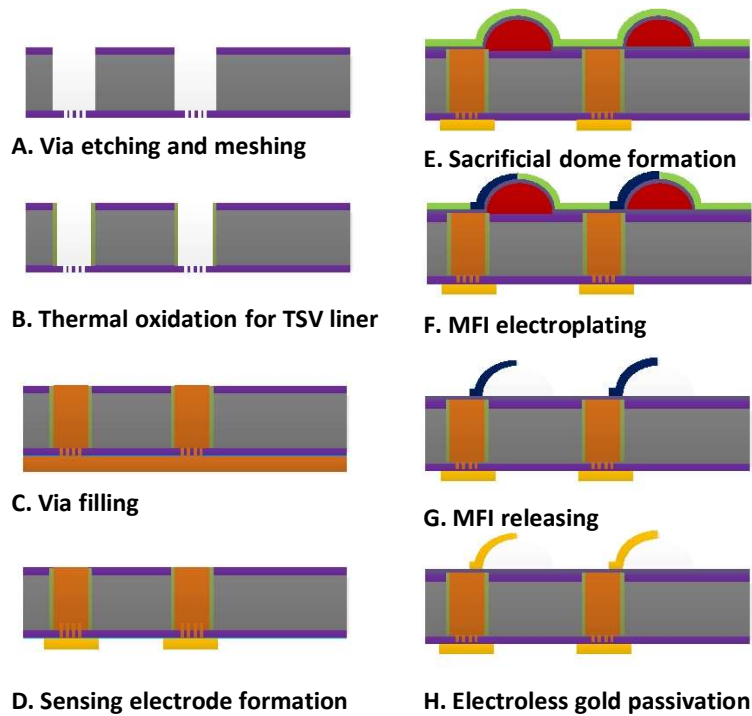


Figure 31 Fabrication flow of the e-microplate

by mesh formation in the oxide layer by photolithography and subsequent oxide etch. The TSVs were then lined with oxide using thermal oxidation in furnace. Seed layer deposition and copper electroplating was then carried out to fill the vias. CMP was then utilized to planarize both sides of the wafer for further processing. The sensing electrodes were fabricated on the top side of the e-microplate by the deposition of Ti/Cu/Au metallization with 30nm/500nm/500nm thickness using an evaporation process, followed by a subsequent lift-off process. After the formation of the sensing electrodes, gold passivated NiW MFIs, using the same process described in Section 2.2.1, were fabricated on the bottom side; utilizing NiW to fabricate the MFIs allows for larger deformation within the elastic region owing to its higher yield strength relative to copper [86]. As low-profile MFIs were required for this particular application, higher spin speeds were utilized to get a final dome height of $\sim 30 \mu\text{m}$. The gold passivation using electroless plating ensures reliable gold-to-gold contact between the MFI and the sensing electrode on the CMOS biosensor. The surface profile of the sensing electrodes for the fabricated e-microplate is shown in Figure 32. Surface variations and dishing are seen owing to the CMP process. Key dimensions of the TSVs and MFIs fabricated for the e-microplate are summarized in Table 5. The layout of the e-microplate pixel group was designed to complement the sensor pixel layout on the CMOS biosensor, as described in [126]. Figure 33 shows an X-ray and an SEM image of the TSV-MFI integration. As seen from the X-ray image, the fabricated TSVs are free of any voids enabling reliable interconnections, which are crucial for the accurate functionality of the platform. The SEM image shows the fabricated MFIs in a

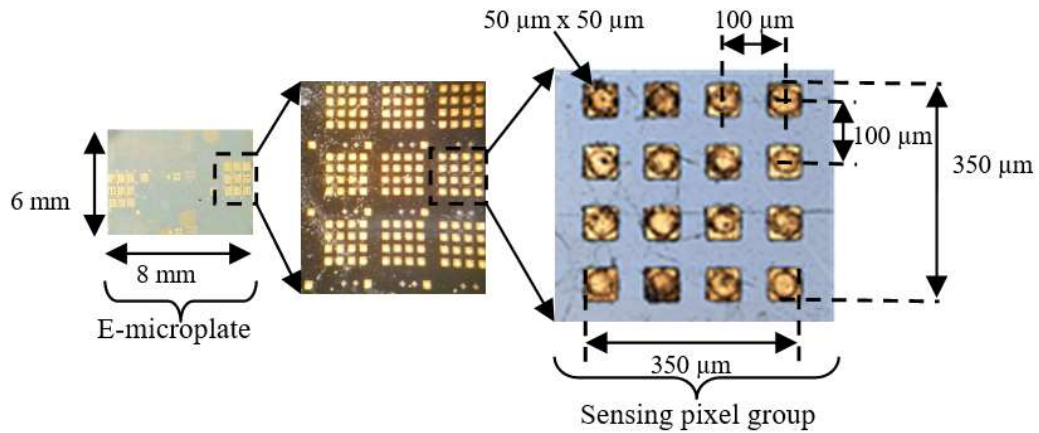


Figure 32 Sensing pixel group of e-microplate and its surface profile

Table 5 Dimensions of the fabricated MFIs and TSVs

	Dimension	Value (μm)
TSVs	Diameter	50
	Height	300
	Pitch	100
MFIs	Thickness	3.5
	Vertical Height	30
	Pitch	100

pixel group on the bottom side of the e-microplate (facing the CMOS biosensor); each pixel

group consists of 16 MFIs, which make a contact with the corresponding electrodes on the

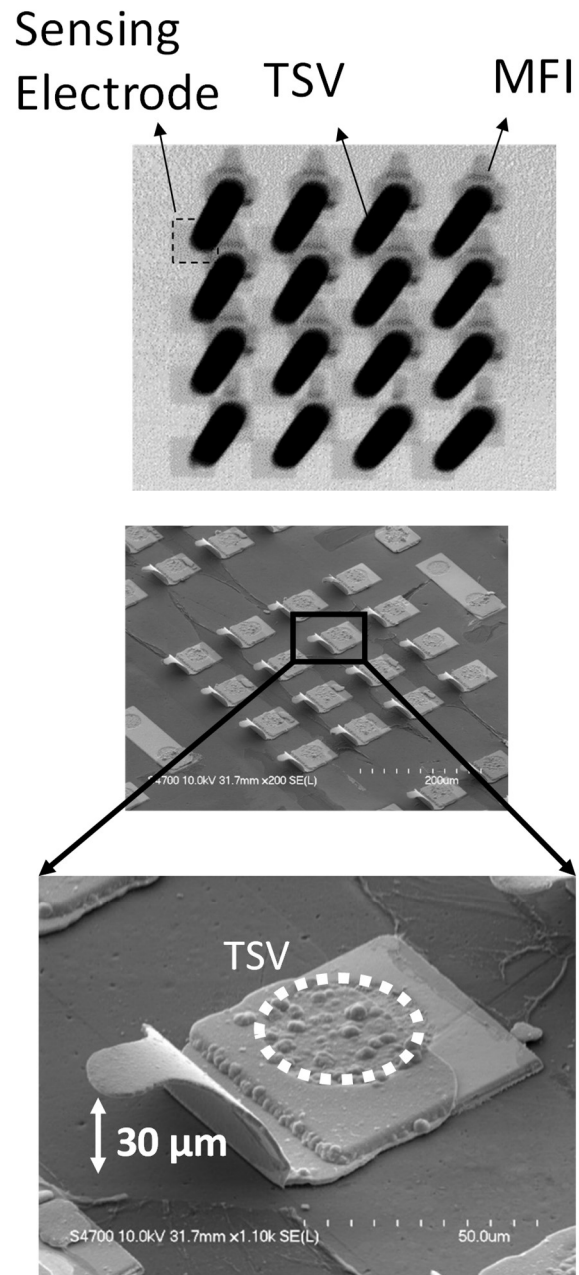


Figure 33 X-ray and SEM images of the fabricated e-microplate pixel group

CMOS biosensor.

4.3 Characterization

4.3.1 Mechanical Characterization of MFIs

Figure 34 shows the mechanical compliance measurements performed for the MFIs on the e-microplate using a nano-indentor. The 30 μm tall MFIs regain original height after up to 10 μm of vertical displacement; this allows them to compensate for minor surface profile or inter-tier gap variations ensuring a good electrical interconnection to the electrodes on the CMOS biosensor. The measured compliance of the fabricated MFIs is $\sim 15 \text{ mm/N}$. The non-linearity in the force-displacement curve occurs when the yield strength is exceeded. The hysteresis in the curves with higher displacement indicates plastic deformation and work hardening, which introduces defects into the structure, increasing the yield strength for subsequent indentations [110].

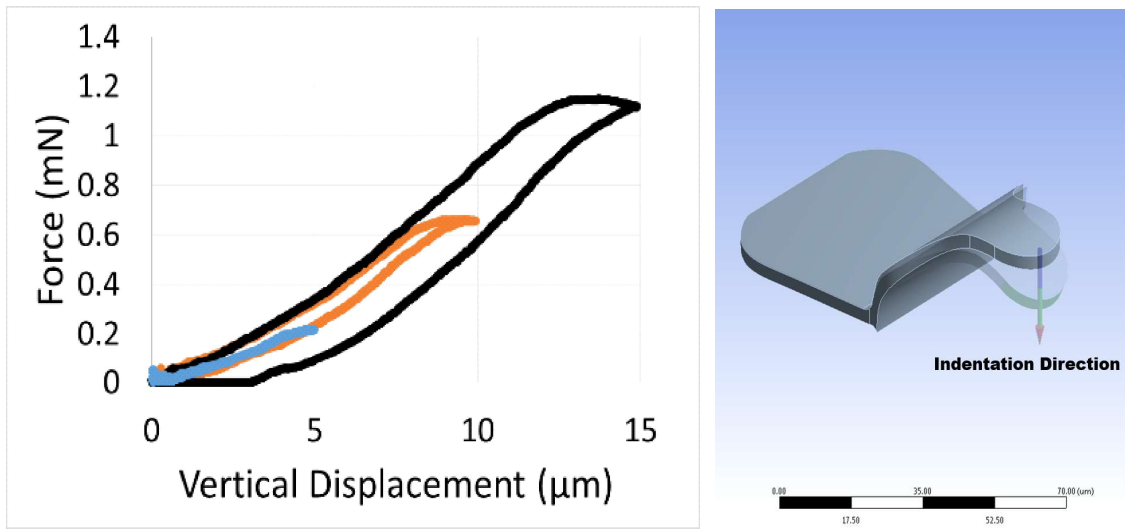


Figure 34 Mechanical compliance measurements for fabricated MFIs

4.3.2 Electrical Characterization of TSV-MFI Link

Four-point resistance measurement for the TSV-MFI link was carried out by bonding e-microplate, as shown in Figure 35. The average resistance measured for the link was 163 m Ω , which included the contact resistance. The low value of resistance, compared to the input impedance of the amplifier (\sim G Ω range) in the CMOS biosensor, ensures negligible signal degradation from the living cells on the sensing electrodes to the biosensor.

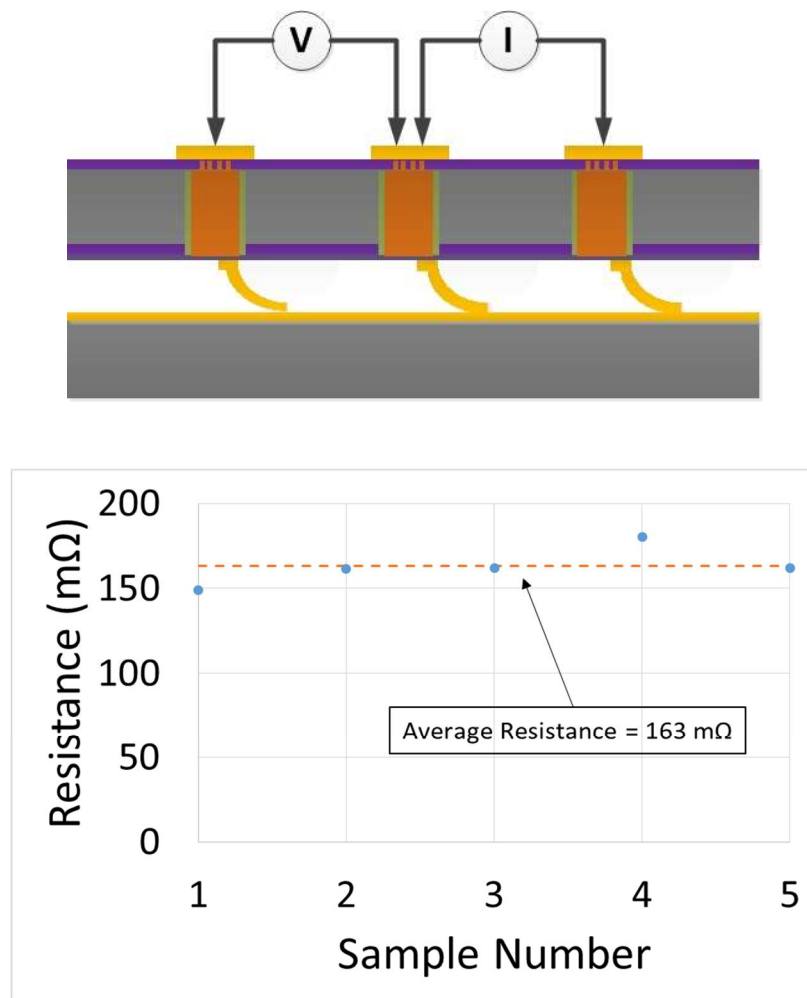


Figure 35 Four-point resistance measurement results for the TSV-MFI link

4.3.3 Cell Growth

Cell growth experiments were carried out to verify the viability of human pluripotent and mouse stem cell growth on the e-microplate's surface. Attachment and growth of human pluripotent stem cells was investigated over various surfaces to investigate adhesion and growth across these surfaces as compared to standard TCPS. Each of the five experimental surfaces (silicon nitride with and without sensing electrodes, silicon oxide with and without sensing electrodes, and silicon oxide with TSVs and sensing electrodes) were sterilized with three washes of ethanol followed by three washes with water. All surfaces were then coated with Matrigel (Corning) for 24 hours at 37°C prior to cell seeding. Human pluripotent stem cells were cultured in serum free media (mTeSR, StemCell Technologies) for several passages prior to seeding experiments. Cells were then dissociated to single cell suspension and seeded onto each of the five silicon surfaces at a concentration of 200,000 cells/cm². As a control, cells were similarly seeded onto tissue culture polystyrene (TCPS), a common material used in standard culture dishes. Cells were cultured for 48 hours prior to fixation and staining with Hoechst nuclear dye. Cell seeding was visualized with an epifluorescent microscope.

Figure 36 shows the initial attachment and growth of cells 48 hours after seeding. Nitride and oxide on silicon, as shown in Figure 36 (a) and (b), respectively, show almost identical results to that of the TCPS control (Figure 36 (f)). For samples with sensing electrodes, the cell attachment appears lower; however, as shown from Figure 36 (c) through (e), after 48 hours, all the sensing electrodes show some cell adhesion and would be expected to grow and cover the entire surface if left for a longer time period. In these initial cells seeding experiments, human pluripotent stem cells were used as a proof of concept. However, these cells can be later differentiated into cardiac cells or neurons, allowing for more complex

studies and integration of the silicon membrane interface for advanced sensing applications including, but not limited to, studying drug effects on cardiac cell beating or neuron activity.

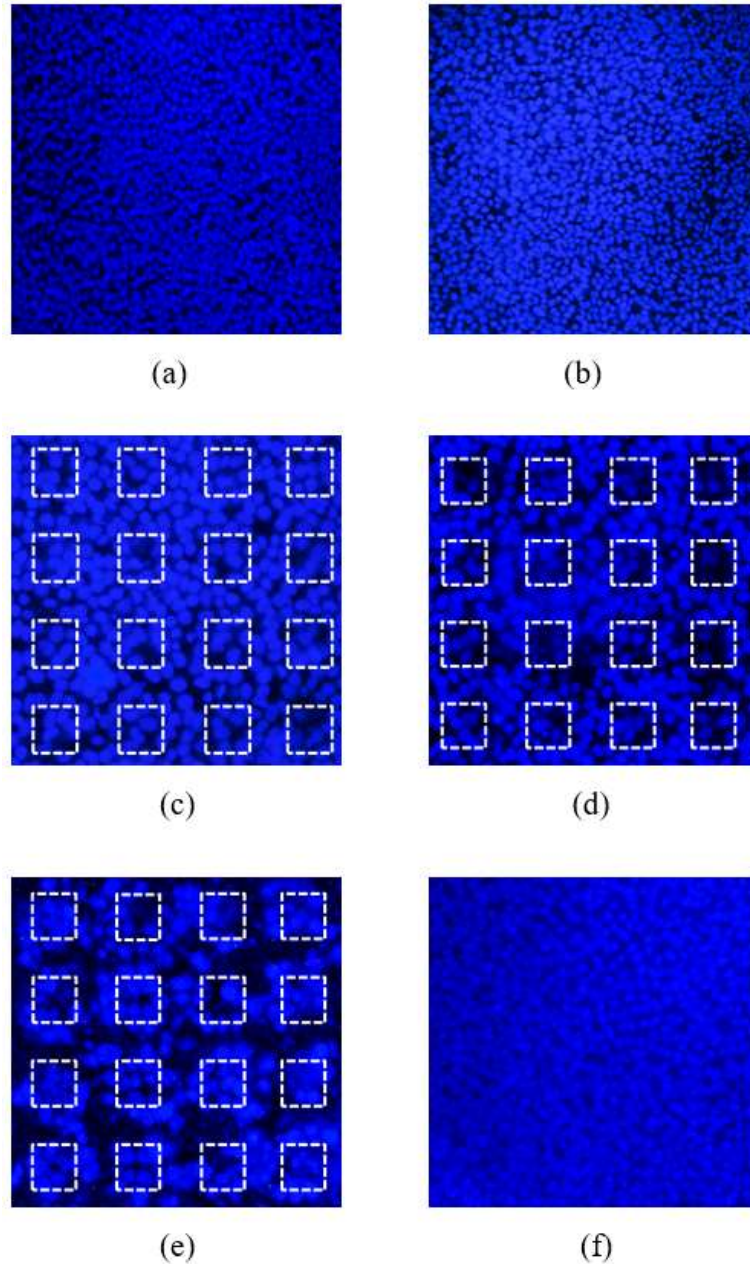
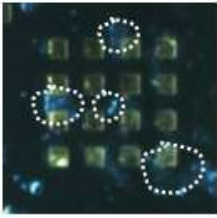
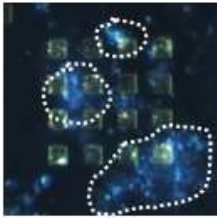
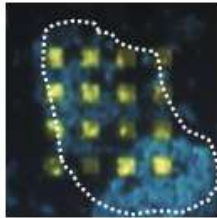
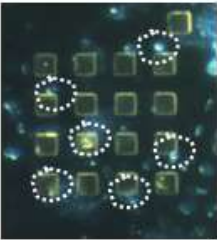
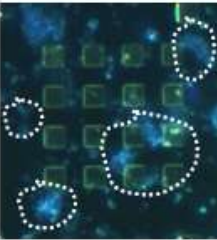
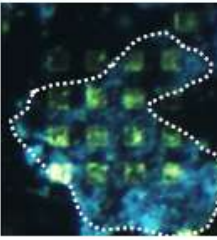


Figure 36 Cell growth results after 48 hours of seeding on (a) nitride, (b) oxide, (c) nitride with sensing electrodes only, (d) oxide with sensing electrodes only, (e) silicon membrane with oxide surface, sensing electrodes, and TSVs and (f) control with cells on TCPS

D3 mouse embryonic stem cells were also tested for attachment and growth over time with the e-microplate. The sensing electrodes' surface was first washed with methanol followed by three washes with phosphate-buffered saline. The surface was then gelatin-coated (0.1% gelatin) to promote cell adhesion. The cells were trypsinized with 0.05% trypsin to form a single-cell suspension and seeded at a density of 70k cells/e-microplate in 400 μ L of media. The media was supplemented with leukemia inhibitory factor (LIF) to maintain cell pluripotency. Thereafter, the media was changed every two days, and cell growth monitored by examination with a stereoscope. The results are shown in Table 6.

Table 6 Mouse embryonic stem cell growth on oxide and nitride surfaces with sensing electrodes

Surface	48 hours	96 hours	144 hours
Oxide			
Nitride			

As seen from Table 6, the mouse stem cells adhere to the sensing electrodes after 48 hours of cell seeding. Subsequent growth is observed after 96 and 144 hours of cell seeding, respectively. After the 144-hour mark, cells are seen to cover the majority of the sensing

electrodes on both surfaces. This further warrants the utilization of e-microplates for cell-based assays of varying types and makes the platform versatile and adaptable.

4.3.4 Integrated System characterization

The system level characterization was carried out by flip-chip bonding the e-microplate to the biosensor. The biosensor was first attached to a carrier chip using photoresist as adhesive. The carrier chip with the biosensor was then placed on the evaluation board by using epoxy. The e-microplate was then flip-chip bonded to the biosensor. The flip-chip bonder's force was kept at 1 N. While holding at this force, epoxy was used to hold the assembly together with the subsequent removal of the force. Wire bonds were then made between the assembly and the evaluation board for subsequent testing. A twofold system level characterization was then performed for the assembled e-microplate system. Firstly, the CMOS biosensor's internal amplifier gain and input referred noise were measured

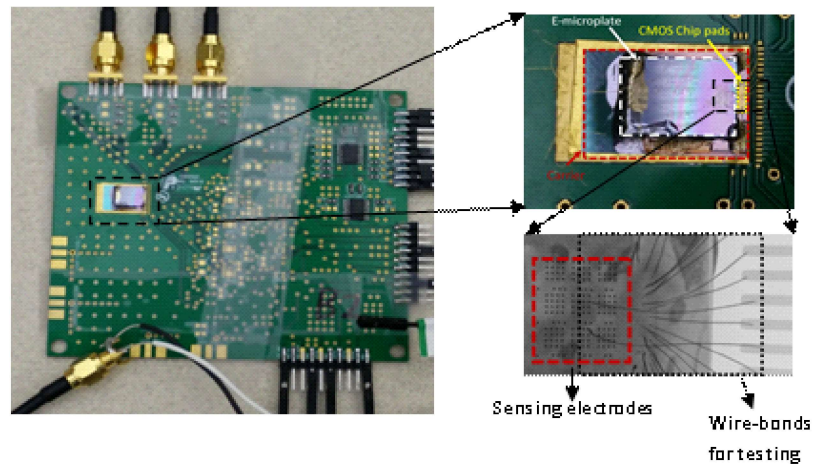


Figure 37 Test setup for gain and noise measurements – sensing electrodes were wire-bonded to test board for measurements



Figure 38 Test setup for impedance mapping

through the wire bonds made to the sensing electrodes on the e-microplate, as shown in Figure 40. The test signal traversed the TSV-MFI interconnection to reach the input of the internal amplifier of the biosensor. Secondly, impedance mapping of DPBS solution was performed in order to verify the functional accuracy of two different assembled systems. Figure 37 shows the assembled e-microplate system used for internal amplifier gain and noise measurements; the system includes the e-microplate, carrier, and CMOS biosensor assembly mounted onto the test board. For impedance mapping, a standard 35 mm petri-dish with a drilled-out bottom was mounted onto the board and sealed using Polydimethylsiloxane (PDMS) to provide electrical isolation while maintaining biocompatibility (Figure 38). Figure 39 shows the X-ray image of a pixel group in the

assembled platform; the MFIs are seen to be well aligned to the sensing electrodes on the CMOS biosensor ensuring good electrical interconnection.

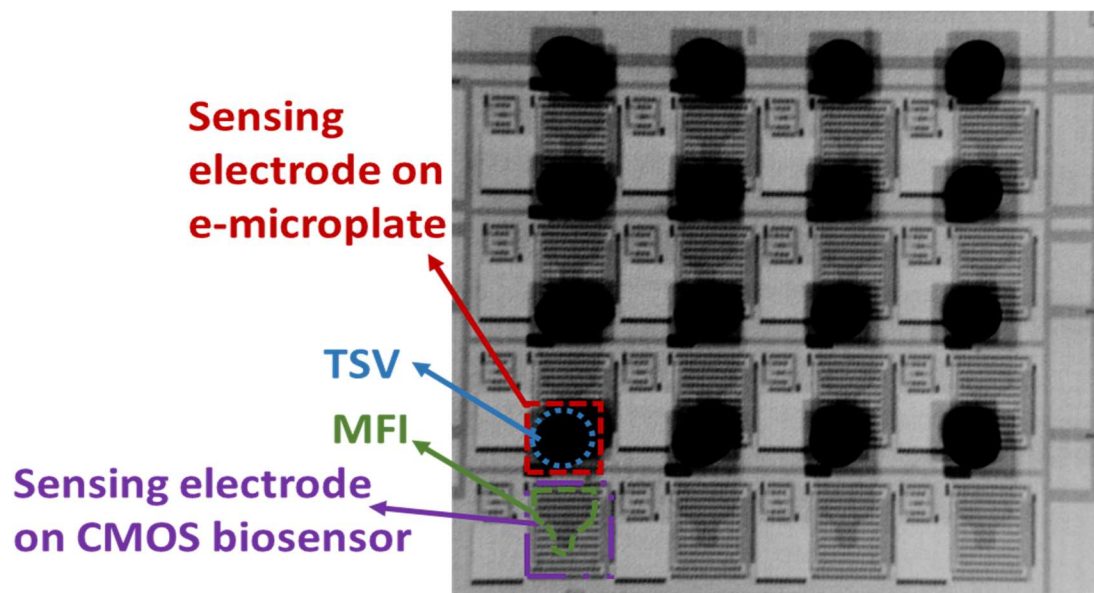


Figure 39 X-ray image showing accurate alignment between e-microplate and CMOS biosensor

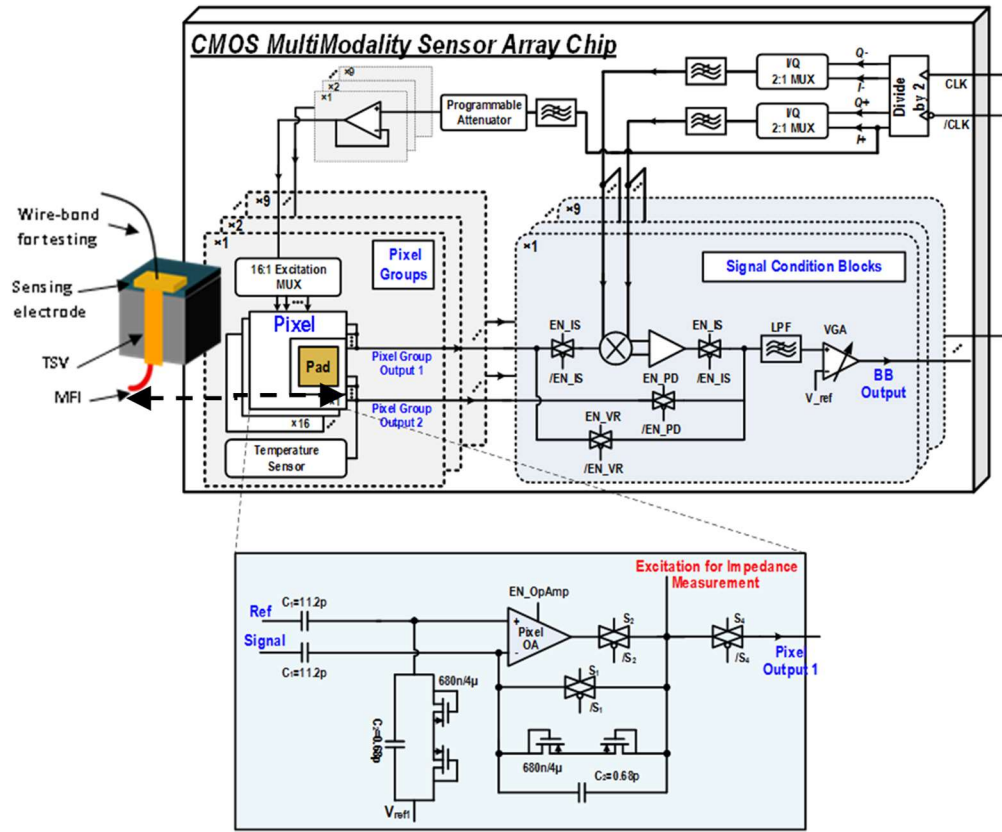
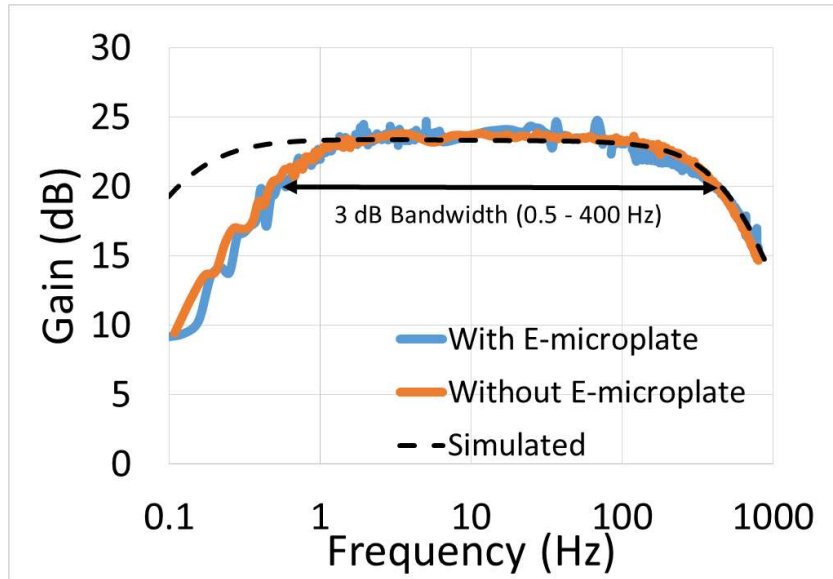


Figure 40 Schematic of internal voltage sensing amplifier and its connection to the e-microplate's pixel

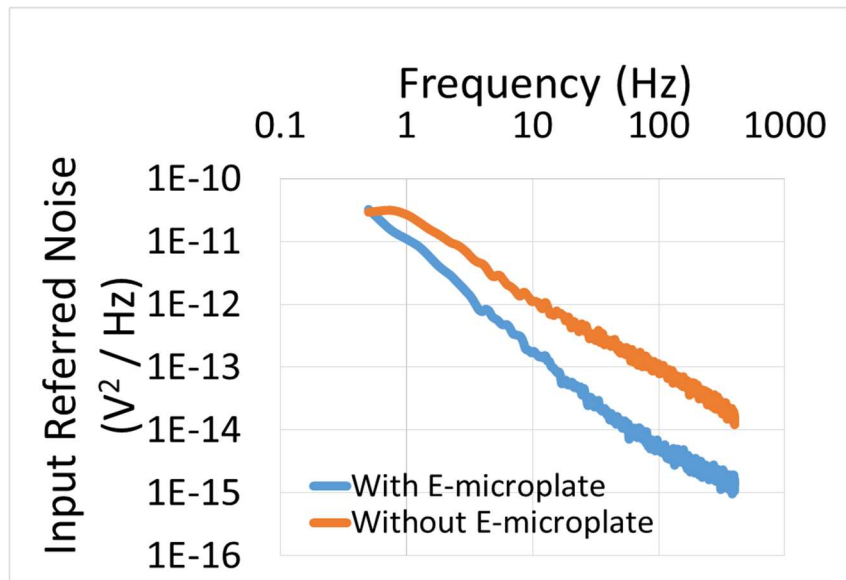
Figure 40 shows the circuit schematic for the in-pixel tri-modality sensor. For the extracellular potential recording, in-pixel op-amp, pseudo resistors, and capacitors C_1 and C_2 are configured as a high-pass inverting amplifier with a voltage gain of C_1/C_2 and a low cut-off frequency of $1/2\pi R_{\text{pseudo}}C_2$. Note that the high cut-off frequency and the voltage gain are fully programmable in signal conditioning block. For the complex impedance measurement, two-pixel electrodes (one for the voltage excitation and the other for the current sensing) are selected through the switch multiplexer and the generated voltage excitation signals bypass the in-pixel op-amp by enabling the transmission gate switch S_1 and is ac-coupled to the voltage excitation electrode. The op-amp in the voltage excitation

pixel is switched off during the voltage excitation. The resulting current flows through the capacitors C_1 and C_2 in the selected current sensing pixel and is converted to the voltage at the output of the amplifier. This voltage signal passes the mixer, programmable low-pass filter, and programmable gain amplifier to complete the complex impedance measurement. The quadrature signals are sequentially applied to the mixer for complex impedance measurement.

To test the effect of the e-microplate on the internal amplifier gain and input referred noise, interconnections were made by wire-bonding the sensing electrodes on the e-microplate to the test board; this allowed the test signals to traverse through the TSV-MFI link to the sensing electrode on the CMOS biosensor. Figure 41 (a) shows the amplifier gain, measured with and without the e-microplate. The results show that the incorporation of the e-microplate does not affect the amplifier gain; also, the 3dB bandwidth remains unchanged. Similarly, the input referred noise, shown in Figure 41 (b), does not degrade with the incorporation of the e-microplate; the integrated input referred noise of the amplifier, from 0.5 Hz to 400 Hz, was measured to be $4.96 \mu\text{Vrms}$. As frequency of most of the biological signals being recorded falls within the 3dB bandwidth, maximum amplification of the minute signals is ensured while simultaneously suppressing the unwanted noise outside this frequency band. This low input noise ensures high SNR when measuring extremely weak biological signals from living cells (e.g. cardiac cells or neurons), which is critical in ensuring the integrity of the measured data. Impedance mapping, using similar techniques as described in [126], was performed for DPBS for two different e-microplates and compared to air to verify the capability and functional accuracy



(a)



(b)

Figure 41 (a) Amplifier gain measurements – the amplifier gain remains unchanged with the incorporation of the e-microplate, (b) Input referred noise measurements – low input referred noise ensures high SNR when measuring weak signals

of the impedance mapping in the e-microplate assembly. The results utilizing the high yield

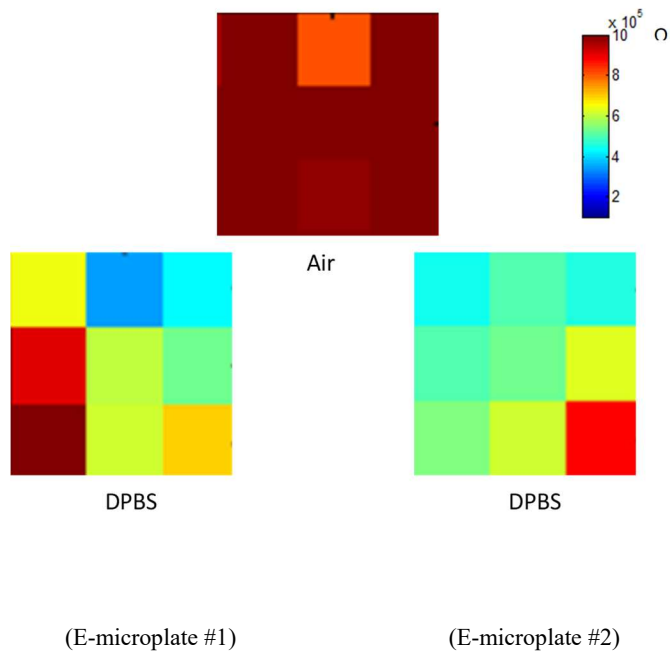


Figure 42 Impedance measurement for air and DPBS measured via e-microplate's pixel group – measurements verify functional accuracy of the platform

pixels in the e-microplate, shown in Figure 42, confirm accurate assembly functionality for 2 different e-microplate assemblies.

4.4 Conclusion

A low-cost, disposable platform using 3D IC technology, capable of providing electrical interconnections between living cells and CMOS biosensors, is presented. The e-microplate sits atop the CMOS biosensor circumventing the need for direct cell growth on the CMOS biosensor surface while the TSV-MFI link provides the necessary electrical interconnections from the cells to the biosensor. The void free TSVs and the gold

passivated NiW MFIs ensure reliable connections to the pixel array on the biosensor, which are essential for accurate sensing. Mouse embryonic stem cells are shown to attach and grow on the sensing electrodes of the e-microplate warranting it suitable for cell-based assays. The integration of the e-microplate does not degrade the CMOS biosensor's amplifier gain or input referred noise, hence ensuring accurate sensing of weak biological signals from living cells cultured on the e-microplate, which is critical for reliable data analysis. Impedance maps generated for air and DPBS confirm functional accuracy of the developed platform.

CHAPTER 5. FABRICATION AND CHARACTERIZATION OF HIGH DENSITY ELECTRODES ON FLEXIBLE SUBSTRATE FOR IN VIVO EMG RECORDING

5.1 Introduction

Recent advances in data analysis methods in neuroscience are shedding light on how a nervous system controls complex behaviors such as vocal learning and song production in songbirds [69, 70]. This research focuses largely on the central nervous system, exploiting new technologies that can record large numbers of individual neurons (brain cells) for extended periods of time in order to quantify their relation to behavior [128-130]. Despite recent evidence pointing to the importance of precise timing in the activity of motor units (the collection of muscle fibers innervated by a single motor neuron) for controlling behavior [24, 71], techniques for recording electromyographic (EMG) signals from muscles lag far behind those developed for neural recordings in the central nervous system. Specifically, most EMG datasets are collected by inserting fine-wire electrodes into the muscles. This method has a number of drawbacks. First, the penetrating wire electrodes damage the muscles into which they are inserted and cannot be used to record the very small muscles that control skilled behavior. Second, wire electrodes typically cannot isolate electrical signals from individual motor units, instead yielding signals that represent the summed activity of many units, preventing analysis of single-unit activity (a standard approach for studying the function of neurons in the brain). New approaches are therefore needed to record stable single-unit EMG activity.

Information-theoretic analyses provide a quantitative framework in which to understand how time series of electrical events (action potentials or “spikes”) in biological tissues represent information and control behavior [24,71,131-133]. For example, in a recent study, EMG signals from expiratory muscles in songbirds (Figure 43 (a)) were recorded using multi-electrode arrays (MEA) [24]. Spike sorting routines [134, 135] were used to identify spikes (tick marks in Figure 43 (b)) from individual motor units, which arise when a motor neuron activates a set of muscle fibers and causes them to contract [136]. Information-theoretic techniques were used to compare the timing of spikes to fluctuations

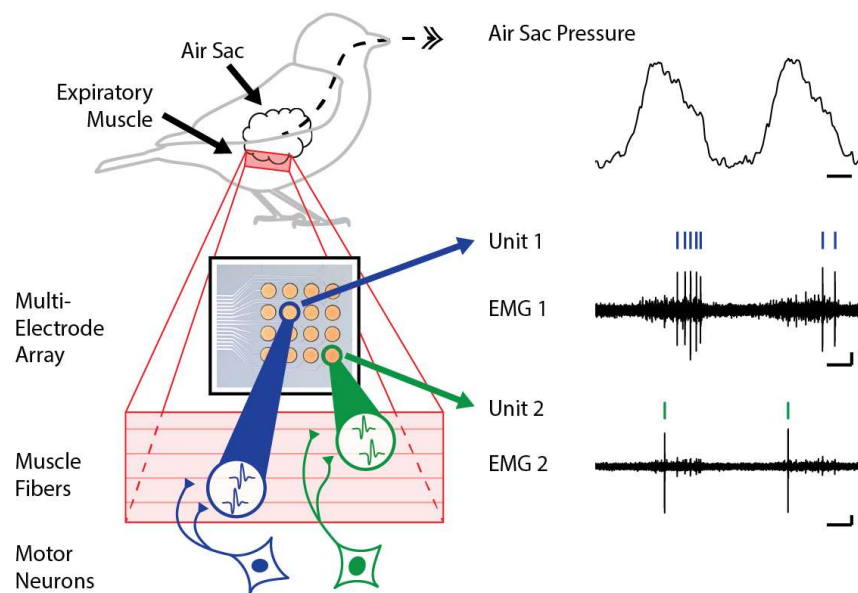


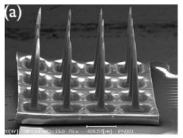
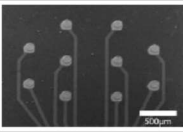
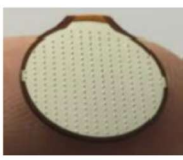
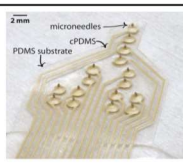
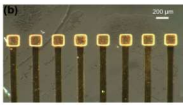
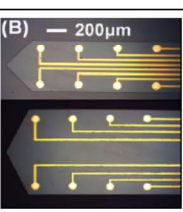

Figure 43 Schematic of experimental set up and EMG activity recorded during breathing. A) The exhaling phase of breathing in songbirds is controlled by expiratory muscles that contract around an air sac. Motor neurons excite individual muscle fibers that cause the expiratory muscle to contract. Multi-electrode arrays are used to record electromyography (EMG) activity. B) Increases in air pressure occur when the expiratory muscles contract. Spike sorting algorithms are used to detect individual spikes (Unit 1, Unit 2) from recorded muscle activity (EMG 1, EMG 2). Tick marks above physiological traces indicate spike times. Time scale: 100 ms. Vertical scale: 30 μ V.

in air pressure of an animal's air sac used for breathing and singing (Figure 43(b)). Although this study provided evidence for the importance of precise spike timing in individual motor units for controlling respiratory behavior [24], the difficulty of robustly recording multiple units simultaneously and over long periods limit our understanding of how the nervous system controls complex behaviors.

The main challenge in characterizing single motor unit activity is obtaining stable, reliable EMG recordings in data sets that are large enough to perform advanced computational analyses (including, but not limited to, information-theoretic methods) [73, 74]. While advances in spike sorting algorithms [79, 137, 138] have helped to better discriminate multiple units recorded on the same channel, the ability to record single units on an MEA channel will improve the reliability of experimental analyses.

Current technologies employ flexible polymers, such as polyimide, PDMS, and parylene-C [148-151], as the substrate for the MEA and use metals like gold for contact sites. MEA fabrication is also beginning to combine materials in order to optimize the processing parameters and mechanical properties of different polymers [139-141]. The advantage to using these materials includes their compliance with muscle and other tissues as well as their biocompatibility. A summary of some of the flexible electrodes from literature is shown in Table 7. However, each of these materials have their own processing challenges: PDMS suffers from poor metal adhesion [142-144]; and, polyimide typically requires a metal etch mask [145, 146] or, in the case of photo-definable polyimide, is significantly more expensive. In this chapter, a hybrid polyimide-PDMS MEA fabrication process leveraging the benefits of each of the materials while mitigating their shortcomings is discussed. Using a hybrid polyimide-PDMS substrate resulted in EMG recordings that

Table 7 Summary of the different types of flexible electrodes in literature

Reference	Flexible Substrate Material	Contact Type	# of Routing Layers / Pitch / Total Electrodes	Application	Measurement Species	Image
[139]	Silicon/ Parylene	3D – needle shaped	Single / 550 μm / 16	Neural	Dog	
[140]	PDMS/ Parylene	3D – convex shaped	Single / NR / 10	ECoG	Rat	
[148]	Polyimide	3D – stacked double-microdomes	Single / NR / NR	ECG	Human	
[149]	PDMS	3D – microneedle shaped	Single / NR / 16	EMG	Cat	
[150]	PDMS	2D	Single / 300 μm / 8	Neural	Rat	
[151]	Parylene	2D	Single / 500 and 1000 μm / 8	EMG	Larvae	
[152]	Parylene	2D	Single / NR / 27	EMG	Rat	
[153]	Parylene	2D	Single / 750 μm / 16	ECoG	Rat	
[154]	Polyimide	2D	Single / 1800 μm / 202	ECoG	Monkey	

were better than those obtained using a pair of fine-wire electrodes inserted into muscle.

Furthermore, our hybrid fabrication process utilizing polyimide as the base layer and PDMS as the top insulation layer allows for ease of fabrication, lower processing time and a lower cost for the MEAs. Moreover, specific shape of the flexible MEAs are designed to record from the mouse fore-limb allowing high-fidelity recordings. The fabrication process flow for the MEAs' fabrication is outlined in Figure 44.

5.2 Flexible MEA Fabrication

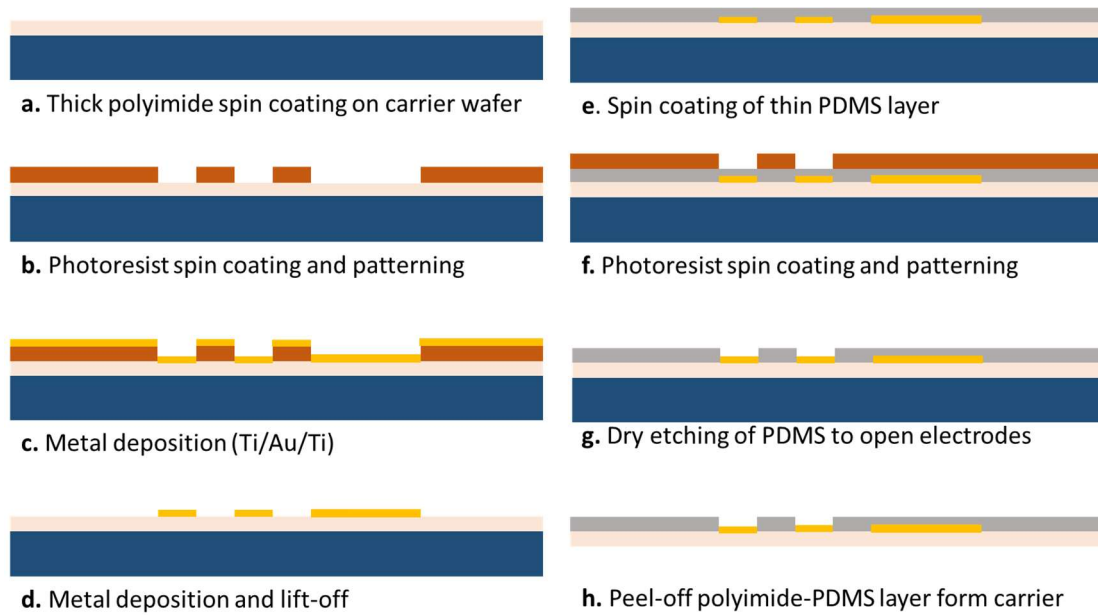


Figure 44 Fabrication process flow for Flexible MEAs.

The first step of the fabrication involves spin coating polyimide (PI-2611 from HD Microsystems) @ 450 rpm on a carrier wafer to get a thick polyimide film. The polyimide is then cured with a temperature profile summarized in Table 8. Photoresist is then spin coated and patterned followed by metallization and a lift-off process. A Ti/Au/Ti layer of 30nm / 200nm / 30nm is deposited using an evaporation process. The bottom Ti layer acts as an adhesion promoter while the top Ti layer provides an easy visual check to confirm

the completion of the PDMS etch process. After the lift-off process, PDMS (Slygard 184, 1:10 ratio) is then spin coated @ 5000 rpm and cured at 100 °C for 2 hours to form the top layer of insulation. In order to promote the adhesion of the resist to the PDMS for further lithography, the PDMS is first exposed to O₂ plasma [147] followed by spin coating of the etch mold. A RIE process is then used to etch the PDMS to expose the electrodes. SF₆ and O₂ were used as the etching gases with a flow rate of 90 and 6 sccm respectively while the

Table 8 Temperature profile used for curing polyimide

Temperature (°C)	Ramp (°C/min)	Duration (min)
100	2	30
150	4	45
200	4	60

RF power was 300 watts. The etch rate obtained for the PDMS was ~ 170 nm/ min.

Two different designs for the MEAs were fabricated for *in vivo* recording from songbird and mouse respectively. The MEA for recording from the songbird consisted of 16 electrodes with equal spacing in both x and y directions. The MEA for recording from mouse fore-limb consisted of four 2x2 electrodes spatially separated to record from different sections of the fore-limb. Optical microscope images of the fabricated devices for

the songbird and the mouse arrays are shown in Figure 45 and Figure 46, respectively. The diameters of the fabricated electrodes fabricated for the songbird are 200, 125 and 50 μm with a center-to-center pitch of 300, 200 and 100 μm , respectively. For the mouse-shoulder array, the 125 μm diameter electrodes with a 200 μm pitch were utilized. As seen in the figure, the gold electrode color is visible in locations where PDMS was etched away while the traces still covered by PDMS appear as a greyish-silver color from the top Ti layer.

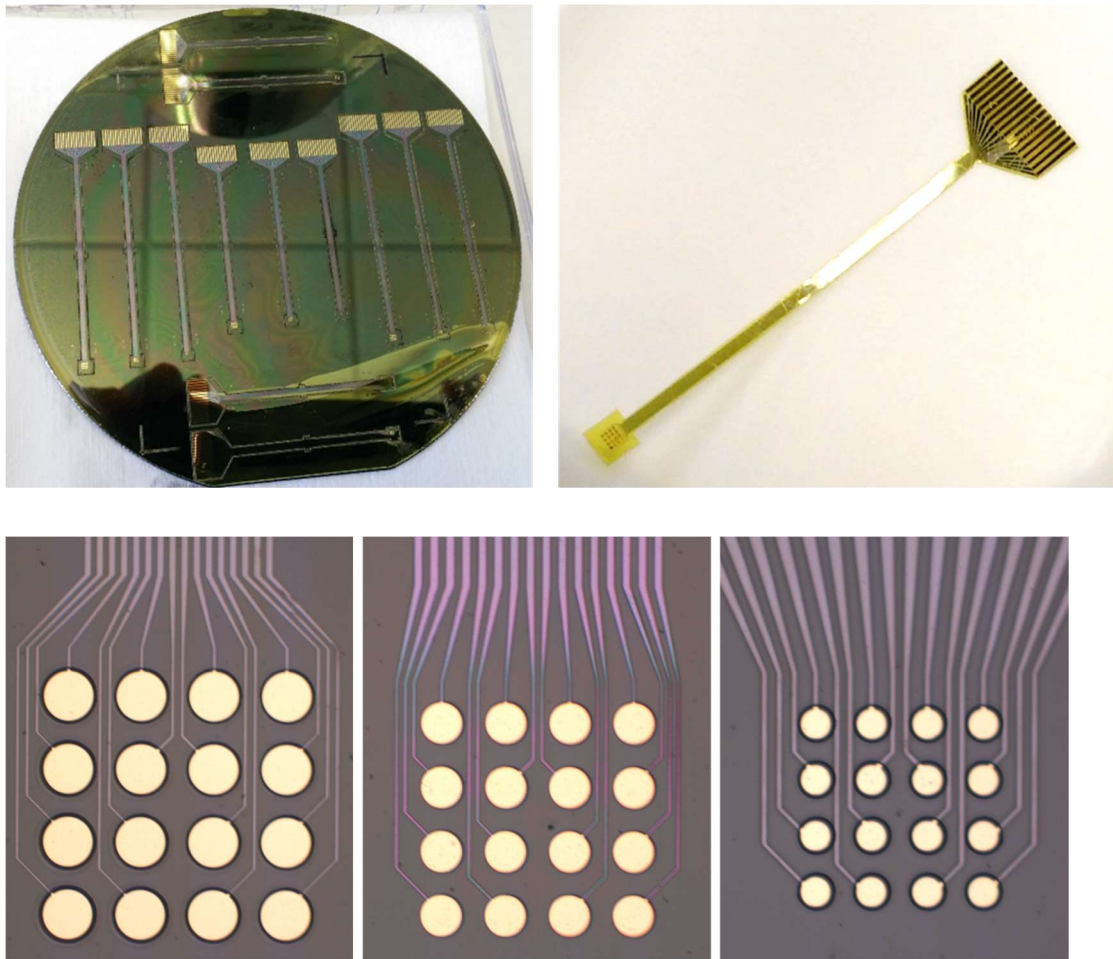


Figure 45 Optical image showing the fabricated electrodes for Songbird's expiratory muscle; (a) 200 μm diameter, 300 μm pitch, (b) 125 μm diameter, 200 μm pitch and (c) 50 μm diameter, 100 μm pitch.

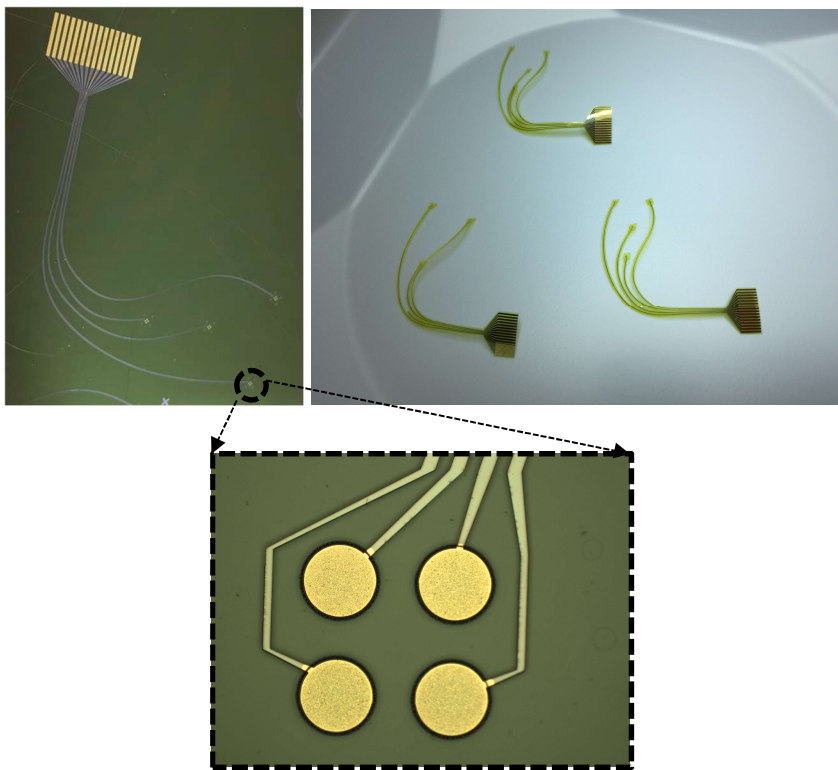
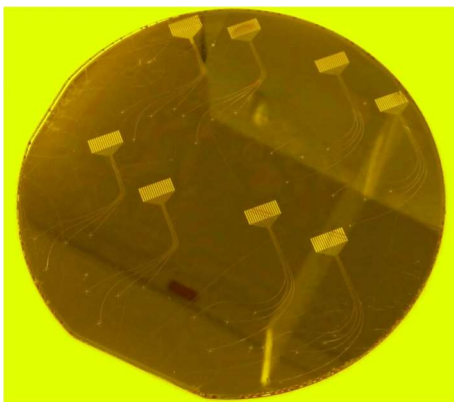


Figure 46 Fabricated mouse fore-limb array; 16 electrodes are spatially arranged in a cluster of 4 electrodes for picking up EMG from different locations in the fore-limb

5.3 MEAs Characterization and EMG Measurements

5.3.1 Electrical Characterization of Fabricated MEAs

Four-point resistance measurements for the trace and electrodes on the fabricated devices were measured, as shown in Figure 47. The average resistance of the traces for the 200, 125 and 50 μm diameter electrodes is summarized in Table 9. The electrode size did not impact the DC resistance significantly as the resistance was primarily determined by the metal trace and the slight variation can be attributed to fabrication process variation and the exact probe placement during the four-point resistance measurement.

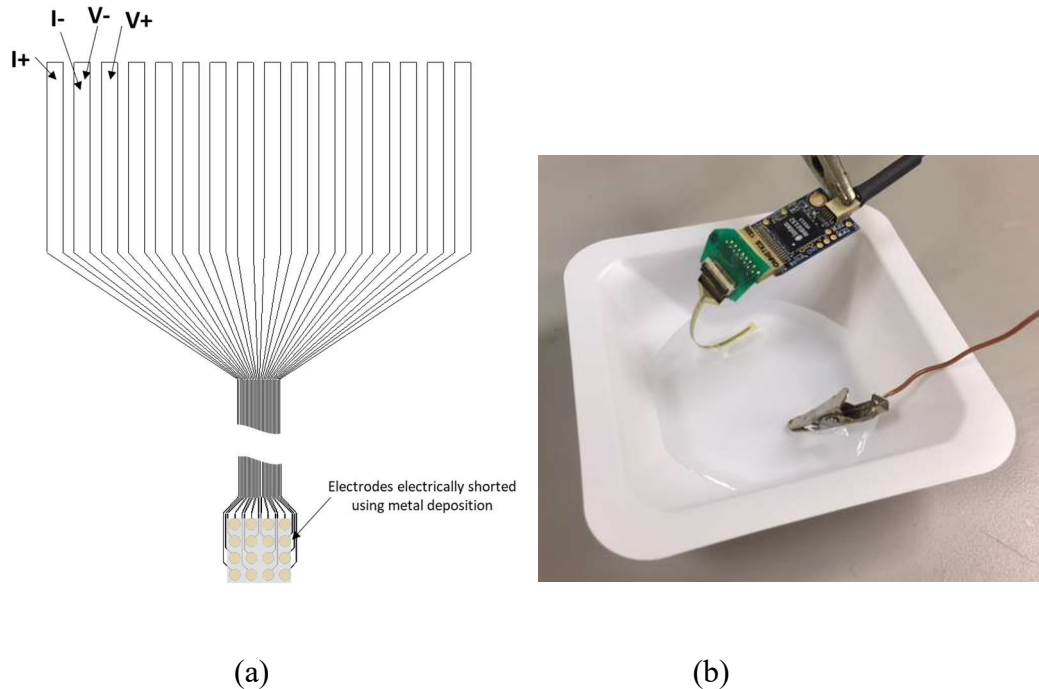


Figure 47 Characterization of electrical properties for different electrode sizes. (a) Schematic of four-point DC resistance measurement across traces for each electrode array. (b) Image of impedance measurement at 1,000 Hz where each electrode array is submerged in a grounded bath of saline.

To characterize biologically relevant electrical properties, the impedance at 1,000 Hz was measured with an Intan RHD2000 Eval board (Intan Technologies). The MEA devices were submerged in a grounded bath of saline (10% saline solution, TEKNOVA) and connected via a ZIF-clip/Omnetics adapter to an Intan RHD 2132 amplifier board (Intan Technologies; Figure 47(b)). The average impedances for the 200, 125, and 50 μm diameter electrodes are also reported in Table 9.

Table 9 Range of trace resistance and electrode impedance for each electrode contact site

Contact Diameter (μm)	Average Trace Resistance	Average Electrode Impedance (Songbird Array)	Average Electrode Impedance (Mouse Array)
50	234 Ω	556 k Ω	
125	235 Ω	107 k Ω	22 k Ω
200	233 Ω	77 k Ω	

5.3.2 EMG Measurements

A data collection flowchart from the songbird experiment is summarized in Figure 48. EMG activity was recorded from the expiratory muscles of anesthetized songbirds using the flexible MEA devices described above or a pair of fine-wire electrodes made from 25 μm -diameter stainless steel wire. All procedures were approved by the Emory University

Institutional Animal Care and Use Committee. EMG recordings for the polyimide-PDMS devices were collected using 16 contacts that were 200, 125, and 50 μm in diameter and arranged in a 4x4 matrix. Example EMG units recorded on one of the 16 contacts were chosen based on their physiological properties including the type of burst exhibited during breathing cycles and the relative amplitude in comparison to other EMG units that were simultaneously recorded.

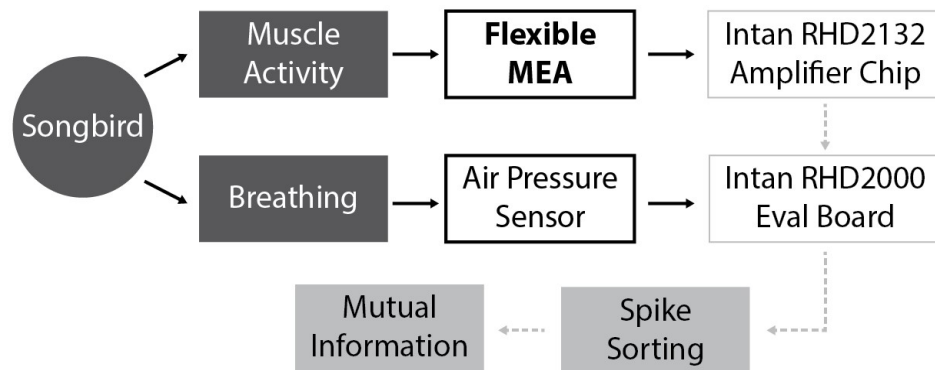


Figure 48 Data collection flow chart. Rhythmic muscle activity generates air pressure during breathing (dark gray). Analog signals (solid arrows) are detected by the Flexible MEA and an Air Pressure Sensor (black outlined boxes). EMG activity from the Flexible MEA is amplified and digitized by the Intan RHD2132 Amplifier Chip and air pressure data are digitized by the Intan RHD2000 Eval Board (light gray outlined boxes). The Eval Board records digital signals (dashed arrows) for both EMG and air pressure data for analysis (gray boxes). Spike sorting is used to distinguish individual motor units and mutual information is used to analyze neural activity and behavior.

The EMG units shown here (Figure 49) fired rhythmically throughout the expiration phase of each breathing cycle. These EMG units were also the smallest units identified within each recording. A qualitative comparison of the different electrode diameters (Figure 49(a-c)) does not show significant differences in signal fidelity. To illustrate the extent to which the MEAs represent a significant improvement over standard, fine-wire EMG techniques,

Figure 49 (d) shows a fine-wire recording from the expiratory muscle. As is typical of wire EMG recordings, the recorded signal consists of many overlapping spike waveforms (in comparison to the isolated recordings of single units shown in Figure 49(a-c). Figure 50

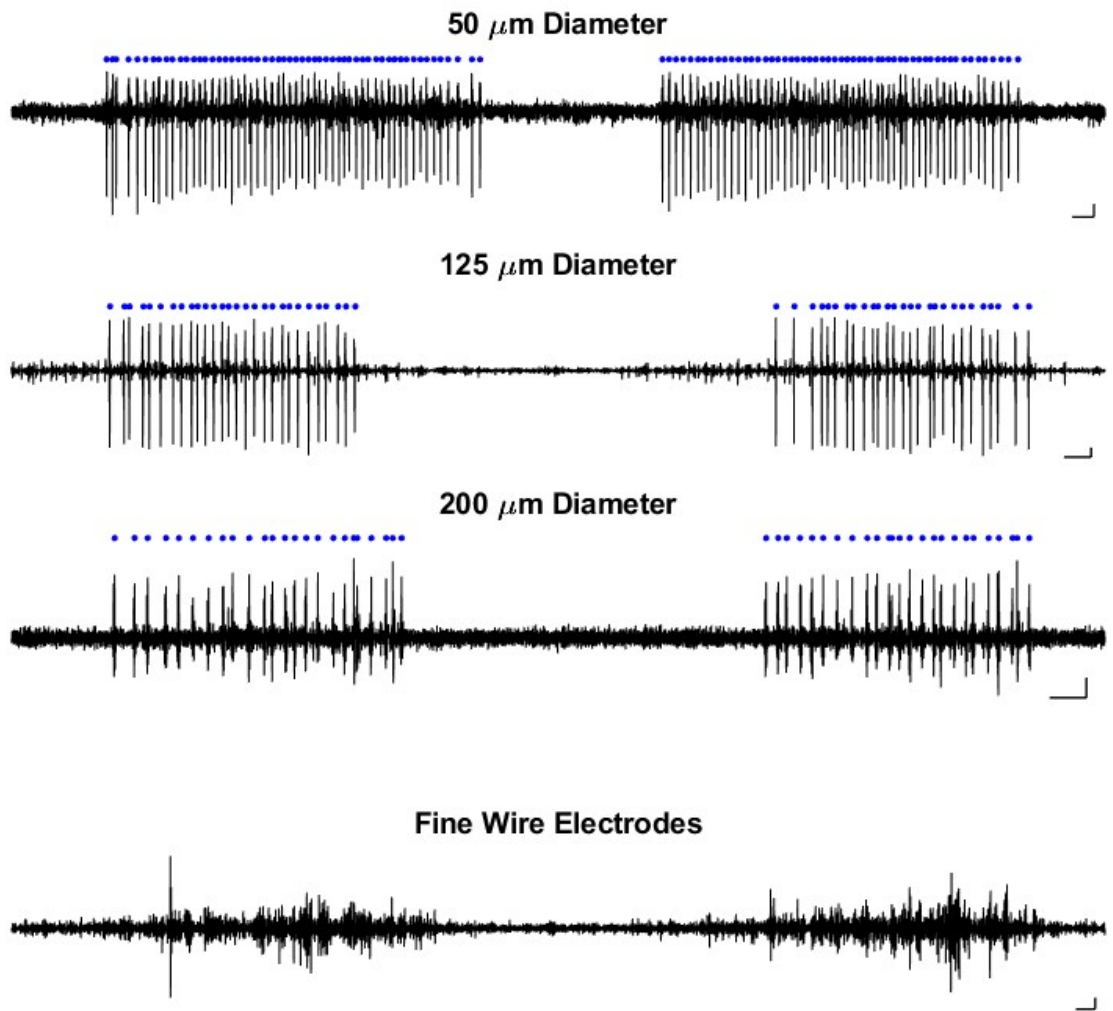


Figure 49 EMG recordings of expiratory muscle activity using two types of MEA devices. (a-c) EMG activity during 2 breathing cycles shows comparable signal qualities for all electrode sizes. Blue tick marks indicate spike times identified using a previously-described spike-sorting algorithm [11]. Time scale: 30 ms. Vertical scale: (a,b) 50 μV , (c) 20 μV . (d) EMG activity recorded using a pair of fine-wire electrodes, which, in this recording, the waveforms of individual spikes were not sufficiently distinct to be isolated by spike sorting. Time scale: 30 ms. Vertical scale: 1000 units.

shows the preliminary EMG data collected from the mouse shoulder array. The data shows high SNR empirical for subsequent data analysis which will be done as part of the future work from the presented work.

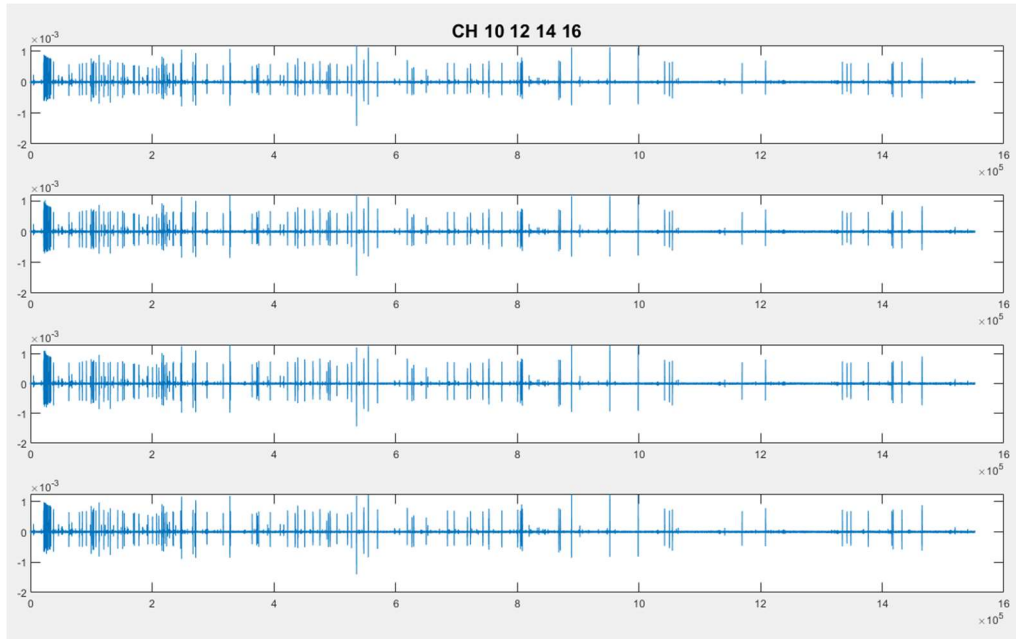


Figure 50 EMG recording from mouse shoulder muscle using the fabricated MEAs

5.4 Conclusion

In vivo EMG recordings from breathing muscles of a songbird utilizing hybrid polyimide-PDMS flexible multi-electrode array are presented. As the need for larger and more complex MEA devices grows new fabrication processes will need to be developed to address several challenges of current recording technologies. While individual polymers offer specific advantages, they also present different constraints. Here, a fabrication process was developed in order to reduce fabrication costs and time while still maintaining

the fidelity of biological recordings. In addition to using a “hybrid polymer” substrate approach to the fabrication process, other device properties that can be changed to improve single EMG unit recording quality is to use raised contact sites or other materials, such as carbon nanofibers.

CHAPTER 6. FABRICATION AND CHARACTERIZATION OF 3D MULTI-ELECTRODE ARRAY ON FLEXIBLE SUBSTRATE FOR IN VIVO EMG RECORDING FROM EXPIRATORY MUSCLE OF SONGBIRD

6.1 Introduction

This chapter extends the work presented in Chapter 5 and presents fabrication and characterization of 3D multi-electrode array on a flexible substrate. As mentioned earlier, understanding how nervous systems produce behaviors requires recording devices and algorithms that can identify individual motor events, called muscle potentials. However, obtaining high fidelity recordings suitable for neural analyses remains a critical bottleneck and requires: biological compliance of recording devices and high signal-to-noise ratio. In addition, characterizing single motor unit activity requires a stable, reliable EMG recording for a duration long enough to produce sufficient data for advanced computational analyses [69,70].

Polymer materials including polyimide, PDMS and parylene-C have been widely used for the fabrication of high-density multi-electrode arrays. To increase the signal fidelity, three-dimensional neural and muscular recording devices have also been explored [148-151]. However, these involve complex processing methodologies increasing the fabrication complexity, cost and time.

To address these challenges, this chapter presents fabrication and characterization of a flexible 3D MEA utilizing a simple photoresist reflow process to obtain the 3D electrodes.

The process described has been adapted from the micro-inductor fabrication process discussed in Chapter 3. The photoresist reflow process, as in the case of the micro-inductor, allows for the formation of the 3D electrodes. Polyimide is the base substrate for better metal adhesion and PDMS is the top insulation layer as it is more affordable, easier to etch and can be diluted to obtain thin top insulation layer. The height of the 3D electrodes can easily be modulated by changing the film thickness of the spin coated photoresist. *In vivo* EMG measurements from an anesthetized songbird are also presented. The fabricated 3D MEAs provide up to 7x SNR improvement over the 2D array, described in Chapter 5, allowing detection of small units which can otherwise get lost in noise.

6.2 Fabrication of 3D Multi-Electrode Arrays

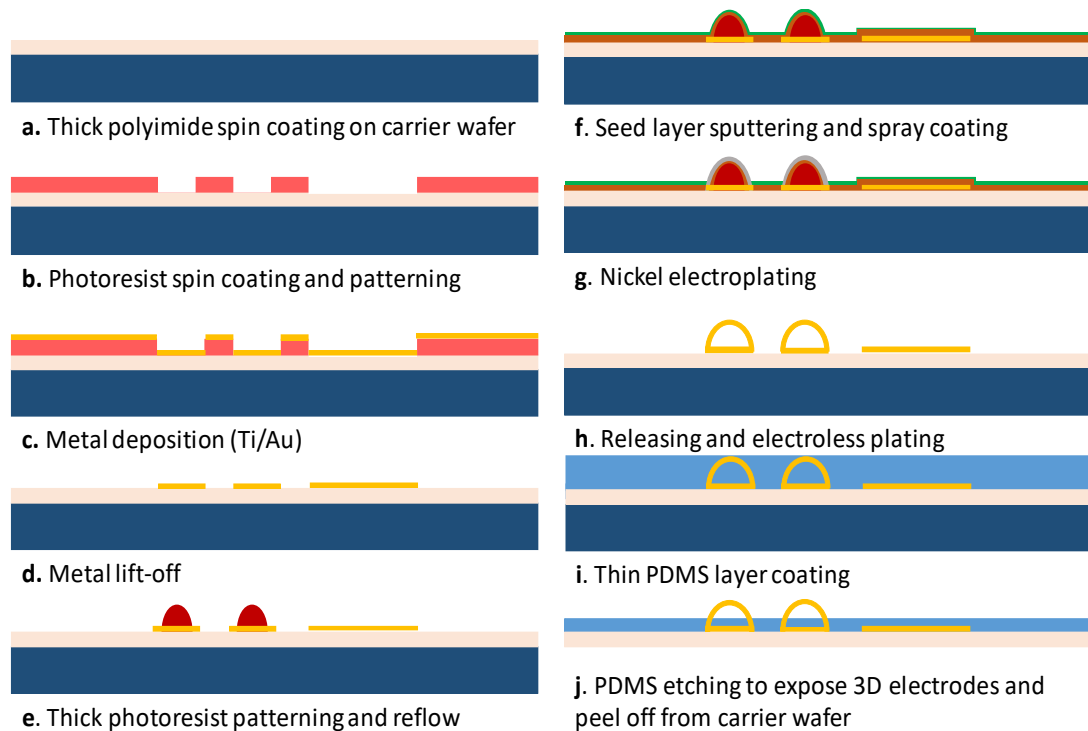


Figure 51 Fabrication process flow for the flexible 3D MEAs

The fabrication process of the 3D MEAs is outlined in Figure 51. Polyimide (PI-2611 from HD Microsystems) is spin coated @ 450 rpm on a carrier wafer and subsequently cured to get a thick polyimide film. Photoresist is then spin coated and patterned followed by metallization and a lift-off process. A Ti/Au layer of 30nm / 200nm is deposited using an evaporation process. Thick photoresist (AZ-40XT) is then spin coated and patterned using photolithography, which is then reflowed to form the hemispherical structures as shown in Figure 51(e). Figure 52 shows the profilometer scan of the reflowed photoresist domes.

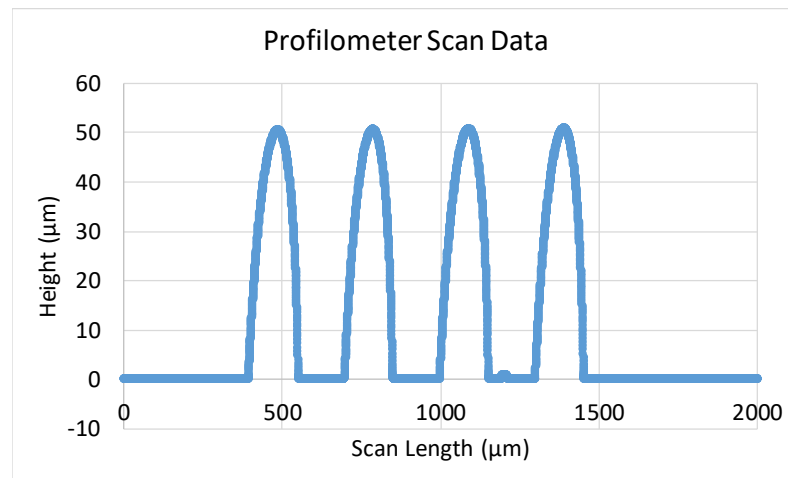
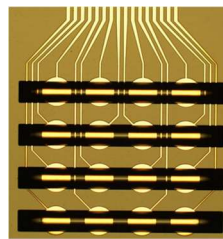


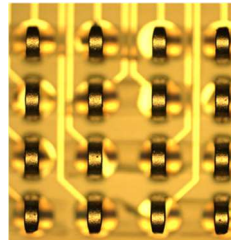
Figure 52 Profilometer scan data after reflow of photoresist to form the hemispherical domes (step (e) in the process flow). A 50 µm dome height was obtained for the 3D MEAs and can be modulated by changing the photoresist film thickness.

The double-reflow process described in [155] can also be utilized here to obtain multi-height 3D electrodes in the same fabrication flow. An electroplating seed layer consisting of 50 nm of Ti and 300 nm of Cu is subsequently sputtered. Photoresist is then spray coated

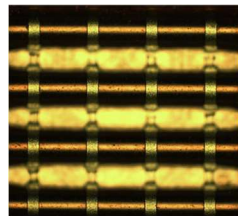
and the electroplating mold is formed. Nickel electroplating (10 μm thick) is then performed followed by the removal of the underlying photoresist and the seed layer to give the free-standing 3D MEAs. Electroless gold plating is then performed to passivate the electrode surface and prevent oxidation. To obtain the top insulation layer, a thin coating of PDMS (Sylgard 184, 1:10 ratio) diluted with toluene (0.9% weight ratio) is obtained and then cured. A reactive-ion etching (RIE) process is then used to etch the PDMS to expose the 3D electrodes. SF_6 and O_2 were used as the etching gases with a flow rate of 90 and 6 sccm respectively while the RF power was 300 watts. The etch rate obtained for the PDMS was $\sim 170 \text{ nm/ min}$. Optical images of the MEAs through the fabrication process are summarized in Figure 53. The final 3D electrodes obtained are shown in Figure 54.



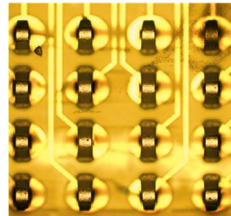
After step (e)



After step (h)



After step (g)



After step (j)

Figure 53 Optical images of fabricated 3D MEAs

6.3 EMG Measurement and SNR Comparison

EMG and air pressure data were collected as outlined in Figure 48. Rhythmic muscle activity generates air pressure during breathing. Analog signals are detected by the flexible MEA and an air pressure sensor. EMG activity from the flexible MEA is amplified and digitized by an Intan RHD2216 bipolar amplifier chip. Air pressure data was also simultaneously collected using a pressure sensor connected to a tube inserted into the air sac of the anesthetized songbird. The Intan RHD 2000 evaluation board records digital signals for both EMG and air pressure data for analysis. Spike sorting is used to distinguish individual motor units from background noise and mutual information is then used to determine the correlation between neural activity and behavior. Both 3D and 2D arrays were used to record EMG activity from the expiratory muscles of anesthetized songbirds. All procedures were approved by the Emory University Institutional Animal Care and Use Committee. EMG recordings for the flexible MEA devices were collected using 16 contacts arranged in a 4x4 matrix. Example EMG units recorded on one of the 16 contacts

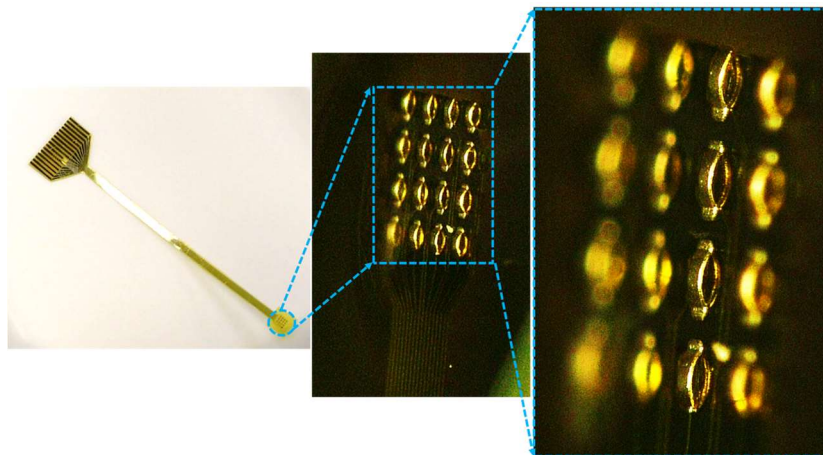
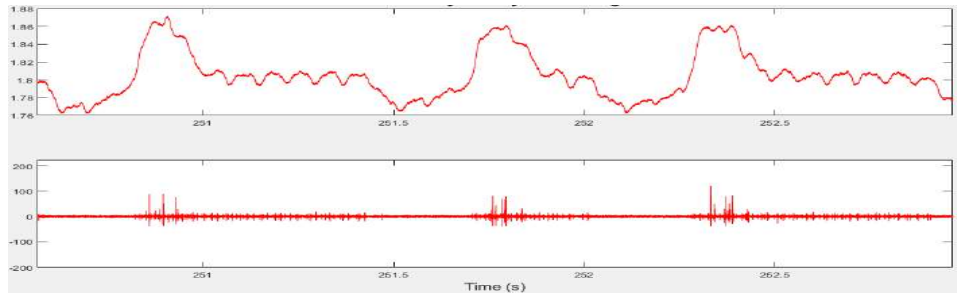


Figure 54 3D optical images of the fabricated 3D MEAs

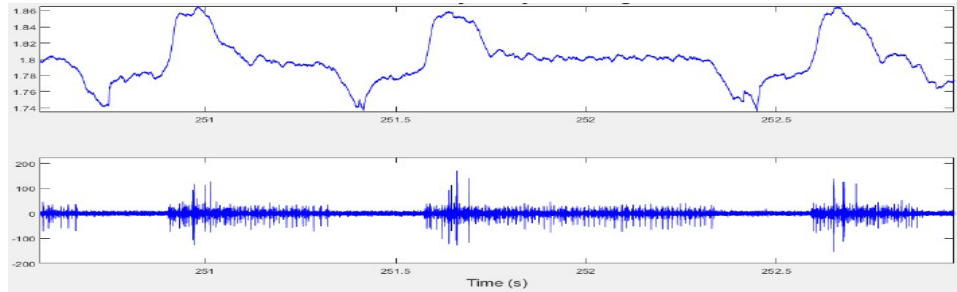
were chosen based on their physiological properties including the type of spiking exhibited during breathing cycles (i.e., spiking at a constant, moderate firing rate versus only a few spikes at a higher firing rate) and the relative amplitude in comparison to other EMG units that were simultaneously recorded.

The data collection sequence of experiments for comparison of the SNR was conducted as follows: A total of four recordings of at least 30 minutes each were carried out alternating between 2D and 3D MEAs. After each recording and before the placement of the next MEA, a drop of saline was poured on the exposed expiratory muscle. Care was taken to ensure that the electrode placement was roughly over the same area of the expiratory muscle of the bird. Figure 55 shows the EMG measurements along with the pressure data from the air sac of the bird. As seen from the figure, the 3D MEAs pick up more activity from the muscle as compared to the 2D MEA and give a more consistent recording across trials. On the other hand, the 2D array's signal deteriorates from one trial to the next; this can be attributed to poor contact with the muscle due to protein or other unwanted material build up as the EMG recording duration increases; this is also exacerbated by the fact that the electrodes are inset below the surface of the top PDMS insulation layer. SNR calculations were performed by taking the ratio of the root-mean-square (RMS) amplitude of the waveforms during periods of activity with large or small units (signal) over periods of noise. Figure 56 shows the SNR for the 2D and 3D MEAs over the course of the four different trials that were carried out. An average SNR was calculated in 3-minute intervals with 4 measurements during each interval used to determine the standard error of the mean (shaded region in Figure 56).

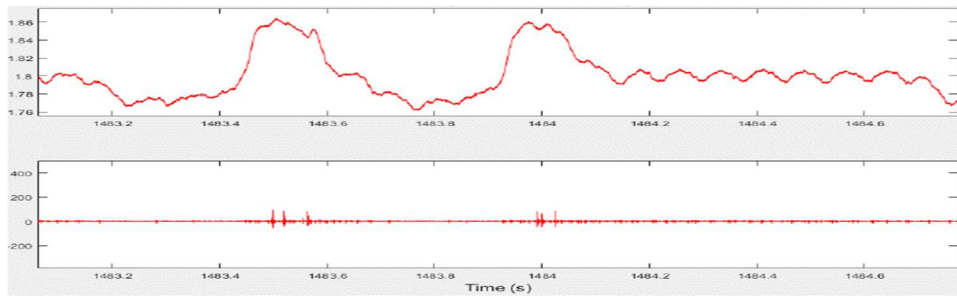
Table 10 summarize the SNR measurements for the 2D and 3D electrodes over the different trials carried out for small and large amplitude unit activity; the 3D MEAs provide significant improvement in SNR for both small and large units with a 3.5x SNR improvement 5 minutes after the array placement and more than 7x SNR improvement 25 minutes into the recording for the larger unit. Improvement of SNR within a trial over time can be explained by better contact of the electrodes with the muscle as the saline dries out.



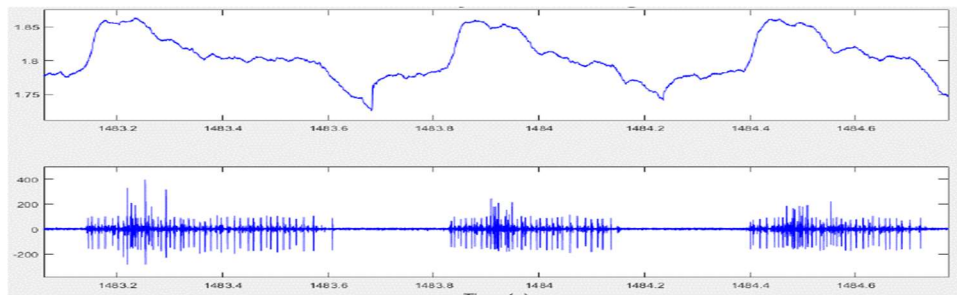
(a)



(b)



(c)



(d)

Figure 55 Example air pressure and electromyograph recordings. (a,b) EMG recording after 5 minutes of array placement on the expiratory muscle of the songbird with (a) flexible 2D MEA, and (b) flexible 3D MEA. (c,d) EMG recording after 25 minutes of array placement on the expiratory muscle of songbird with (c) flexible 2D MEA, and (d) flexible 3D MEA.

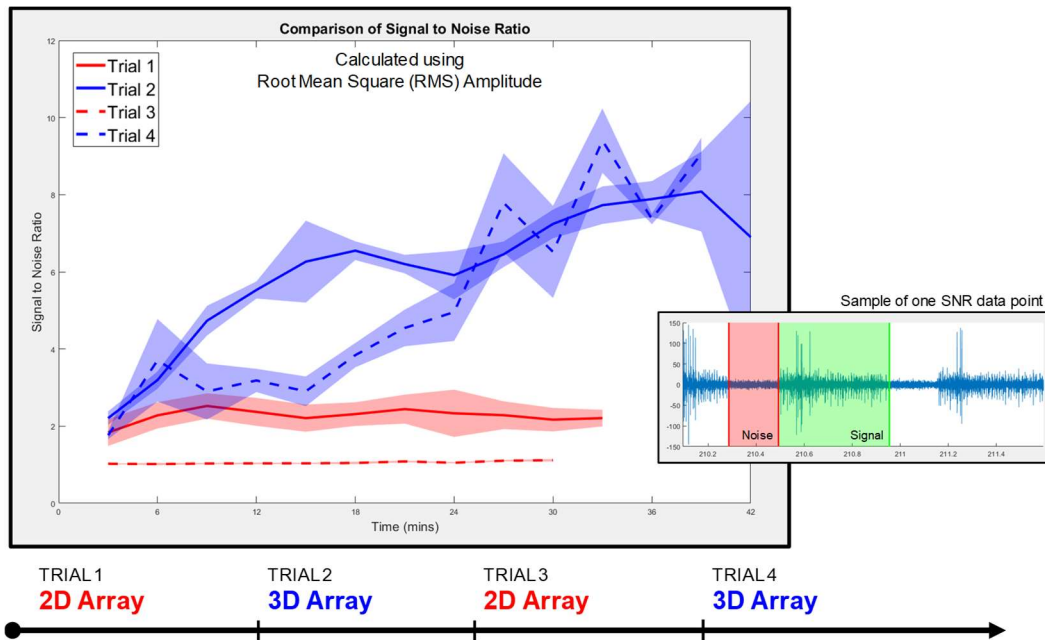


Figure 56 Comparison of signal-to-noise ratio (SNR) using multi-electrode arrays with either 2D (red) or 3D (blue) electrode sites. Recordings for each trial were collected over at least 30-minute periods and alternated between 2D and 3D MEAs to control for non-stationary factors of the in vivo preparation. An average (solid or dashed line) SNR was calculated every 3 minutes with 4 measurements during each minute to determine a standard error of the mean (shaded regions).

Table 10 SNR comparison of EMG signal recorded using the 2D and 3D MEAs. N/A is listed where signal was not discernable from noise.

Trial #	Contact Type	Time Since Array placement (mins)	Large Unit SNR	Small Unit SNR
1	2D	5	3.76	1.74
		25	3.58	1.79
2	3D	5	4.68	2.77
		25	8.99	5.70
3	2D	5	1.02	N/A
		25	1.18	N/A
4	3D	5	3.59	2.12
		25	8.45	6.82

6.4 Conclusion

A flexible 3D MEA for high SNR in vivo EMG recordings is presented. The process flow allows for easy height modulation of 3D electrodes by changing the film thickness of the photoresist. An Intan RHD2000 evaluation board and an RHD2216 amplifier chip is used to record expiratory muscle EMG activity and air pressure data. The 3D MEAs yielded higher SNR measurements over a longer duration of time as compared a 2D array. This is particularly important for detecting and analyzing smaller units which are otherwise lost in noise. Using the 3D arrays, an SNR of up to 7x was achieved and some of the improvement may have been due to better electrical isolation as excess liquid dried around the recording site. With better signal fidelity, individual units can be identified more reliably and for longer periods of time, which will allow more advanced analysis techniques that can be used to understand how nervous systems control behavior.

CHAPTER 7. SUMMARY AND FUTURE WORK

The core contributions of the thesis in the domain of heterogeneous integration and biosensing are:

- The utilization of photoresist reflow process for the fabrication and assembly of large-scale silicon system comprising of multiple interposers bridged with high-density flexible interconnects via a silicon bridge. System level analysis of the bridged interposers is also presented to highlight the bandwidth and energy trade-offs between electrical and optical interconnects in such a system.
- The adaptation and modification of the flexible interconnect fabrication process for simultaneous fabrication of flexible I/Os alongside 3D solenoidal micro-inductors. The unique fabrication process allows fabrication of flexible I/Os with varying thickness, height, pitch and material enabling close integration of actives and passives.
- The utilization of the technologies (PSAS, MFI, TSV) developed for the heterogeneous integration applications into fabricating a 3D integrated electronic microplate enabling high-throughput low-cost biosensing. The e-microplate enables 3D electrical interconnections using TSVs and flexible interconnects between living cells and CMOS biosensor while maintaining a physical separation. The addition of the e-microplate does not affect the amplifier's gain or the input referred noise.
- Utilizing high-density interconnect knowledge base from the heterogeneous integration and combining it with flexible substrate fabrication to fabricate and

characterize 2D multi-electrode arrays for *in vivo* EMG recording from expiratory muscle of a songbird and the fore-limb of a mouse. The fabrication process presented utilizes both polyimide and PDMS to leverage the benefits of each of the materials while keeping the fabrication process simple.

- Incorporating flexible interconnect fabrication process to extend the flexible MEA fabrication to develop 3D multi-electrode array for high SNR *in vivo* EMG measurements. The fabrication process presented enables high aspect ratio 3D multi-electrode array allowing better contact with the animal muscle resulting in up to 7x improvement in SNR.

7.1 Future Work

The potential extensions and advancement of the work presented in this dissertation will be discussed in this section.

7.1.1 Heterogeneous integration

- (a) The multi-interposer system work presented outlines a framework for both electrical and optical interconnect. Building on the work presented, a full system realization with both optical and electrical interconnects must be assembled. The model presented in this dissertation can function as a guideline to determine the system size and the optimal interconnection scheme for such a system.
- (b) For the 3D micro-inductors, a comprehensive trade-off analysis with respect to the number of turns, height of the loop and material of the inductors must be performed. This will be essential in determining the optimal size of the micro-inductor and provide a guideline for selecting the right topology for different applications.

7.1.2 *In vitro and in vivo biosensing*

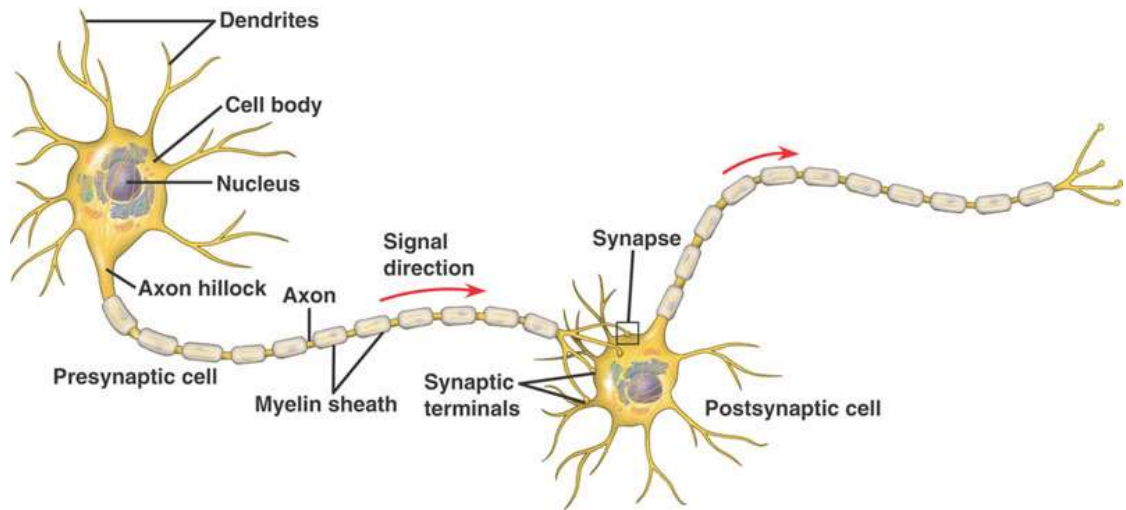


Figure 57 Example showing conduction along two neurons – a major motivation for HD E-microplate is being able to trace the exact path of the electrical activity

- (a) The electronic microplate platform for in vitro biosensing should be extended to enable high-density RDL on the top surface for sub-cellular imaging. This is important for applications like studying the conduction of action potential along a

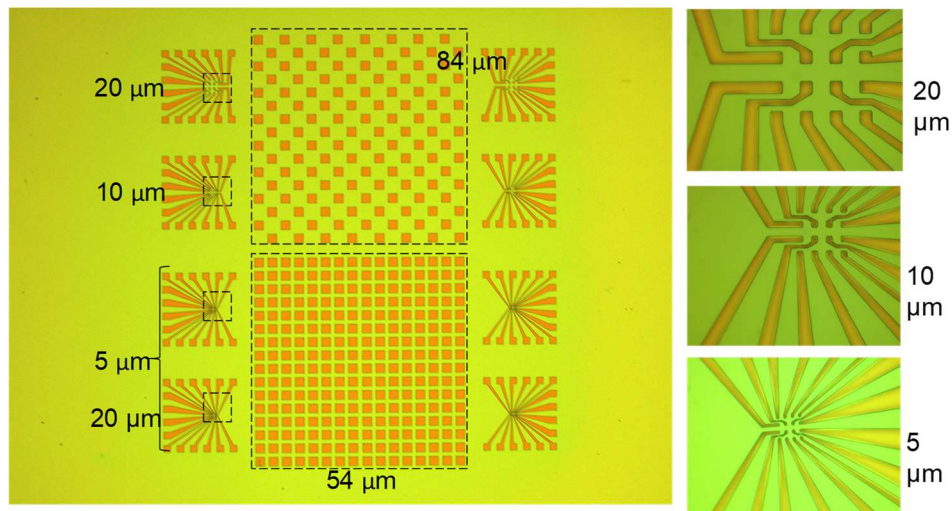


Figure 58 RDL layout for realizing HD E-microplate without scaling the TSVs or flexible interconnects

neuron (Figure 57); if the electrode density is not high enough, the travelling impulse can get ‘lost’ in real time measurements as the origin of the electrical activity among multiple neurons cannot be differentiated and hence studies aimed at understanding, for example, neural plasticity, cannot be performed effectively. Figure 58 shows RDL option for realizing the HD E-microplate. The layout presented can enable localized high-density regions on the e-microplate without the need to scale the TSVs and the flexible interconnects which otherwise can be challenging. In addition to this, e-microplate with other biocompatible, for example TCPS, materials should also be explored to reduce the cost further and possibly introduce for point-of-care applications.

- (b) The multi-electrode array for *in vivo* EMG recording presented fabrication of the devices using a hybrid polyimide-PDMS approach. A detailed characterization of the benefits/shortcomings of MEAs fabricated with different materials should be

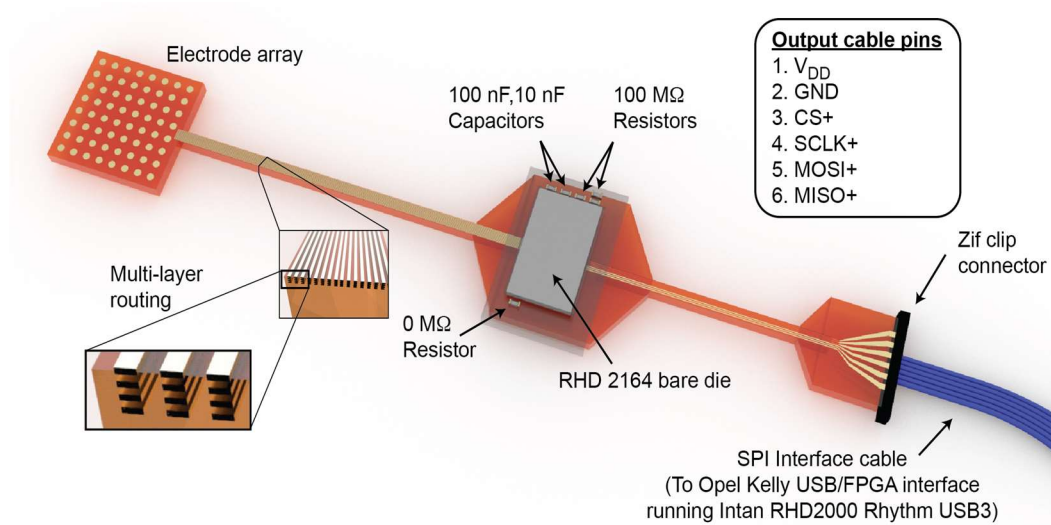


Figure 59 Future vision of multi-electrode array with multi-layer high-density RDL and integrated signal conditioning IC

performed. The impact of top insulation layer on SNR should also be studied in order to determine the optimal thickness.

A high-density multi-electrode array with significantly more number of electrodes should also be explored. This can allow single-unit recordings from multiple muscle fibers allowing a large data set for analyses. Increasing the number of electrodes, however, would require devices that can have multi-layer high-density RDL alongside close integration of active circuit. This can reduce the overall noise in the system and alleviate the need for having a large number of wires coming out of the animal. A concept design of such an array is shown in Figure 59.

In addition to advancing technology side, significant effort is also required to analyze the data collected and make meaningful conclusions. Thus, a holistic system capable of high-SNR recording and subsequent data analysis should be explored for rapid analyses of large set of spike data.

REFERENCES

- [1] Xuezhe Zheng; Krishnamoorthy, A.V., "Si photonics technology for future optical interconnection," in Communications and Photonics Conference and Exhibition, 2011. ACP. Asia , vol., no., pp.1-11, 13-16
- [2] Kam, D.G. et al, "Is 25 Gb/s On-Board Signaling Viable?," in Advanced Packaging, IEEE Transactions on , vol.32, no.2, pp.328-344, May 2009
- [3] Kuwahara, T et al, "A study of high-density differential transmission line of the package board based on crosstalk reduction," in Electronics Packaging and iMAPS All Asia Conference (ICEP-IACC), 2015 International Conference on , vol., no., pp.878-881, 14-17 April 2015
- [4] Braunisch, H. et al, "High-Speed Flex-Circuit Chip-to-Chip Interconnects," in Advanced Packaging, IEEE Transactions on , vol.31, no.1, pp.82-90, Feb. 2008
- [5] Schares, L. et al, "Terabus: Terabit/Second-Class Card-Level Optical Interconnect Technologies," in Selected Topics in Quantum Electronics, IEEE Journal of , vol.12, no.5, pp.1032-1044, Sept.-Oct. 2006
- [6] Doany, F.E et al, "Terabit/s-Class Optical PCB Links Incorporating 360-Gb/s Bidirectional 850 nm Parallel Optical Transceivers," in Lightwave Technology, Journal of , vol.30, no.4, pp.560-571, Feb.15, 2012
- [7] Kim, N. et al "Interposer design optimization for high frequency signal transmission in passive and active interposer using through silicon via (TSV)," Electronic Components and Technology Conference (ECTC), 2011 IEEE 61st , vol., no., pp.1160,1167, May 31 2011-June 3 2011
- [8] Braunisch, H.; Aleksov, A.; Lotz, S.; Swan, J., "High-speed performance of Silicon Bridge die-to-die interconnects," in Electrical Performance of Electronic Packaging and Systems (EPEPS), 2011 IEEE 20th Conference on , vol., no., pp.95-98, 23-26 Oct. 2011
- [9] Nakamura, T. et al, "High-density silicon optical interposer for inter-chip interconnects based on compact and high speed components," Lasers and Electro-Optics (CLEO), 2013 Conference on , vol., no., pp.1,2, 9-14 June 2013.
- [10] H. Wu; M. Khmour; P. Apsangi; H. Yu, "High Frequency Magnetic Thin Film Inductor Integrated on Flexible Organic Substrates," in IEEE Transactions on Magnetics , 2017.
- [11] T. Akagi, S. Abe, M. Hatanaka and S. Matsumoto, "An isolated DC-DC converter using air-core inductor for power supply on chip applications," 2015 IEEE International Telecommunications Energy Conference (INTELEC), Osaka, 2015, pp. 1-6.
- [12] N. Wang, T. O'Donnell, S. Roy, P. McCloskey, and C. O'Mathuna, "Micro-inductors integrated on silicon for power supply on chip," J. Magn. Mater., vol. 316, no. 2, pp. e233–e237, Sep. 2007.

- [13] E.-C. Park, J.-B. Yoon, S. Hong, and E. Yoon, "A 2.6 GHz low phasenoise VCO monolithically integrated with high Q MEMS inductors," in Proc. IEEE 28th Eur. Solid-State Circuits Conf. (ESSCIRC), Sep. 2002, pp. 147–150.
- [14] C. Zhang, L. Guo, L. F. Wang, J. Q. Huang and Q. A. Huang, "A passive wireless integrated humidity sensor based on dual-layer spiral inductors," IEEE SENSORS 2014 Proceedings, Valencia, 2014, pp. 657-660.
- [15] H. Wang, "Magnetic sensors for diagnostic medicine: CMOS-based magnetic particle detectors for medical diagnosis applications," IEEE Microwave Magazine, vol. 14, no. 5, pp. 110-130, Jul/Aug 2013.
- [16] M. Schienle, et al., "A fully electronic DNA sensor with 128 positions and in-pixel A/D conversion," IEEE J. Solid-State Circuits, vol. 39, no. 12, pp. 2438–2445, Dec. 2004.
- [17] F. Heer, et al., "CMOS electro-chemical DNA-detection array with on-chip ADC," in IEEE ISSCC Dig. Tech. Papers, Feb. 2008, pp. 168–169, 604.
- [18] B. Jang, P. Cao, A. Chevalier, A. Ellington, A. Hassibi, "A CMOS fluorescence-based biosensor microarray," in IEEE ISSCC Dig. Tech. Papers, Feb. 2009, pp. 436–437, 437a.
- [19] D. Hall, et al., "A 256 channel magnetoresistive biosensor microarray for quantitative proteomics," in IEEE VLSI Circuits (VLSIC), 15–17 June 2011, pp. 174–175.
- [20] S. Gambini, et al., "A CMOS 10kpixel baseline-free magnetic bead detector with column-parallel readout for miniaturized immunoassays," in IEEE ISSCC Dig. Tech. Papers, Feb. 2012, pp. 126–128.
- [21] H. Wang, A. Mohdavi, D. Tirrell, and A. Hajimiri, "A magnetic cell based sensor," Lab Chip, Vol. 12, Issue 21, pp. 4465–4471, 2012.
- [22] H. Wang, S. Kosai, C. Sideris, and A. Hajimiri, "An ultrasensitive CMOS magnetic biosensor array with correlated double counting noise suppression," IEEE MTT-S Int. Microwave Symp. (IMS), pp.616-619, May 2010.
- [23] B. Eversmann, et al., "A 128×128 CMOS biosensor array for extracellular recording of neural activity," IEEE JSSC, vol. 38, no. 12, Dec. 2003.
- [24] Srivastava KH, et al. Motor control by precisely timed spike patterns. PNAS, vol. 114, iss. 5, pp. 1171-1176, January 2017.
- [25] P. N. Gad et al., "Using in vivo spinally-evoked potentials to assess functional connectivity along the spinal axis," 2013 6th International IEEE/EMBS Conference on Neural Engineering (NER), San Diego, CA, 2013, pp. 319-322.
- [26] A. Tooker et al., "Towards a large-scale recording system: Demonstration of polymer-based penetrating array for chronic neural recording," 2014 36th Annual International Conference of the IEEE Engineering in Medicine and Biology Society, Chicago, IL, 2014, pp. 6830-6833.
- [27] K. G. Shah et al., "Chronic, percutaneous connector for electrical recording and stimulation with microelectrode arrays," 2014 36th Annual International Conference

- of the IEEE Engineering in Medicine and Biology Society, Chicago, IL, 2014, pp. 5240-5243.
- [28] A. M. Belle et al., "Measurement of glutamate in dorsal root ganglion cell culture with integrated electrochemical biosensors," 2017 IEEE International Symposium on Medical Measurements and Applications (MeMeA), Rochester, MN, 2017, pp. 453-457.
- [29] A. Tooker et al., "Optimization of multi-layer metal neural probe design," 2012 Annual International Conference of the IEEE Engineering in Medicine and Biology Society, San Diego, CA, 2012, pp. 5995-5998.
- [30] A. Tooker et al., "Microfabricated polymer-based neural interface for electrical stimulation/recording, drug delivery, and chemical sensing - development," 2013 35th Annual International Conference of the IEEE Engineering in Medicine and Biology Society (EMBC), Osaka, 2013, pp. 5159-5162.
- [31] Dickson, T.O et al, "An 8x 10-Gb/s Source-Synchronous I/O System Based on High-Density Silicon Carrier Interconnects," in Solid-State Circuits, IEEE Journal of , vol.47, no.4, pp.884-896, April 2012.
- [32] Ho, R. et al, "Optical Interconnect for High-End Computer Systems," in Design & Test of Computers, IEEE , vol.27, no.4, pp.10-19, July-Aug. 2010.
- [33] Ho, R. et al, "Silicon Photonic Interconnects for Large-Scale Computer Systems," in Micro, IEEE , vol.33, no.1, pp.68-78, Jan.-Feb. 2013.
- [34] Jin Yao et al, "Optical interlayer coupling design for optical interconnects based on mirror enhanced grating couplers," in Optical Interconnects Conference, 2012 IEEE , vol., no., pp.27-28, 20-23 May 2012.
- [35] Shubin, I. et al, "All solid-state multi-chip multi-channel WDM photonic module," in Electronic Components and Technology Conference (ECTC) , 2015 IEEE 65th , vol., no., pp.1293-1298, 26-29 May 2015.
- [36] Thacker, H.D. et al, "An all-solid-state, WDM silicon photonic digital link for chip-to-chip communication," in Opt. Express 23(10), pp. 12808-12822 (2015).
- [37] S. G. Chow, Y. Lin, B. Adams and S. W. Yoon, "Board level reliability improvement in eWLB (embedded wafer level BGA) packages," 2016 11th International Microsystems, Packaging, Assembly and Circuits Technology Conference (IMPACT), Taipei, 2016, pp. 139-142.
- [38] L. Tian, Y. Zhao, Q. Yao, Y. Cao and B. Lian, "The reliability of high-lead solder joints in flip-chip devices," 2014 15th International Conference on Electronic Packaging Technology, Chengdu, 2014, pp. 847-849.
- [39] M. Su, B. Black, Y. H. Hsiao, C. L. Changchien, C. C. Lee and H. J. Chang, "2.5D IC Micro-Bump Materials Characterization and IMCs Evolution Under Reliability Stress Conditions," 2016 IEEE 66th Electronic Components and Technology Conference (ECTC), Las Vegas, NV, 2016, pp. 322-328.
- [40] Z. Leng, M. Xiao, M. He, W. Xia and B. Wang, "Electromigration simulation of Cu pillar interconnect microstructure of 3D packaging," 2016 17th International

- Conference on Electronic Packaging Technology (ICEPT), Wuhan, 2016, pp. 234-239.
- [41] Y. Lin, C. Kang, L. Chua, W. K. Choi and S. W. Yoon, "Advanced 3D eWLB-PoP (Embedded Wafer Level Ball Grid Array - Package on Package) Technology," 2016 IEEE 66th Electronic Components and Technology Conference (ECTC), Las Vegas, NV, 2016, pp. 1772-1777.
- [42] Bakir M et al 2003 SoL ultra high density wafer level chip input/output interconnections for gigascale integration (GSI) IEEE Trans. Electron. Devices 50 2039–48
- [43] P. Xu, G. Hernandez, S. Wang, J. Zhong, C. Ellis and M. Hamilton, "Flip chip based on compliant double helix interconnect for high frequency applications," in Proc. IEEE Electronic Components and Technology Conference (ECTC), 2014, pp. 1086-1090.
- [44] Ma L, Zhu Q, Hantschel T, Fork D K and Sitaraman S K 2002 J-springs—innovative compliant interconnects for next generation packaging 57th Electronic Components and Technology Conf. (Reno, Nevada) pp 1359–65
- [45] Kacker K, Sokol T and Sitaraman S K 2007 Flex connects: a cost-effective implementation of compliant chip-to-substrate interconnects Proc. 57th Electronic Components and Technology Conf. (Reno, Nevada) pp 1678–84
- [46] Spanier G et al 2007 Platform for temporary testing of hybrid microsystems at high frequencies J. MEMS 16 1367–77
- [47] I. Shubin, E. Chow, J. Cunningham, D. De Bruyker, C. Chua, B. Cheng, J. C. Knights, K. Sahasrabudhe, Y. Luo, A. Chow, J. Simons, A. Krishnamoorthy, R. Hopkins, R. Drost, R. Ho, D. Douglas, and J. Mitchell, "Novel packaging with rematable spring interconnect chips for mcm," in Electronic Components and Technology Conference, 2009. ECTC 2009. 59th, May 2009, pp. 1053–1058.
- [48] I. Shubin, A. Chow, J. Cunningham, M. Giere, N. Nettleton, N. Pinckney, J. Shi, J. Simons, R. Hopkins, J. Mitchell, D. Douglas, E. Chow, D. DeBruyker, B. Cheng, and G. Anderson, "A package demonstration with solder free compliant flexible interconnects," in Electronic Components and Technology Conference (ECTC), 2010 Proceedings 60th, June 2010, pp. 1429–1435.
- [49] B. Cheng, D. De Bruyker, C. Chua, K. Sahasrabudhe, I. Shubin, J. Cunningham, Y. Luo, K. Bohringer, A. Krishnamoorthy, and E. Chow, "Microspring characterization and flip-chip assembly reliability," Components, Packaging and Manufacturing Technology, IEEE Transactions on, vol. 3, no. 2, pp. 187–196, Feb 2013.
- [50] L. Ma, Q. Zhu, T. Hantschel, D. Fork, and S. Sitaraman, "J-springs – innovative compliant interconnects for next-generation packaging," in Electronic Components and Technology Conference, 2002. Proceedings. 52nd, 2002, pp. 1359–1365.
- [51] J. L. Gonzalez, P. K. Jo, R. Abbaspour and M. S. Bakir, "Flexible Interconnect Design Using a Mechanically-Focused, Multi-Objective Genetic Algorithm," in Journal of Microelectromechanical Systems, vol. 27, no. 4, pp. 677-685, Aug. 2018.

- [52] Q. Zhu, L. Ma, and S. Sitaraman, “ β -helix: a lithography-based compliant offchip interconnect,” *Components and Packaging Technologies*, IEEE Transactions on, vol. 26, no. 3, pp. 582–590, Sept 2003.
- [53] J. N. Burghartz and B. Rejaei, "On the design of RF spiral inductors on silicon," in *IEEE Transactions on Electron Devices*, vol. 50, no. 3, pp. 718-729, March 2003.
- [54] S Uchiyama et al 2013 *J. Micromech. Microeng.* 23 114009.
- [55] T.C. Lee, Y-S Chang, C-M Hsu, S-C Hsieh, P-N Lee, Y-C Hsieh, L-C Wang and L. Zhang, "Glass based 3D-IPD integrated RF ASIC in WLCSP," 2017 IEEE 67th Electronic Components and Technology Conference (ECTC), Orlando, FL, 2017.
- [56] X. Yu, M. Kim, F. Herrault, C. H. Ji, J. Kim and M. G. Allen, "Silicon-embedded 3D toroidal air-core inductor with through-wafer interconnect for on-chip integration," 2012 IEEE 25th International Conference on Micro Electro Mechanical Systems (MEMS), Paris, 2012, pp. 325-328.
- [57] V. Badilita et al., “On-chip three dimensional microcoils for MRI at the microscale,” *Lab Chip*, vol. 10, no. 11, pp. 1387–1390, 2010.
- [58] L. Gu and X. Li, "High-Q Solenoid Inductors With a CMOS-Compatible Concave-Suspending MEMS Process," in *Journal of Microelectromechanical Systems*, vol. 16, no. 5, pp. 1162-1172, Oct. 2007.
- [59] C. Yang, S. Y. Wu, C. Glick, Y. S. Choi, W. Hsu and L. Lin, "3D printed RF passive components by liquid metal filling," 2015 28th IEEE International Conference on Micro Electro Mechanical Systems (MEMS), Estoril, 2015, pp. 261-264.
- [60] M. K. Bhuyan, J. I. Rodriguez-Devora, K. Fraser, and T.-L. Tseng, “Silicon substrate as a novel cell culture device for myoblast cells,” *Journal of Biomedical Science* 2014, 21:47.
- [61] N. J. Hallab, K. J. Bundy, K. O'Connor, R. L. Moses, and J. J. Jacobs, “Evaluation of metallic and polymeric biomaterial surface energy and surface roughness characteristics for directed cell adhesion,” *Tissue Engineering*, Feb. 2001, Vol. 7, No. 1, pp.55-71.
- [62] T.-W. Chung, D.-L. Liu, S.-Y. Wang, S.-S. Wang, “Enhancement of the growth of human endothelial cells by surface roughness at nanometer scale,” *Biomaterials* 24 (2003) 4655–4661.
- [63] R. A. Gittens, et. al., “The effects of combined micron-/submicron-scale surface roughness and nanoscale features on cell proliferation and differentiation,” *Biomaterials* 32 (2011) 3395-3403.
- [64] I. Keen, et. al., “Surface roughness and topography of Poly(3-hydroxybutyrate-co-3-hydroxyvalerate) influences osteoblast cell growth,” *Journal of Biomaterials Science, Polymer Edition* 18(9), pp. 1101-1123. 2007.
- [65] M. Jäger, et. al., “Osteoblast differentiation onto different biometals with an endoprosthetic surface topography in vitro,” *Journal of Biomedical Materials Research*, Vol. 86A, Issue 1, pp. 61-75, 2008.

- [66] H.-I Chang and Y. Wang (2011), "Cell Responses to Surface and Architecture of Tissue Engineering Scaffolds," *Regenerative Medicine and Tissue Engineering - Cells and Biomaterials*, D. Eberli (Ed.), ISBN: 978-953-307-663-8, pp. 569-589.
- [67] J. S. Park, et. al., "A multimodality CMOS sensor array for cell-based assay and drug screening," *IEEE ISSCC*, Feb. 2015, pp. 208-209.
- [68] Y. Temiz, S. Kilchenmann, Y. Leblebici and C. Guiducci, "3D integration technology for lab-on-a-chip applications," in *Electronics Letters*, vol. 47, no. 26, pp. S22-S24, December 22 2011.
- [69] Mackavicius EL, Fee MS. Building a state space for song learning. *Current Opinion in Neurobiology*, vol. 49, pp. 59-68 , April 2018.
- [70] Srivastava KH, Elemans CPH, Sober SJ. Multifunctional and context-dependent control of vocal acoustics by individual muscles. *J Neurosci*, vol. 35, iss. 42, pp. 14183-14194, October 2015.
- [71] Tang C, Chehayeb D, Srivastava K, Nemenman I, Sober SJ. Millisecond-scale motor encoding in a cortical vocal area. *PLoS Biology*, vol. 12, iss. 12, December 2014.
- [72] Guitchounts G, Markowitz JE, Liberti WA, Gardner TJ. A carbon-fiber electrode array for long-term neural recording. *J Neural Eng*, Vol. 10, iss. 4, 046016, July 2017.
- [73] Lin L, Osan R, Shoham S, Jin W, Zuo W, Tsien JZ. Identification of network-level coding units for real-time representation of episodic experiences in the hippocampus. *PNAS*, vol. 102, iss. 17, pp. 6125-6130, April 2005.
- [74] Churchland MM, et al. Neural population dynamics during reaching. *Nature*, vol. 487, iss. 7405, pp. 51-56, July 2012.
- [75] Nemenman I, Shafee F, Bialek W. "Entropy and inference, revisited," in *Adv Neural Inf Proc Syst*, vol 14, TG Dietterich, S Becker and Z Ghahramani, Eds. Cambridge, MA: MIT Press, 2002.
- [76] Kraskov A, Stogbauer H, Grassberger P. Estimating mutual information. *Phys Rev E Stat Nonlin Soft Matter Phys*, vol. 69, iss. 6, pt. 2, 066138, June 2004.
- [77] Nemenman I, Lewen GD, Bialek W, de Ruyter van Steveninck RR. Neural coding of natural stimuli: Information a sub-millisecond resolution. *PLoS Comp Bio*, vol. 4, iss. 3, e1000025, March 2008.
- [78] Sober SJ, Wohlgenuth MJ, Brainard MS. Central contributions to acoustic variation in birdsong. *J Neurosci*, vol. 28, iss. 41, pp. 10370-10379, October 2008.
- [79] Heitler WJ. DataView: A tutorial tool for data analysis. Template-based spike sorting and frequency analysis. *J Undergrad Neurosci Educ*, vol. 6, iss. 1, pp. A1-A7, October 2007.
- [80] Siegelbaum SA, Hudspeth AJ. Principles of neural science, vol. 4. ER Kandel, JH Schwartz and TM Jessell, Eds. New York: McGraw-Hill, 2000, pp. 768-789.
- [81] Lau, J.H., "Evolution, challenge, and outlook of TSV, 3D IC integration and 3d silicon integration," in *Advanced Packaging Materials (APM)*, 2011 International Symposium on , vol., no., pp.462-488, 25-28 Oct. 2011

- [82] Mourier, T. et al, "3D Integration challenges today from technological toolbox to industrial prototypes," in Interconnect Technology Conference (IITC), 2013 IEEE International , vol., no., pp.1-3, 13-15 June 2013
- [83] Ko, C.T. et al, "Wafer-level 3D integration with Cu TSV and micro-bump/adhesive hybrid bonding technologies," in 3D Systems Integration Conference (3DIC), 2011 IEEE International , vol., no., pp.1-4, Jan. 31 2012-Feb. 2 2012
- [84] H. S. Yang, C. Zhang and M. S. Bakir, "Self-Aligned Silicon Interposer Tiles and Silicon Bridges Using Positive Self-Alignment Structures and Rematable Mechanically Flexible Interconnects," in IEEE Transactions on Components, Packaging and Manufacturing Technology, vol. 4, no. 11, pp. 1760-1768, Nov. 2014.
- [85] Chaoqi Zhang et al, "Highly Elastic Gold Passivated Mechanically Flexible Interconnects," in Components, Packaging and Manufacturing Technology, IEEE Transactions on , vol.3, no.10, pp.1632-1639, Oct. 2013
- [86] E. Slavcheva et al, "Electrodeposition and properties of NiW films for MEMS application," *Electrochim. Acta*, vol. 50, no. 28, pp. 5573–5580, Sep. 2005.
- [87] Unchwaniwala, K.B. et al, "Electrical analysis of IC packaging with emphasis on different ball grid array packages," in Electronic Components and Technology Conference, 2001. Proceedings., 51st , vol., no., pp.1496-1501, 2001.
- [88] Xu, Z. and J. Lu, "Through-silicon-via fabrication technologies, passives extraction, and electrical modeling for 3-D integration/packaging," *IEEE Transactions on Semiconductor Manufacturing*, Vol. 26, No. 1, 23–34, 2013.
- [89] Rodionov, V.N. & Goncharov, A.I. *Combust Explos Shock Waves* (1995) 31: 313.
- [90] Hoyeol Cho et al, "Power comparison between high-speed electrical and optical interconnects for inter-chip communication," *Interconnect Technology Conference, 2004. Proceedings of the IEEE 2004 International , vol., no., pp.116,118, 7-9 June 2004.*
- [91] A. J. Zilkie et al, "Power-efficient III-V/silicon external cavity DBR lasers," *Opt. Express* 20(21), 23456–23462 (2012).
- [92] H. Wu; M. Khmour; P. Apsangi; H. Yu, "High Frequency Magnetic Thin Film Inductor Integrated on Flexible Organic Substrates," in *IEEE Transactions on Magnetics* , 2017.
- [93] T. Akagi, S. Abe, M. Hatanaka and S. Matsumoto, "An isolated DC-DC converter using air-core inductor for power supply on chip applications," 2015 IEEE International Telecommunications Energy Conference (INTELEC), Osaka, 2015, pp. 1-6.
- [94] N. Wang, T. O'Donnell, S. Roy, P. McCloskey, and C. O'Mathuna, "Micro-inductors integrated on silicon for power supply on chip," *J. Magn. Mater.*, vol. 316, no. 2, pp. e233–e237, Sep. 2007.
- [95] E.-C. Park, J.-B. Yoon, S. Hong, and E. Yoon, "A 2.6 GHz low phasenoise VCO monolithically integrated with high Q MEMS inductors," in *Proc. IEEE 28th Eur. Solid-State Circuits Conf. (ESSCIRC)*, Sep. 2002, pp. 147–150.

- [96] C. Zhang, L. Guo, L. F. Wang, J. Q. Huang and Q. A. Huang, "A passive wireless integrated humidity sensor based on dual-layer spiral inductors," IEEE SENSORS 2014 Proceedings, Valencia, 2014, pp. 657-660.
- [97] J. N. Burghartz and B. Rejaei, "On the design of RF spiral inductors on silicon," in IEEE Transactions on Electron Devices, vol. 50, no. 3, pp. 718-729, March 2003.
- [98] S Uchiyama et al 2013 J. Micromech. Microeng. 23 114009
- [99] T.C. Lee, Y-S Chang, C-M Hsu, S-C Hsieh, P-N Lee, Y-C Hsieh, L-C Wang and L.Zhang, "Glass based 3D-IPD integrated RF ASIC in WLCSP," 2017 IEEE 67th Electronic Components and Technology Conference (ECTC), Orlando, FL, 2017
- [100] Chaoqi Zhang et al 2017 J. Micromech. Microeng. 27 025014
- [101] X. Zhang, P. K. Jo, M. Zia, G. S. May and M. S. Bakir, "Heterogeneous Interconnect Stitching Technology With Compressible MicroInterconnects for Dense Multi-Die Integration," in IEEE Electron Device Letters, vol. 38, no. 2, pp. 255-257, Feb. 2017.
- [102] X. Zhang, "3D and 2.5D heterogeneous integration platforms with interconnect stitching and microfluidic cooling" Internet: <https://smartech.gatech.edu/handle/1853/58647>, 2017[October 11, 2018].
- [103] R. Mahajan, R. Sankman, N. Patel, D.-W. Kim, K. Aygun, Z. Qian, Y. Mekonnen, I. Salama, S. Sharan, D. Iyengar, and D. Mallik, "Embedded multi-die interconnect bridge (EMIB)—A high density, high bandwidth packaging interconnect," in Proc. IEEE Electron. Compon. Technol. Conf. (ECTC), Jun. 2016, pp. 557–565, doi: 10.1109/ECTC.2016.201.
- [104] D. M. Pozar, Microwave Engineering, 3rd ed. New York: Wiley, 2005.
- [105] O. F. Hikmat and M. S. Mohamed Ali, "RF MEMS Inductors and Their Applications—A Review," in Journal of Microelectromechanical Systems, vol. 26, no. 1, pp. 17-44, Feb. 2017.
- [106] X. Yu, M. Kim, F. Herrault, C. H. Ji, J. Kim and M. G. Allen, "Silicon-embedded 3D toroidal air-core inductor with through-wafer interconnect for on-chip integration," 2012 IEEE 25th International Conference on Micro Electro Mechanical Systems (MEMS), Paris, 2012, pp. 325-328.
- [107] V. Badilita et al., "On-chip three dimensional microcoils for MRI at the microscale," Lab Chip, vol. 10, no. 11, pp. 1387–1390, 2010.
- [108] L. Gu and X. Li, "High-Q Solenoid Inductors With a CMOS-Compatible Concave-Suspending MEMS Process," in Journal of Microelectromechanical Systems, vol. 16, no. 5, pp. 1162-1172, Oct. 2007.
- [109] C. Yang, S. Y. Wu, C. Glick, Y. S. Choi, W. Hsu and L. Lin, "3D printed RF passive components by liquid metal filling," 2015 28th IEEE International Conference on Micro Electro Mechanical Systems (MEMS), Estoril, 2015, pp. 261-264.
- [110] Roylance, Mechanical Properties of Materials, 2008.

- [111] H. Wang, "Magnetic sensors for diagnostic medicine: CMOS-based magnetic particle detectors for medical diagnosis applications," *IEEE Microwave Magazine*, vol. 14, no. 5, pp. 110-130, Jul/Aug 2013.
- [112] F. Heer, et al., "CMOS electro-chemical DNA-detection array with on-chip ADC," in *IEEE ISSCC Dig. Tech. Papers*, Feb. 2008, pp. 168–169, 604.
- [113] B. Jang, P. Cao, A. Chevalier, A. Ellington, A. Hassibi, "A CMOS fluorescence-based biosensor microarray," in *IEEE ISSCC Dig. Tech. Papers*, Feb. 2009, pp. 436–437, 437a.
- [114] D. Hall, et al., "A 256 channel magnetoresistive biosensor microarray for quantitative proteomics," in *IEEE VLSI Circuits (VLSIC)*, 15–17 June 2011, pp. 174–175.
- [115] S. Gambini, et al., "A CMOS 10kpixel baseline-free magnetic bead detector with column-parallel readout for miniaturized immunoassays," in *IEEE ISSCC Dig. Tech. Papers*, Feb. 2012, pp. 126–128.
- [116] H. Wang, A. Mohdavi, D. Tirrell, and A. Hajimiri, "A magnetic cell based sensor," *Lab Chip*, Vol. 12, Issue 21, pp. 4465–4471, 2012.
- [117] H. Wang, S. Kosai, C. Sideris, and A. Hajimiri, "An ultrasensitive CMOS magnetic biosensor array with correlated double counting noise suppression," *IEEE MTT-S Int. Microwave Symp. (IMS)*, pp.616-619, May 2010.
- [118] B. Eversmann, et al., "A 128×128 CMOS biosensor array for extracellular recording of neural activity," *IEEE JSSC*, vol. 38, no. 12, Dec. 2003.
- [119] M. K. Bhuyan, J. I. Rodriguez-Devora, K. Fraser, and T.-L. Tseng, "Silicon substrate as a novel cell culture device for myoblast cells," *Journal of Biomedical Science* 2014, 21:47.
- [120] N. J. Hallab, K. J. Bundy, K. O'Connor, R. L. Moses, and J. J. Jacobs, "Evaluation of metallic and polymeric biomaterial surface energy and surface roughness characteristics for directed cell adhesion," *Tissue Engineering*, Feb. 2001, Vol. 7, No. 1, pp.55-71.
- [121] T.-W. Chung, D.-L. Liu, S.-Y. Wang, S.-S. Wang, "Enhancement of the growth of human endothelial cells by surface roughness at nanometer scale," *Biomaterials* 24 (2003) 4655–4661.
- [122] R. A. Gittens, et. al., "The effects of combined micron-/submicron-scale surface roughness and nanoscale features on cell proliferation and differentiation," *Biomaterials* 32 (2011) 3395-3403.
- [123] I. Keen, et. al., "Surface roughness and topography of Poly(3-hydroxybutyrate-co-3-hydroxyvalerate) influences osteoblast cell growth," *Journal of Biomaterials Science, Polymer Edition* 18(9), pp. 1101-1123. 2007.
- [124] M. Jäger, et. al., "Osteoblast differentiation onto different biomaterials with an endoprosthetic surface topography in vitro," *Journal of Biomedical Materials Research*, Vol. 86A, Issue 1, pp. 61-75, 2008.

- [125] H.-I Chang and Y. Wang (2011), “Cell Responses to Surface and Architecture of Tissue Engineering Scaffolds,” *Regenerative Medicine and Tissue Engineering - Cells and Biomaterials*, D. Eberli (Ed.), ISBN: 978-953-307-663-8, pp. 569-589.
- [126] J. S. Park, et. al., “A multimodality CMOS sensor array for cell-based assay and drug screening,” *IEEE ISSCC*, Feb. 2015, pp. 208-209.
- [127] H. S. Yang, C. Zhang, and M. S. Bakir, “Self-Aligned Silicon Interposer Tiles And Silicon Bridges Using Positive Self-Alignment Structures and Rematable Mechanically Flexible Interconnects,” *IEEE TCPMT*, vol. 4, no.11, pp. 1760-1768, Nov. 2014.
- [128] Guitchounts G, Markowitz JE, Liberti WA, Gardner TJ. A carbon-fiber electrode array for long-term neural recording. *J Neural Eng*, Vol. 10, iss. 4, 046016, July 2017.
- [129] Lin L, Osan R, Shoham S, Jin W, Zuo W, Tsien JZ. Identification of network-level coding units for real-time representation of episodic experiences in the hippocampus. *PNAS*, vol. 102, iss. 17, pp. 6125-6130, April 2005.
- [130] Churchland MM, et al. Neural population dynamics during reaching. *Nature*, vol. 487, iss. 7405, pp. 51-56, July 2012.
- [131] Nemenman I, Shafee F, Bialek W. “Entropy and inference, revisited,” in *Adv Neural Inf Proc Syst*, vol 14, TG Dietterich, S Becker and Z Ghahramani, Eds. Cambridge, MA: MIT Press, 2002.
- [132] Kraskov A, Stogbauer H, Grassberger P. Estimating mutual information. *Phys Rev E Stat Nonlin Soft Matter Phys*, vol. 69, iss. 6, pt. 2, 066138, June 2004.
- [133] Nemenman I, Lewen GD, Bialek W, de Ruyter van Steveninck RR. Neural coding of natural stimuli: Information a sub-millisecond resolution. *PLoS Comp Bio*, vol. 4, iss. 3, e1000025, March 2008.
- [134] Sober SJ, Wohlgemuth MJ, Brainard MS. Central contributions to acoustic variation in birdsong. *J Neurosci*, vol. 28, iss. 41, pp. 10370-10379, October 2008.
- [135] Heitler WJ. DataView: A tutorial tool for data analysis. Template-based spike sorting and frequency analysis. *J Undergrad Neurosci Educ*, vol. 6, iss. 1, pp. A1-A7, October 2007.
- [136] Siegelbaum SA, Hudspeth AJ. Principles of neural science, vol. 4. ER Kandel, JH Schwartz and TM Jessell, Eds. New York: McGraw-Hill, 2000, pp. 768-789.
- [137] Kadir SN, Goodman DFM, Harris KD. High-dimensional cluster analysis with the masked EM algorithm. *Neural computation*, vol. 26, iss. 11, pp. 2379-2394, November 2014.
- [138] Rossant C, et al. Spike sorting for large, dense electrode arrays. *Nat Neurosci*, vol. 19, iss. 4, pp. 634-641, March 2016.
- [139] Byun D, Cho SJ, Lee BH, Min J, Lee JH, K S. Recording nerve signals in canine sciatic nerves with a flexible penetrating microelectrode array. *J Neural Engineering*, vol. 14, iss. 4, 046023, June 2017.

- [140] Lee WR, Im C, Koh CS, Kim JM, Sjhin HC, Seo JM. A convex-shaped, PDMS-parylene hybrid multichannel ECoG-electrode array. Engineering in Medicine and Biology Society (EMBC), 2017 39th Annual International Conference of the IEEE, IEEE, pp. 1093-1096, July 2017.
- [141] Wang J, et al. "Decoding peripheral nerve sensory information with a spiked flexible neural interface," in Micro Electro Mechanical Systems (MEMS), 2018 IEEE, IEEE, pp. 182-185, January 2018.
- [142] Guo, Liang, and Stephen P. DeWeerth. "An Effective Lift-Off Method for Patterning High-Density Gold Interconnects on an Elastomeric Substrate." *Small* (Weinheim an Der Bergstrasse, Germany) 6.24 (2010): 2847–2852. PMC.
- [143] Lee, M.-T., Lee, D., Sherry, A., Grigoropoulos, C.P., "Rapid selective metal patterning on polydimethylsiloxane (PDMS) fabricated by capillarity-assisted laser direct write.", *J. Micromech. Microeng.* 2011, 21, 095018.
- [144] L. Li et al, "Nanofabrication on unconventional substrates using transferred hard masks", *Scientific Reports* volume 5, Article number: 7802 (2015)
- [145] S. Metz, F. Oppliger, R. Holzer, B. Buisson, D. Bertrand and P. Renaud, "Fabrication and test of implantable thin-film electrodes for stimulation and recording of biological signals," 1st Annual International IEEE-EMBS Special Topic Conference on Microtechnologies in Medicine and Biology. Proceedings (Cat. No.00EX451), Lyon, 2000, pp. 619-623.
- [146] Mimoun, B., Pham, H.T., Henneken, V., Dekker, R., "Residue-free plasma etching of polyimide coatings for small pitch vias with improved step coverage.", *J. Vac. Sci. Technol. B Nanotechnol. Microelectron. Mater. Process. Meas. Phenom.* 2013, 31, 021201
- [147] W. Chen, R. H. W. Lam and J. Fu, "Photolithographic surface micromachining of polydimethylsiloxane (PDMS).", *Lab Chip*, 2011, 12, 391–395.
- [148] Lin K, Wang X, Zhang X, Wang B, Huang J, Huang F. An FPC based flexible dry electrode with stacked double-micro-domes array for wearable biopotential recording system. *Microsystem Technologies*, vol. 23, iss. 5, pp.1443-1451, May 2017.
- [149] Guvanasen GS, et al. A stretchable microneedle electrode array for stimulating and measuring intramuscular electromyographic activity. *Neural Systems and Rehabilitation Engineering, Transactions on, IEEE*, no. 9, pp. 1440-1452, September 2017.
- [150] Kim JM, Im C, Lee WR. Plateau-shaped flexible polymer microelectrode array for neural recording. *Polymers*, vol. 9, iss. 12, p. 690, December 2017.
- [151] Metallo C, White RD, Trimmer BA. Flexible parylene-based microelectrode arrays for high resolution EMG recordings in freely moving small animals. *J Neurosci Methods*, vol. 195, iss. 2, pp. 176-184, February 2011.
- [152] M. S. Nandra, I. A. Lavrov, V. R. Edgerton and Y. Tai, "A parylene-based microelectrode array implant for spinal cord stimulation in rats," 2011 IEEE 24th

International Conference on Micro Electro Mechanical Systems, Cancun, 2011, pp. 1007-1010.

- [153] L. Chou, S. Tsai, W. Chang, J. Chiou and T. Chiu, "A parylene-C based 16 channels flexible bio-electrode for ECoG recording," SENSORS, 2014 IEEE, Valencia, 2014, pp. 877-880.
- [154] S. Stokov, A. Schander, H. Stemmann, T. TeBmann, W. Lang and A. Kreiter, "A flexible multichannel ECoG array with PEDOT-coated electrodes for minimally invasive recording and stimulation," 2017 IEEE SENSORS, Glasgow, 2017, pp. 1-3.
- [155] C. Zhang, H. S. Yang, and M. S. Bakir, "A double-lithography and double-reflow process and application to multi-pitch multi-height mechanical flexible interconnects," J. Micromech. Microeng., vol. 27, no. 2, p. 025014, 2017.